# CHARACTERIZATION AND MODELING OF A MEMS MICROMIRROR ARRAY

# CHARACTERIZATION AND MODELING OF A MEMS MICROMIRROR ARRAY FOR USE IN AN ADAPTIVE OPTICS SYSTEM

by

ROBERT A. LOCKHART

B.Sc.(Queen's) 2003

A Thesis
Submitted to the School of Graduate Studies
in Partial Fulfilment of the Requirements
for the Degree
Master of Applied Science

McMaster University
©Copyright by Robert A. Lockhart, 2006.

MASTER OF APPLIED SCIENCE (2006)
(Engineering Physics)

McMaster University
Hamilton, Ontario

TITLE: Characterization and modeling of a MEMS Micromirror Array For Use in an Adaptive Optics System

AUTHOR: Robert A. Lockhart

SUPERVISOR: Dr. R. N. Kleiman

NUMBER OF PAGES: x, 124

# Abstract

In recent years, deformable micromirror arrays have become the focus of several attempts to create cost efficient adaptive optics systems for vision science. Conversely, the Digital Micromirror Device$^{\text{TM}}$ (DMD$^{\text{TM}}$) has been overlooked by several applications, including adaptive optics, due to its inherent bistability. As a means of addressing this limitation, this thesis suggests multiple methods to demonstrate the feasibility of analog operation of the DMD$^{\text{TM}}$. The first step in this process involves the characterization of the DMD$^{\text{TM}}$ by means of an automated, optical measurement system. This system was developed to actively monitor the angular deflection of individual micromirrors in the MEMS array. Two key mechanical properties of the microstructure - the natural frequency and the quality factor - are determined through analysis of the micromirrors' recorded dynamic behaviour. Further, through automation of the characterization setup, an investigation of device uniformity is presented exposing a clear trend in the measured micromirror properties over 160 tested mirrors in the DMD$^{\text{TM}}$ array. This linear trend is attributed to the variation in thickness of the torsional hinges as a result of the sputtering deposition process. Using the DMD$^{\text{TM}}$ characteristics discovered through experimentation, a computationally inexpensive, one-dimensional model based on the fourth order Runge-Kutta numerical method is constructed to simulate the response of the DMD$^{\text{TM}}$ micromirrors to user defined input voltage waveforms. Simulations are initially used to exhibit the validity of the model for existing DMD$^{\text{TM}}$ voltage patterns through a comparison with measured micromirror responses, and subsequently used to demonstrate two proposed methods of analog operation. The first method creates a limited form of analog control by varying the amplitude of 16 analog bias voltage lines, whereas the second method provides complete analog operation of the DMD$^{\text{TM}}$ using high frequency pulse width modulation of the underlying address circuitry.

# Acknowledgements

There are several people who have been influential throughout my work on this project. I would like to thank, first and foremost, Dr. Rafael Kleiman, my supervisor, who has not only provided the resources to make this research possible but has also provided helpful guidance and insightful ideas to further this work. I am very appreciative of my group of Dr. Oleksa Hulko, Édgar Huante Cerón, Paul Dreidger, as well as Jorge Fonseca Campos who gratefully offered their thoughts and feedback on many of the barriers which arose throughout this research. Thank you to my committee members, Dr. John Preston and Dr. Steve Hranilovic, for agreeing to be a part of this project. My thanks also goes to Julia D'Aloisio who edited several initial drafts of this thesis and to my family for their constant support.

# Contents


**List of Figures** vii

**List of Tables** x

**1 Introduction** 1
- 1.1 MEMS . . . 1
  - 1.1.1 Micromirror Arrays . . . 2
  - 1.1.2 The Digital Micromirror Device (DMD$^{TM}$) . . . 7
- 1.2 Adaptive Optics . . . 16
  - 1.2.1 Vision Science . . . 18
- 1.3 Problem Statement . . . 21
- 1.4 Outline . . . 21

**2 Electrostatic Actuation** 23
- 2.1 Parallel Plate Capacitor . . . 23
- 2.2 Mechanical Actuation . . . 25
- 2.3 Steady-State Solutions and the Pull-in Instability . . . 27
- 2.4 Digital Operation . . . 30
- 2.5 Free Oscillations . . . 33

**3 Optical Setup** 36
- 3.1 Design . . . 37
  - 3.1.1 Beam Propagation . . . 37
  - 3.1.2 Collection Lenses . . . 44
  - 3.1.3 Position Sensitive Detector . . . 48
  - 3.1.4 Motion Controllers . . . 52
  - 3.1.5 Spatial Modeling . . . 52
  - 3.1.6 DMD Discovery$^{TM}$ 1100 . . . 52
- 3.2 Alignment . . . 53
- 3.3 Calibration . . . 54

**4 Experimental Results** **58**
4.1 Automated Experimental Design . . . . . 59
4.1.1 Alignment Procedure . . . . . 60
4.2 Results . . . . . 61
4.2.1 Natural Frequency and Quality Factor . . . . . 63
4.2.2 Switching Time . . . . . 70
4.2.3 Deflection Angles . . . . . 72

**5 Simulation** **74**
5.1 Modeling Equation . . . . . 74
5.1.1 Electrostatic Torque . . . . . 75
5.1.2 Moment of Inertia . . . . . 79
5.1.3 Mechanical Torque . . . . . 80
5.1.4 Damping . . . . . 81
5.1.5 DMD™ Dimensions . . . . . 82
5.2 DMD™ Model . . . . . 83
5.2.1 PSD Transfer Function . . . . . 84
5.2.2 Results . . . . . 85
5.3 Analog Operation . . . . . 89
5.3.1 Bias Control . . . . . 90
5.3.2 Address Voltages . . . . . 90
5.3.3 Angle Stabilization . . . . . 94
5.3.4 Pull-In . . . . . 95

**6 Conclusions and Future Work** **97**
6.1 Limitations . . . . . 98
6.2 Future work . . . . . 99

**A Beam Trajectory** **100**

**B Runge-Kutta Numerical Method** **103**

**C Moment of Inertia** **106**

**D DMD Micromirror Modeling: MATLAB Simulation Code** **110**

**Bibliography** **119**

# List of Figures


1.1 Degrees of freedom of a micromirror: tip, tilt and piston. . . . . . . . 3
1.2 Comparison of a piston micromirror: model and SEM . . . . . . . . . 4
1.3 Flexure vs. torsional micromirror design . . . . . . . . . . . . . . . . 5
1.4 Schematic of 2DOF micromirror with gimbal frame . . . . . . . . . . 6
1.5 SEM micrograph of fabricated 3DOF micromirror using electrostatic comb drives. . . . . . . . . . . . . . . . . . . . . . . . . . . . . . 6
1.6 DMD™ projection schematic . . . . . . . . . . . . . . . . . . . . . . 9
1.7 Exploded view of the DMD™ micromirror layers. . . . . . . . . . . . 10
1.8 Visible structure of early generation DMD design: hinges, supports, etc. 11
1.9 Reliability development and lifetime improvement of DMD™. . . . . 13
1.10 SEM image of spring landing tip. . . . . . . . . . . . . . . . . . . . . 15
1.11 Fundamental principle of adaptive optics. . . . . . . . . . . . . . . . . 17
1.12 Example of phase conjugation. . . . . . . . . . . . . . . . . . . . . . 18
1.13 Point spread function of human eye . . . . . . . . . . . . . . . . . . 18

2.1 Schematic of the parallel plate capacitor model. . . . . . . . . . . . . 26
2.2 Comparison of mechanical and electrostatic torque. . . . . . . . . . . 29
2.3 Snap down and hysteresis phenomena of electrostatic actuators. . . . 29
2.4 Comparison of parallel and torsional plate models. . . . . . . . . . . . 31
2.5 Schematic of the 'crossover' transition. . . . . . . . . . . . . . . . . . 32
2.6 Simulated 'crossover' and 'stay' trajectories. . . . . . . . . . . . . . . 33

3.1 Schematic of the optical setup. . . . . . . . . . . . . . . . . . . . . . . 38
3.2 Schematic of the setup used in a knife edge test. . . . . . . . . . . . . 41
3.3 Plot of the data collected representing the integral of a Gaussian function. 42
3.4 Beam width measurements. . . . . . . . . . . . . . . . . . . . . . . . 43
3.5 Schematic representing the increase in optical angle as a result of reflection. . . . . . . . . . . . . . . . . . . . . . . . . . . . . . . . . 44
3.6 Two lenses acting as an optical relay. . . . . . . . . . . . . . . . . . . 45
3.7 Spherical aberration. . . . . . . . . . . . . . . . . . . . . . . . . . . . 45
3.8 OLSO ray tracing diagram of a poor lens. . . . . . . . . . . . . . . . 46

3.9 OLSO ray tracing diagram of an aspheric lens. . . . . . . . . . . . . . 47
3.10 Functional diagram of a position sensitive detector. . . . . . . . . . . 47
3.11 Intensity dependency of the PSD. . . . . . . . . . . . . . . . . . . . . . 49
3.12 Measured linearity of the PSD. . . . . . . . . . . . . . . . . . . . . . . 50
3.13 PSD transfer function. . . . . . . . . . . . . . . . . . . . . . . . . . . 51
3.14 AutoCAD model of optical setup . . . . . . . . . . . . . . . . . . . . . 53
3.15 Angular calibration setup. . . . . . . . . . . . . . . . . . . . . . . . . 55
3.16 Calibration curves of the optical setup. . . . . . . . . . . . . . . . . . 57

4.1 Automated test path of the DMD™. . . . . . . . . . . . . . . . . . . . 60
4.2 Astigmatism of propagating beam . . . . . . . . . . . . . . . . . . . . 62
4.3 Experimentally recorded a)'float' trajectory and b)'stay' and 'crossover' trajectories. . . . . . . . . . . . . . . . . . . . . . . . . . . . . . . . 64
4.4 Measured 'float' transition along with the respective fit. . . . . . . . . 65
4.5 Device uniformity of $\omega_0$ and $Q$ . . . . . . . . . . . . . . . . . . . . . . 68
4.6 Planar fit produced of the natural frequency data. . . . . . . . . . . . 69
4.7 Distributions of measured $\omega_0$ and $Q$ values . . . . . . . . . . . . . . . 71

5.1 Schematic of a torsional actuator. . . . . . . . . . . . . . . . . . . . . 76
5.2 Counter electrostatic fields in the DMD™ design. . . . . . . . . . . . . 78
5.3 Components of the DMD™ micromirror. . . . . . . . . . . . . . . . . . 79
5.4 Simulations of electrostatic torque acting on a DMD™ micromirror. . 84
5.5 Fourier transform of the 'crossover' trajectory . . . . . . . . . . . . . 85
5.6 Comparison of simulated trajectories with experimental data. . . . . 86
5.7 Simulated 'crossover' transition using two stage model. . . . . . . . . 88
5.8 Simulation of analog operation by varying the amplitude of the bias voltage. . . . . . . . . . . . . . . . . . . . . . . . . . . . . . . . . . . . 91
5.9 Square wave voltage. . . . . . . . . . . . . . . . . . . . . . . . . . . . . 91
5.10 Schematic representing the voltages on the address electrodes equated to torques on the micromirror . . . . . . . . . . . . . . . . . . . . . . 92
5.11 Simulation of analog operation based on the modulation of the address states. . . . . . . . . . . . . . . . . . . . . . . . . . . . . . . . . . . . 93
5.12 Theoretical frequency response of the DMD™ micromirror. . . . . . 94
5.13 Stabilization of the angular deflection as a function of the input voltage frequency. . . . . . . . . . . . . . . . . . . . . . . . . . . . . . . . . . 95

A.1 Schematic of a non-normal incident beam reflecting of a rotating plane before striking the detection plane. . . . . . . . . . . . . . . . . . . . 101
A.2 Arc trajectory of a beam reflecting off of a rotational mirror at non-normal incidence . . . . . . . . . . . . . . . . . . . . . . . . . . . . . . 102

C.1 Dimensions of mirror plate showing axis and rotation. . . . . . . . . . 107
C.2 Dimensions of support post showing axis and rotation. . . . . . . . . 107

C.3 Dimensions of yoke showing axis and rotation. . . . . . . . . . . . . . 108
C.4 Dimensions of torsional hinge showing axis and rotation. . . . . . . . 109

# List of Tables

1.1 Comparison of the deformable mirrors used for aberration correction. 20

4.1 Mean values for $f_0$ and $Q$ for 160 tested mirrors. . . . . . . . . . . . . 66
4.2 Mean optical switching times of 160 tested mirrors. . . . . . . . . . . 72
4.3 Mean resting angles of 160 mirrors in various transitional states. . . . 73

5.1 DMD$^{TM}$ micromirror dimensions. . . . . . . . . . . . . . . . . . . . . . 83
5.2 Comparison of $I$,$K_\theta$,$K_b$, and $\eta$: model vs. geometrical. . . . . . . . . 89

# Chapter 1

# Introduction

## 1.1 MEMS

Over the last twenty years, researchers have developed novel fabrication techniques used to create MicroElectroMechanical Systems (MEMS, micro sized, integrated, mechanically compliant sensors and actuators) to provide solutions not only for new applications but also products where macro sized solutions were already in place. Due to extensive advances in microfabrication, MEMS devices boast similar mechanical abilities to that of their older, macro counterparts; however, it is not simply enough to build smaller devices with similar capabilities. There has to be an obvious incentive to induce change. Fortunately, it is also the case that many MEMS devices also offer increased speed and sensitivity, reduced weight, require less power consumption, and most importantly - lower costs. Inertial, pressure, and chemical sensors, RF and optical switching, biomedical devices and optical projection are just a few examples where MEMS devices are beginning to replace older technologies.

A major reason for the early success of MEMS stems from the fact that these miniature mechanical systems use much of the same fabrication technology as the integrated circuit (IC) industry. This permits a straightforward incorporation between the mechanical devices and the electronic circuitry which drives them. In turn, this allows for skillful integration into new and existing systems along with a reduced fabrication cost and a greater reliability.

Two of the more successful, commercially available MEMS devices include the inertial sensor developed by Analog Devices to trigger the airbag release in an automotive collision and Texas Instrument's Digital Micromirror Device (DMD$^{TM}$) which can now be found in digital projectors for both high definition cinema as well as light weight home and business projection applications.

### 1.1.1 Micromirror Arrays

Optical MEMS, a subset typically referred to as MOEMS, combine the micromechanical ability of MEMS with the properties of photonics to control the propagation of light. With the recent drive to create an optical bench on a single chip combined with the growing number of optical sensor applications there is certainly not an absence of MOEMS devices being developed. The extensive list currently includes micromirrors, microlenses, microshutters and choppers, modulators, switches, optically driven actuators and integrated optical sensors. Micromirrors play a critical role in MOEMS to modify optical path lengths and alter the direction of light signals. Stand alone micromirrors have been used in applications such as a microinterferometery or a single optical switch; however, it has become apparent that arrays of micromirrors are often more desirable for the majority of applications.

Several examples of micromirror arrays exist in the literature for a variety of purposes. Texas Instruments' projectors based on Digital Light Processing (DLP$^{TM}$) technology use rotational mirror arrays to steer light towards or away from the image plane providing a black and white pixelated image [1]. Optical interconnects utilize deflectable micromirror arrays to couple light in and out of optical fibers [2]. Fresnel lenses are created by modifying the surface profile of micromirror arrays to manipulate the diffractive effects and permit beam steering and focusing applications [3]. In each of these examples light is reflected by mechanically compliant controllable micromirror arrays, although, the design from one device to the next can be quite different.

There are three main classes of micromirrors based on their allowed motion and degrees of freedom. In the first, as demonstrated with the example of projection displays, the mirrors are able to rotate or 'tilt' about a single axis parallel to the plane

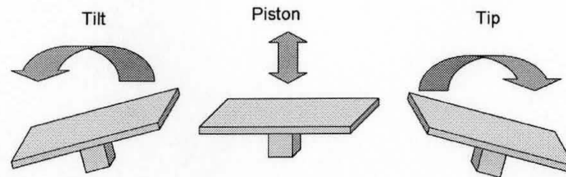


Figure 1.1: Degrees of freedom of a micromirror: tip, tilt and piston.

of the array. The second class adds a degree of freedom to the first allowing the mirror to rotate in two dimensions ('tip' and 'tilt') with both rotational axes lying parallel to the array. The third, and possibly the simplest class, provides transverse motion in the direction perpendicular to the mirror's surface. This 'up and down' motion is appropriately referred to as 'piston'. The three degrees of freedom are illustrated in figure 1.1. As a direct result of the complexity involved, all three degrees of freedom - tip, tilt and piston are rarely realized in a single device. However, in recent years it has been demonstrated [4].

Several groups have developed piston-only micromirrors making use of a wide range of actuation mechanisms common to MEMS devices. Electrostatic, piezoelectric, and thermal methods have all been realized. Although, due to the relative ease of fabrication, straight forward application of control, as well as the sharp response time of electrostatically actuated devices, most groups have moved towards this means of control. An electrostatic piston-only micromirror resembles a parallel plate capacitor in which the plates are held apart by springs allowing the upper plate to move freely in the vertical direction. A schematic of this is presented in figure 1.2(a) along side an SEM image of the physical mirror developed by Lee *et al.* [5]. The beams supporting the central mirror structure act as the springs in our simplified schematic and permit the height of the mirrors to be adjusted. Although the design in figure 1.2(b) quite closely resembles the simplified schematic, the parallel plate capacitor model is a very useful tool in developing simplified models of many MEMS designs based on electrostatic actuation methods. For this reason, further discussion of the parallel plate capacitor model follows in later chapters.

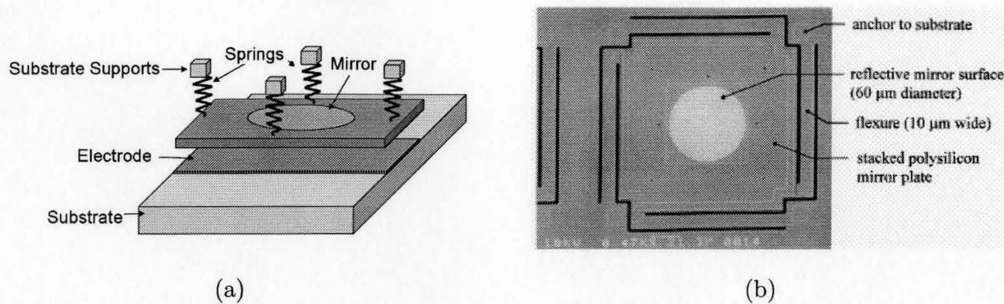


(a) (b)

Figure 1.2: Comparison of a) parallel plate capacitor mass on a spring model with b) an SEM image of a piston mirror developed by Lee *et al.* [5].

An early paper by Larry Hornbeck, the mastermind behind TI's DMD$^{\mathrm{TM}}$, presents several designs for single axis rotational micromirrors [6]. Two distinct groups stand out: torsional-beam mirrors and flexure-beam mirrors. In both designs, a relatively large, thick, reflective surface is freely suspended above an air gap by a thin beam (or beams) which attach the mirror to a rigid support. The difference between the two groups becomes apparent in the way each reacts to an outside force applied to the mirror. As the name suggests, the support hinge of the flexure-beam design bends along its length, similar to a cantilever, in order to provide the compliant motion of the mirror. This action is similar to that of the piston design presented earlier, with the only difference being the placement of the support. To enable rotation, the support posts are positioned asymmetrically which leaves one or more edges free to drop further than the others resulting in a titling motion. On the other hand, in a torsional-beam design the support hinge is twisted. Typically two support hinges, placed symmetrically around the mirror, isolate its motion to a single axis rotation about the hinges. In either case, the relatively thick mirror surface as compared to the thickness of the hinge results in only the hinge flexing while ideally keeping the mirror flat. Both techniques have been successfully demonstrated by several groups over the years [7, 8, 9]. A comparison of the two styles is shown in figure 1.3.

Dokmeci *et al.* have been able to elaborate on the torsional micromirror technique to produce a rotational mirror with two degrees of freedom [2]. Their design places

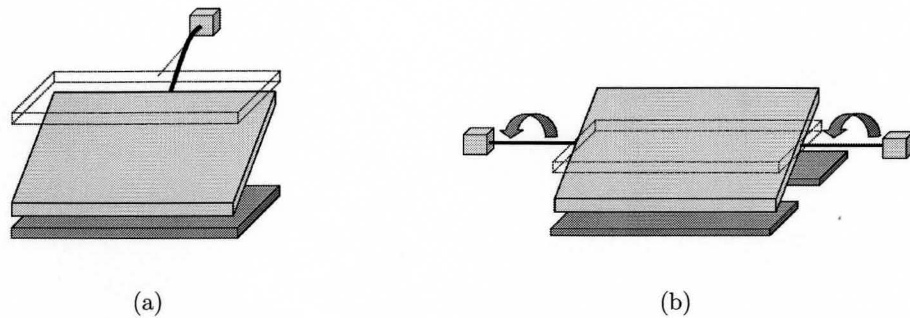


Figure 1.3: Schematics representing two types of rotating mirror designs a) a flexure micromirror b) a torsional micromirror.

an intermediate gimbal frame between the mirror plate and a rigid support. Both the mirror and the frame are free to rotate, albeit in separate directions, thus allowing a net rotation in two axes. A schematic of their design is shown in figure 1.4. With appropriately placed electrodes, the mirrors rotation can be controlled by means of electrostatic actuation. One electrostatic potential causes the mirror plate to rotate about the $x$-axis while another is used to rotate the frame about the $y$-axis. The net result is a mirror that is able to both 'tip' and 'tilt'. With the added freedom however, comes added complication. For example, this design was shown to experience crosstalk between the closely spaced electrodes. The interaction between the electrostatic fields means the actuation felt by either the mirror plate or the outer frame is not independent and will most likely require feedback control to accurately position the mirror.

Another design which in a way solves the problem of crosstalk between the electrodes was developed by Young. Instead of combining two torsional designs, Young combined the ideas of torsional mirrors with that of the flexure design [10]. By simply using two electrodes and positioning them in such a way that the cantilever type mirror described earlier can also rotate about its support hinge, a mirror with two degrees of rotational freedom was achieved. While, the problem of crosstalk is not completely removed, it is reduced because the same electrodes control both the rotational motion about the hinge as well as the deflection angle. The mirror's cantilever

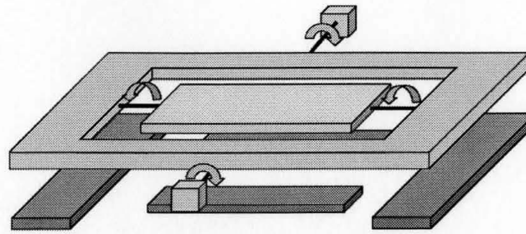

Figure 1.4: Schematic of 2DOF micromirror with gimbal frame.

deflection is adjusted by changing the bias on the electrodes simultaneously while the torsional deflection of the mirror is proportional to the variation between the two electrodes. For this reason, crosstalk only becomes an impeding issue when little or no cantilever deflection is desired.

Creating a mirror with three degrees of freedom adds complexity in both fabrication and device control; however, this increased versatility is often desired for many applications. Milanovic *et al.* have developed such a device at the Adriatic Research Institute [4]. Contrary to all other devices presented in this chapter, the

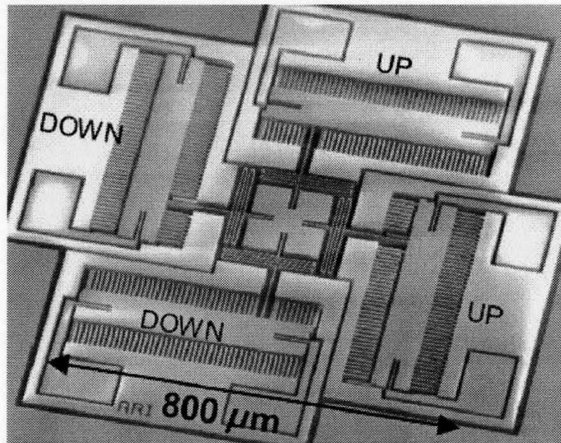


Figure 1.5: SEM micrograph of fabricated 3DOF micromirror using electrostatic comb drives [4].

three degree-of-freedom mirror is manipulated by a complex array of electrostatic comb drives. Although this approach eliminates the problem of cross talk experienced in previous devices, it comes at a price. In addition to the added complexity of fabrication, the comb drives occupy a rather large amount of space surrounding the mirror. The increased complexity of this device compared to previous examples is clearly visible in figure 1.5.

Beyond the degrees of freedom exhibited by an array of micromirrors, the optical efficiency (influenced by the optical fill factor and the reflectivity of the mirror itself) greatly affects the performance of the device. As previously mentioned, MEMS devices are benefiting from riding the coattails of the IC fabrication industry. As a result, the material of choice for most MEMS devices is the IC industry standard: polysilicon. As a means of achieving greater reflectivity, metal films, such as gold or aluminum, are occasionally sputtered onto the mirror surface. However, as in any multilayered material, inherent strains produced by intrinsic processing stresses and thermal expansion mismatches cause undesired curvature of the mirror surface [11].

A further problem which effects optical efficiency in MEMS arrays is the packing density of the elements or the optical fill factor. This is not as much a concern for optical interconnects as it is for perhaps projection and adaptive optics applications; although, having closely spaced optical switches may help to reduce spatial constraints and possibly reduce unnecessary weight. In projection and adaptive optics applications however, the consequences are much more severe. Space between the elements of the array allow light from the signal to be lost. For this reason, many of the devices that have been previously considered in this section are unacceptable for use in these applications. As demonstrated with the three degree-of-freedom mirror developed by Milanovic *et al.*, as well as the two degree-of-freedom array to some extent, there is typically a trade off experienced between mirror complexity and optical efficiency.

### 1.1.2 The Digital Micromirror Device (DMD™)

In 1987, a team of engineers at Texas Instruments (TI) led by Larry Hornbeck unveiled the first generation Digital Micromirror Device (DMD™) to compete with

existing Liquid Crystal Displays (LCD) and Cathode Ray Tubes (CRT) in the projection display market. By utilizing a MEMS array consisting of 528 × 1 micromirrors, Hornbeck *et al.* were able to create a truly digital, passive, reflective, spatial light modulator. Now, several years after its conception, the DMD™ is the critical component in TI's Digital Light Processing (DLP™) technology which is widely used for high definition digital cinema projectors as well as light weight home and business projectors and televisions.

The DMD™, currently in its fourth generation, boasts arrays consisting of between 500,000 and more than a millon micromirrors depending on the resolution of the device. The individual mirrors are square with sides of 12.68$\mu$m and spaced on a pitch of 13.68$\mu$m leaving a 1$\mu$m gap between adjacent mirrors. By making use of electrostatic actuation, each mirror in the array is individually addressable and able to rotate to positions of $\pm 12°$. During operation, white light is reflected off the surface of the DMD™ while each mirror in the array is set to either the 'ON' state or the 'OFF' state. When a mirror is positioned in the 'OFF' state, light reflecting off that mirror is directed towards an absorbing beam dump and effectively eliminated; however, when the mirror is in the 'ON' state, the reflected light will travel through a projection lens onto the image plane. As demonstrated in figure 1.6, this effectively creates a light and dark image in which each pixel is created by a single micromirror. To provide common resolutions various sized DMD™ arrays are available. For example, three common resolutions SVGA, XGA, and SXGA are produced with arrays consisting of 480,000 ($800 \times 600$), 786,000 ($1024 \times 768$), and 1.3 million ($1280 \times 1024$) micromirrors respectively.

### DMD™ Architecture

The DMD™ 'superstructure' is monolithically fabricated by depositing and patterning layers of aluminum and aluminum alloys on top of a single crystal silicon complementary metal-oxide-semiconductor (CMOS) memory circuit [13]. In keeping with a goal set in the early stages of the digital imaging project at TI, the DMD™ is fabricated in its entirety using standard semiconductor processes and equipment. As

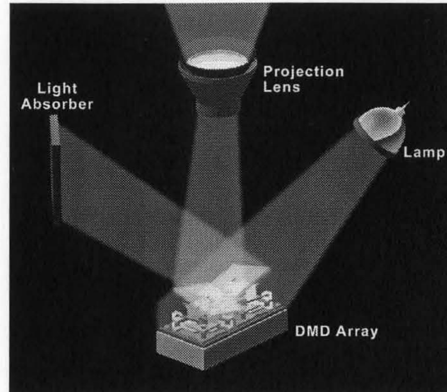


Figure 1.6: DMD$^{\text{TM}}$ projection schematic which defines a pixel as a single micromirror [12].

previously mentioned, this allows for a great reduction in fabrication cost as well as seamless integration between the mechanical layers of the DMD$^{\text{TM}}$ and the controlling circuitry which lies beneath.

An exploded view of a single mirror element in the DMD$^{\text{TM}}$ array is depicted in figure 1.7 [15]. The bottom layer containing the CMOS circuitry consists of a static random-access memory (SRAM) cell made up of a six-transistor circuit which is fabricated using a twin-well CMOS, 0.8$\mu$m, double-level metallization process [13]. This circuity provides addressability to each mirror in the array. The mechanical ability of the DMD$^{\text{TM}}$ is achieved through the freestanding yoke structure which is suspended above an air gap by two thin torsional hinges connected across two rigid support posts. The mirror itself is held on top of the yoke by another rigid support. A pair of address electrodes, connected through vias to complementary sides of the SRAM cell, are positioned under opposing corners of each mirror. A third voltage, the bias-reset voltage, is connected through the yoke and hinges to the mirror itself. The aluminum structure of the upper layers not only provides mechanical stability it also provides electrical conductivity between the layers. Depending on the state of the SRAM cell, the address electrodes will interchange between 0V and 5V. The greater electrostatic potential produced by a combination of the address and bias voltages

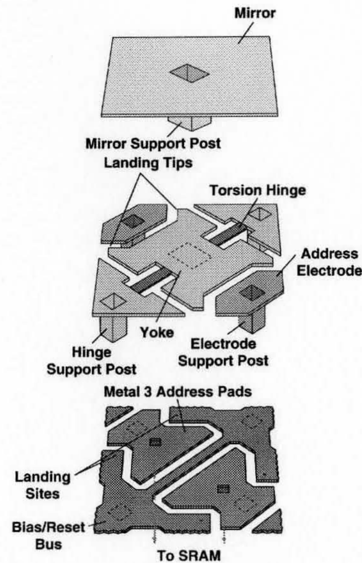


Figure 1.7: An exploded view of the layers which make up a single mirror in the DMD$^{TM}$ [14].

creates an attractive torque towards one of the electrodes causing the mirror and yoke structure to rotate. The torsional hinges oppose the motion; however, if the applied voltage is high enough, the potential will easily overcome the restoration force and the mirror will snap down. Mechanical stops are in place to ensure electrical isolation is always maintained. High voltages (26V) are intentionally used by the designers of the DMD$^{TM}$ in order to achieve bistability. This means each mirror in the DMD$^{TM}$ array can only physically exist in one of two states: 'ON' or 'OFF'. This effectively creates a digital optical switch.

A great deal of thought has been put into the design of the DMD$^{TM}$ to improve the optical performance of the device. Firstly, it is important to note that the aluminum structure not only provides stability and electrical connectivity, but it also provides a very reflective mirror surface for visible light. This eliminates the need for an additional reflective layer to be grown on top of the mirror surface which typically causes bending due to the thermal expansion mismatch of the materials. For this

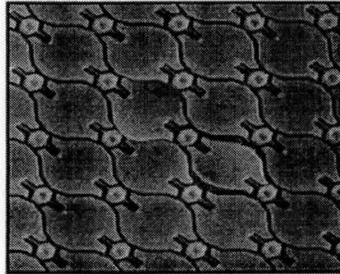

Figure 1.8: Visible structure of early generation DMD design: hinges, supports, etc. [16].

reason the mirror surface can be made ideally flat.

A second characteristic of the DMD$^{TM}$ which greatly improves the optical efficiency of the device is the design which places the mirror perched on top of the yoke support. Earlier DMD$^{TM}$ designs used closely packed 'football' shaped mirrors with visible hinges and mechanical supports (fig. 1.8). By supporting the mirror above the yoke structure, the only visible layer of the device from above is the mirror itself. This has been appropriately named the 'hidden hinge' design. Now with an optical fill factor of 85.2%, meaning 85.2% of the surface is made up of mirrors, less light is scattered and more light can be reflected in the intended direction. In terms of projection, this means greater brightness as well as higher contrast ratios.

### DMD$^{TM}$ Operation

Switching the mirror between the two stable positions is not quite as simple as altering the state of the SRAM cell beneath the mirror. The electrostatic potential that still exists between the closest address electrode and the mirror far exceeds the lowered potential required to allow the mechanical restoring force of the torsion spring to pull the mirror back to its equilibrium position. This process will be expanded upon in the following chapters. However, with this in mind, the research team at TI has invested a great deal of time in developing a perfectly timed reset voltage waveform which not only rotates the mirror from one position to the next - it does so in the quickest possible time. Van Kessel *et al.* have reported that the optical

switching time for a micromirror in the DMD™ array is $\sim 2\mu s$, although $\sim 16\mu s$ is required for the mirror to stabilize in its new position [15]. That is approximately 100,000 times faster than most LCD switching times.

Faster switching times are an obvious advantage for many applications; although, it was not initially understood why faster switching times are important for projection applications where the human visual system is certainly not able to operate at these frequencies. Upon examination it was noted that DLP™ takes advantage of the mirror's quick response to create greyscale images. With a technique referred to as binary Pulse Width Modulation (PWM), the micromirrors are turned 'ON' and 'OFF' for varying amounts of time relative to the shade of grey required. Due to the quickness of the mirror, the eye is unable to discern any flickering and instead integrates over time to produce a clear greyscale image. This is accomplished by passing a binary number to the DMD™ controller. For example, with a 4-bit word, each bit represents a specific amount of time based on the number of bits and the video frame rate being displayed. In this example, the shortest bit, or the least significant bit (LSB) represents 1/15 with the second, third and fourth bits representing 2/15, 4/15, 8/15 respectively. All together there are $2^4$ or 16 possible combinations which represents a greyscale with 16 equally spaced shades of grey. Currently, a single DMD™ is capable of 10-bit greyscale or 1024 shades of grey.

Colour projection is produced in one of two ways. In high quality cinema projection, typically three separate DMD™ arrays are used each reflecting a single colour: red, green, or blue. In home and business applications where cost is the primary concern, a colour wheel is used which splits incoming white light into equally timed portions of red, green and blue light.

### DMD™ Reliability

The digital imaging research group at TI has poured an enormous amount of effort into minimizing or eliminating the failure mechanisms of the DMD™. Since 1992, they have gradually increased its lifetime by making small yet crucial improvements to the fabrication and packaging processes. Figure 1.9 demonstrates how the DMD™'s

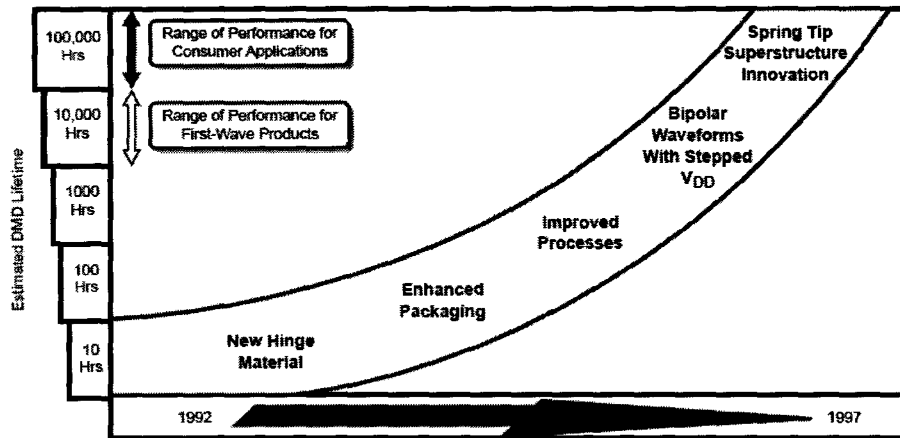


Figure 1.9: Reliability development and lifetime improvement of DMD™ [14].

lifetime has increased through the years and the changes which have made it possible [14].

The wear and tear on the moving parts of any mechanical device is expected to be detrimental to its operation over time. Both intuition and finite element analysis using bulk properties of aluminum pinpointed hinge failure caused by hinge fatigue to be the limiting cause of mirror failure in the DMD™. However, accelerated life tests performed at TI showed no signs of hinge fatigue even after $10^{12}$ cycles. The reason for this was attributed to the erroneous use of bulk material properties in the initial finite element analysis. It was shown that models based on the thin-film properties of metals better represented device test results [14]. Douglas explains that fatigue in bulk materials is caused by a build up of dislocations at the materials surface causing cracks as they accumulate which eventually leads to breakage. It has been postulated that thin films, such as the hinges in the DMD™, have two closely spaced free surfaces which oppose the formation of dislocations and therefore are unable to accumulate a high enough density of dislocations at the surface to cause any fatigue cracks. With updated models, TI has predicted at least ten years and as many as fifty years of normal DMD™ usage before any hinge breakage will occur.

Hinge failure has emerged however, as a life-limiting factor, albeit in a different

form: 'hinge memory'. In the ideal case, mirrors would switch back and forth between the 'ON' and 'OFF' positions spending equal amounts of time on either side. However, in reality mirrors may be placed in either direction for extended periods of time. As this occurs metal creep causes slight deformation in the hinges resulting in a residual tilt even when all voltages are removed. In small amounts, this has little to no effect on the operation of the device; however, when the residual tilt exceeds approximately $35 - 40\%$ of the maximum tilt angle the electrostatic attraction to one side will be consistently higher resulting in an effectively stuck mirror.

Temperature, time, stress, and materials all effect the amount of metal creep present in the system. With little to no control over the first three, TI turned to new materials to solve the problem of hinge memory. Through experimentation an aluminum alloy was selected for the hinge which increased the lifetime of the device by a factor of approximately 5. This modification was able to reduce the amount of hinge memory; however, it was not able to completely eliminate it. Therefore, to further increase the reliability of the DMD$^{TM}$ a 'bipolar reset' voltage waveform along with a stepped up address voltage, $V_{DD} = 7.5V$, was implemented. Both of these additions were used to increase the electrostatic attraction felt between the mirror and the desired landing electrode even with small amounts of residual tilt on the mirror.

Another common concern with the reliability of MEMS devices is the impact of surface adhesion. As devices scale down, so too does the ratio of volume to surface area. Therefore, forces relying on surface area become dominant on the small scales of MEMS devices. In the DMD$^{TM}$, this is represented by stuck mirrors. For example, when a mirror is mechanically latched down to one side it is possible that the surface of the mirror will stick to the landing site. The electrostatic force which then attempts to pull the mirror over to the other side is not enough to overcome this adhesion. As illustrated in figure 1.10, the solution to this problem was the addition of two spring tips to either side of the yoke. The springs perform two actions. First of all, this design minimizes the amount of surface area which comes into contact with the landing site. Secondly, the springs deform upon contact storing up energy which is released when the reset voltage waveform is applied pushing the mirror away from

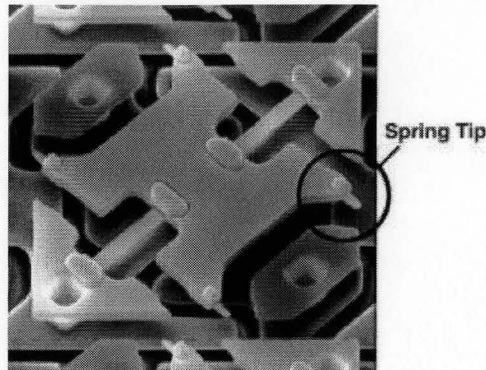


Figure 1.10: SEM image clearly showing the spring landing tip [14].

the landing site.

With a functionally reliable design, the final concern for the DMD$^{TM}$ is environmental robustness. Any dust or debris caught between or under the mirrors will easily damage the device. A humid environment in which moisture can build up on the surface could also be catastrophic. Therefore, the DMD$^{TM}$ is completely assembled in a class 10 clean room before being placed in a hermetically sealed package to protect the device from moisture, debris and other environmental effects that could be harmful to its operation. Current reliability predictions based on accelerated life tests estimate that the lifetime of the DMD$^{TM}$ is expected to be greater than 120,000 hours of normal use.

### DMD$^{TM}$ Applications

Although the DMD$^{TM}$ is still at the heart of TI's DLP$^{TM}$ technology, many research groups are actively working to establish other potential uses for the first commercially available micromirror array. A sample of the myriad of current and emerging applications being investigated have been listed in a paper produced by Dudley *et al.* [12]. While some of the early applications, such as photofinishing, lithography, and volumetric displays resemble the intended use of the DMD$^{TM}$ in a projection environment, the list continues to grow as more abstract applications are added. Switched

Blaze Gratings (SBG) for telecom dynamic filtering applications are being produced which take advantage of the DMD$^{TM}$'s diffractive properties for infrared light [17]. In microscopy applications, the DMD$^{TM}$ has been implemented to function as a dynamic aperture to switch between bright field and dark field as well as confocal microscopy [18, 19]. Spectroscopy applications make use of the DMD$^{TM}$ as both a chopper and an adaptive reflective slit to variably select appropriate wavelengths from a previously separated spectrum [20].

Adaptive optics, a technology used to measure and correct aberrations in wavefronts immediately before imaging, also stands to benefit from the MEMS micromirror technology; however, the DMD$^{TM}$ is typically overlooked in this context due to its inherent bistability [21].

## 1.2 Adaptive Optics

Adaptive optics (AO) is a technology established to compensate for the deteriorating effects of the medium through which an optical signal propagates. As an example, physical optics predicts that under ideal conditions the spatial resolution of an optical image will be limited by diffraction. In reality however, the diffraction-limit is rarely observed due to wavefront variations, known as aberrations, introduced by optical defects and nonhomogeneties inherent in the path of the optical signal. The effects of static defects can be removed with the addition of one or more perfectly positioned passive elements. Although, an active solution is required for dynamic disturbances such as those created by a turbulent atmosphere in astronomical imaging, or mircomuscle fluctuations of the eye when attempting to image the retina.

Many innovative approaches for the implementation of AO systems have been considered [22]. A schematic representing the most common design used for astronomical imaging is shown in figure 1.11 as a means of demonstrating the fundamental principles of a typical AO system [23]. In this diagram, light gathered by the telescope has been affected by the density variations in the earth's atmosphere. The amount of aberration in the incoming light is surveyed by a wavefront sensor and represented mathematically in terms of the Zernike polynomials [22, 24, 25]. This information is

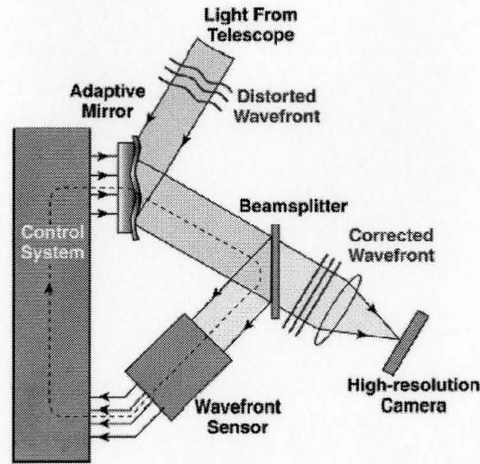


Figure 1.11: Fundamental principle of adaptive optics [23].

then passed through a control system which determines the appropriate amount of correction needed and distorts the shape of a deformable mirror corrective element accordingly. After the correction is applied, the wavefronts are again sampled and modifications to the correction are continuously updated through this closed-loop feedback system.

The wavy lines entering the system in figure 1.11 represent the aberrated wavefronts which under ideal circumstances would be plane waves. Therefore, it is the goal of the AO system to return the incoming phasefronts back into ideal plane waves resulting in a 'perfect' image. In theory, this can be achieved through the principle of phase conjugation. A diagram illustrating this principle is shown in figure 1.12 [22]. A plane wave traveling towards the mirror passes through a piece of glass with an index of refraction greater than 1. This retards the light passing through the glass, thus altering the wavefront. If the mirror deforms so that it takes the shape of the phase conjugate of the wavefront, the reflected wave will again pass through the glass and reverse its initial effect. Had the mirror not been deformed, the wavefront would have been doubly aberrated.

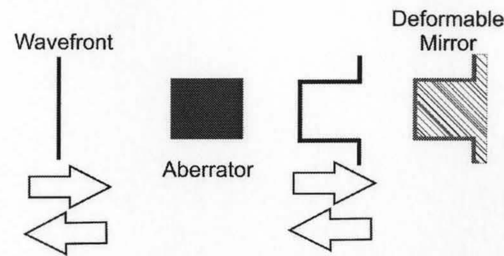


Figure 1.12: Example of phase conjugation.

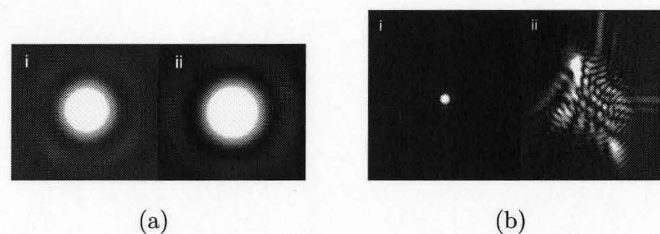


(a) (b)

Figure 1.13: Point spread function of the perfect human eye (i) vs. the typical eye (ii) as a function of pupil size: a) 1mm b) 7mm [29].

### 1.2.1 Vision Science

After decades of using adaptive optics solely for astronomical and beam propagating purposes, it is just recently becoming involved in vision science research for both improved vision and high-resolution retinal imaging [5, 21, 26, 27, 28]. Physical optics tells us that to decrease the point spread function, and therefore increase the spatial resolution, a larger aperture is needed. It is well known however, that the eye, much like an array of non-ideal optical elements, suffers from several monochromatic aberrations which become progressively worse with increasing pupil diameters. As such, it has been suggested that the eye's best optical performance is obtained with a pupil diameter of 3mm; roughly half the achievable pupil diameter of a human eye [27]. To illustrate the effects of aberration in the eye, a comparison of the point spread functions for a diffraction limited system versus that of the normal human eye is provided in figure 1.13 for pupil diameters of 1mm and 7mm [29].

Liang *et al.*, at the Center for Vision Science in the University of Rochester, have developed the first AO system designed to improve the optical quality of the human eye as well as to act as a fundus camera which allows imaging of individual photoreceptors in a living eye [27]. The group made use of a continuous face sheet conventional deformable mirror with 37 actuators supplied by Xinetics, Inc.. This device is commonly used in astronomical AO systems. With this system it was shown that aberrations in the eye up to the fourth Zernike order, including defocus, astigmatism, coma and spherical aberration, were significantly reduced while aberrations beyond the sixth order remained unchanged. Moreover, the authors suggested that by increasing the number of actuators of the deformable mirror higher order aberrations could plausibly be corrected.

The downfall of conventionally manufactured deformable mirrors, such as the one developed by Xinetics, Inc., is the enormous expense associated with them. A typical device costs about $1000 per actuator. Therefore, in recent years many researchers have turned their attention to microfabrication to greatly reduce the cost per actuator making systems with large numbers of correcting elements affordable [5, 21, 26, 28, 30]. These systems also offer a greater compatibility with vision science AO systems since smaller apertures require less pupil magnification. Two types of MEMS deformable mirrors are currently being pursued. Continuous face sheet mirrors deformed by arrays of piston actuators placed below the surface offer high optical efficiency and minimal diffractive effects; however, achieving a desired contour on the surface of the mirror requires complex control algorithms due to the mechanical coupling experienced between the actuators [30]. In addition, continuous face sheet devices also suffer from insufficient stroke [21].

A more promising, much simpler solution is the aforementioned segmented MEMS mirror arrays. Since each element in the array is completely independent, these devices offer the simplest control algorithms and can easily accommodate very large arrays. As previously noted however, low optical efficiencies and diffractive effects can plague these devices.

Using a $12 \times 12$ array of piston-only micromirrors, Cowan *et al.* successfully demonstrated the possibility of using a MEMS device in an AO system [28]. The array

| SPECIFICATION | XINETICS INC | BMC MEMS | TI DMD | IDEAL DM |
|---|---|---|---|---|
| Diameter (mm) | $\phi = 75$ | $33 \times 33$ | $12 \times 14$ | $\phi = 10$ |
| No. of Actuators | 97 | $12 \times 12$ | $1024 \times 768$ | 100 |
| Surface Type | Continuous | Continuous Piecewise | Segmented | Continuous /Segmented |
| Stroke (wavefront) | $\pm 4\mu m$ | $\pm 2\mu m$ | $\pm 4\mu m$ | $> 10\mu m$ |
| Response Speed | $4kHz$ | $3.5kHz$ | $\sim 10kHz$ | $100Hz$ |
| Operating Voltage | $100V$ | $220V$ | $\sim 10V$ | A few volts |
| Cost per Actuator | \$1000 | $\sim$ \$200 | \$0.01 | $\Downarrow$ \$ $\Downarrow$ |

Table 1.1: Comparison of the deformable mirrors used for aberration correction along with the requirements for an ideal array [31].

was placed in a system with intentionally added low order aberrations (defocus) while the point spread functions of the aberrated wavefronts and unaberrated wavefronts were compared. The MEMS deformable mirror performed reasonably well; however, limitations due to the low fill factor ($\sim 70\%$) were clearly visible. A lenslet array was also used in an attempt to increase the optical fill factor, although, this solution was found to greatly increase to complexity of alignment and performance was found to be limited for highly aberrated signals due to the geometry of the hybrid correcting element.

More recently, Doble *et al.* performed a comparison between the Xinetics deformable mirror used by Liang *et al.* and a MEMS mirror designed by Boston Micromachines (BMC) [21]. Both vision improvement and retinal imaging experiments proved that the achievable correction of the low cost MEMS mirror was easily comparable to the that of the conventional Xinetics deformable mirror. As a direct comparison, table 1.1 lists the features of the Xinetics deformable mirror, the BMC micromirror array, and TI's DMD$^{TM}$ as well as the ideal parameters for a deformable mirror corrective element [31]. It is evident from this comparison that the DMD$^{TM}$ has several attributes that are very appealing including its many actuators, quick response time, low voltages, size and most importantly: cost.

## 1.3 Problem Statement

The DMD™ has become a mature technology. It has surpassed the laborious design and development stage as well as TI's strict reliability standards and proceeded into full scale production. Many groups have already taken advantage of this fact and have introduced the DMD™ into a multitude of applications above and beyond its intended use in projection displays. While the majority of applications up to this point have employed the DMD™ in its digital form, there exists a potential to apply the device under different circumstances. As a prime example, the DMD™ possess qualities which make it extremely useful as a deformable mirror corrective element in the field of adaptive optics. Unfortunately, the digital nature of the device precludes its use in applications where a full range of analog positioning is required. Thus, the inherent bistability of the DMD™ must be overcome before the field of adaptive optics, among others, can take full advantage of this device.

Underlying control circuitry which obeys digital logic enables the seamless digital operation of the DMD™ while at the same time creates the major hurdle in achieving analog control. It is thus the aim of this thesis to suggest a method for analog operation based on precise input voltage waveforms and pulse width modulation techniques. In order to accurately develop this method, optical characterization and dynamic simulations are used to determine specific properties of the DMD™ micromirrors including natural frequencies, mechanical spring constants, and damping coefficients.

## 1.4 Outline

The fundamentals of electrostatic actuation are discussed in the following chapter. Instabilities which occur as a result of this form of control are presented and linked to the digital operation of the DMD™. In Chapter 3, the system used to capture the dynamic motion of the DMD™ micromirrors is introduced. The motivation behind the selection and the theory of operation of each component incorporated in the optical setup is explained. The method of automation required to measure the

deflection properties of multiple micromirrors across the DMD$^{TM}$ array is presented in Chapter 4. Statistical micromirror characteristics based on the experimentally recorded trajectories as well as the uniformity of the mirrors across the device are also reported. As a corollary of the acquired micromirror properties, simulations based on the Runge-Kutta numerical approximation are detailed in Chapter 5. The model established predicts the reaction of the DMD$^{TM}$ micromirrors to applied voltage waveforms and allows an investigation into the feasibility of DMD$^{TM}$ analog operation. The concluding chapter presents the contributions of this study and proposes some recommendations for future research.

# Chapter 2

# Electrostatic Actuation

Electrostatic actuation is commonly used in MEMS devices largely due to the simplicity of fabrication, low cost and power requirements, negligible temperature dependance, and the ability to perform large deflections. This type of actuation exploits the attractive coulomb force experienced between two charged surfaces of opposite polarity. A typical device design includes the removal of sacrificial material separating sets of electrodes in the final steps of fabrication to free up mechanically compliant capacitive structures. During operation, externally applied voltages pull the electrodes together while the stiffness in the mechanical structure works to keep them apart. Accurate positional motion is achieved by an equilibrium established between the attractive electrostatic force and the mechanical restoring force. The sections which follow examine the operational theory of electrostatic actuation and, more importantly, its application to the DMD™.

## 2.1 Parallel Plate Capacitor

Electrostatic devices resemble and are typically modeled as parallel plate capacitors. A parallel plate capacitor is simply two electrically conductive thin plates separated by an insulating dielectric medium which prevents the passage of charge from one plate to the other. The benefit of this device is that it is able to store a charge $Q$ proportional to the voltage $V$ that is placed across it. The constant of

proportionality which relates the stored charge to the applied voltage is referred to as the capacitance $C$ of the device:

$$Q = CV. \tag{2.1}$$

The insulating dielectric material between the plates in the capacitor ensures that all the charge stored in the device is constricted to the plates. This accumulation of charge on the surface of a large thin conductive plate will produce an electric field which can be approximately determined by the application of Gauss' law:

$$\oint_S \boldsymbol{E} \cdot d\boldsymbol{a} = \frac{Q_{enc}}{\epsilon_0}. \tag{2.2}$$

In doing so, the integration is performed over the surface of a 'Gaussian pillbox' of the same area $A$ as the plate with a thickness that extends into the area slightly above and below the plane. $Q_{enc}$ is the total charge enclosed in the box and hence the total charge stored on the plate $Q$. $\epsilon_0 = 8.85 \times 10^{-12} Fm^{-1}$ is the permittivity of free space. Since the electric field is perpendicular to the surface of a conductor, the integral need only be evaluated over the top and bottom surfaces of the box. All other components of the integral will be lost since the product $\boldsymbol{E} \cdot d\boldsymbol{a}$ is zero over the sides of the box. This leads to the following electric field

$$\boldsymbol{E} = \frac{Q}{2\epsilon_0 A}\hat{\boldsymbol{n}} \tag{2.3}$$

where $\hat{\boldsymbol{n}}$ is the unit vector pointing normal to the surface. By convention $\hat{\boldsymbol{n}}$ points outwards from the surface. Therefore, the field points upwards above the plane and downwards below it. If the second plate, which contains an equal and opposite charge $(-Q)$, is placed directly beneath the first, by the properties of superposition, the fields of the two plates will add together to form the total electric field. Since the second plate is oppositely charged, the field produced will be opposite to the field generated by the top plate. Meaning the field points downwards above the plate and upwards below it. Hence, by combining the fields, it is clear that they will cancel outside of the plates while combining constructively between them:

$$\boldsymbol{E} = \begin{cases} 0 & \text{out of plates} \\ \frac{Q}{\epsilon_0 A} & \text{between plates} \end{cases}. \tag{2.4}$$

This formulation implies the field is uniform in the area between the plates. Unfortunately, this is only the case for plates which extend out to infinity. For plates of finite dimension, the field will curl around the edges weakening the attractive force between the plates. This phenomenon, known as 'fringing fields', can generally be ignored if the separation distance is much smaller than the plate dimensions.

The capacitance can be determined by using the electric field to find the potential difference between the plates:

$$V(top) - V(bottom) = \int_{bottom}^{top} \boldsymbol{E} \cdot \boldsymbol{dl}. \tag{2.5}$$

If we assume that the top plate is held at a potential $V$ and the bottom plate remains connected to ground then

$$V = \frac{Qd}{\epsilon_0 A} \tag{2.6}$$

where $d$ is the distance between the plates. From equation (2.1), we see that the capacitance of the parallel plate configuration is

$$C = \frac{\epsilon_0 A}{d}. \tag{2.7}$$

In the presence of an electric field, the surface charges on either plate will undoubtedly experience a force given by Coulomb's Law: $\boldsymbol{F} = Q\boldsymbol{E}$. Therefore, the force on the upper plate is given by

$$F_e = \frac{Q^2}{2\epsilon_0 A} = \frac{C^2 V^2}{2\epsilon_0 A} = \frac{\epsilon_0 A V^2}{2d^2} \tag{2.8}$$

where the $\frac{1}{2}$ in this equation removes the force created by the charge $Q$ working on itself. This result shows that any potential difference applied across the plates will create an attractive force which pulls the plates together. The polarity of the applied voltage is of no concern since the charge on the plates will always arrange itself in such a way as to create a positive and negatively charged plate.

## 2.2 Mechanical Actuation

In a typical capacitor, the attractive force between the plates is always present. However, it is generally overlooked since both plates are rigidly held in position. If

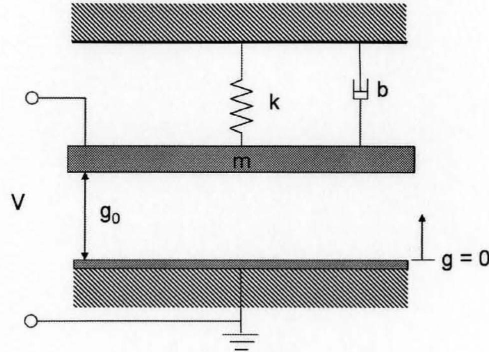


Figure 2.1: Schematic of the parallel plate capacitor model.

we now imagine that the top plate in our parallel plate capacitor is suspended by a spring as shown in figure 2.1, the electrostatic force will work against the stiffness of the spring to pull the plates together. Making use of Newton's law,

$$m\frac{d^2g}{dt^2} = \sum Forces, \tag{2.9}$$

we can derive the governing equation for this system. The forces acting on the system are the aforementioned electrostatic force $F_e$, the mechanical spring force $F_s$, and as illustrated by the dashpot in figure 2.1, a damping force $F_d$. Assuming the spring is linear, it follows Hooke's law,

$$F_s = k(g - g_0). \tag{2.10}$$

The damping force is proportional to velocity,

$$F_d = -b\frac{dg}{dt}. \tag{2.11}$$

Now recalling our result for the electrostatic force from the previous section, equation (2.8), and inserting it along with equations (2.10) and (2.11) into equation (2.9) we are left with

$$m\frac{d^2g}{dt^2} = -\frac{\epsilon_0 AV^2}{2g^2} - b\frac{dg}{dt} - k(g - g_0). \tag{2.12}$$

This is a nonlinear equation with respect to the separation distance $g$. As a result, the motion of the top plate versus time can not be solved analytically and must be determined using numerical methods.

## 2.3 Steady-State Solutions and the Pull-in Instability

If we restrict our attention for a moment to steady-state solutions the derivatives in equation (2.12) drop out and we are left with

$$k(g - g_0) = \frac{-\epsilon_0 A V^2}{2g^2}. \tag{2.13}$$

After rearranging this equation, it becomes apparent that positive feedback exists in this solution;

$$g = g_0 - \frac{\epsilon_0 A V^2}{2kg^2}. \tag{2.14}$$

An applied voltage across the plates will cause the gap to decrease; however, the amount that it decreases is also inversely proportional to the square of the gap. The consequence of this result is that the gap will decrease by larger and larger amounts as the separation distance between the plates shrinks. Eventually, this leads to an instability commonly referred to as pull-in (or snap-down) in which the mechanical restoring force of the spring is unable to compensate for the growing electrostatic attractive force and eventually causes the plates to collapse.

Following the formulation by Senturia [32], by evaluating the stability of the system it is possible to identify the exact position and voltage where the pull-in instability will occur. Stability analysis is performed by allowing a small perturbation to the separation distance between the plates and verifying whether or not the net force acting on the plates tends to return to the equilibrium position. Since we are still only concerned with the steady-state solutions the net force acting on the system is

$$F_{net} = \frac{\epsilon_0 A V^2}{2g^2} + k(g - g_0). \tag{2.15}$$

It is obvious from equation (2.13) that at a point of equilibrium $F_{net}$ will be zero. To evaluate how $F_{net}$ changes with a small perturbation of the gap, $g - \delta g$, we use

$$\delta F_{net} = \left.\frac{\partial F_{net}}{\partial g}\right|_V \delta g. \tag{2.16}$$

Thus, using (2.15),

$$\delta F_{net} = \left(k - \frac{\epsilon_0 A V^2}{g^3}\right) \delta g. \tag{2.17}$$

A stable equilibrium point will have $\delta F_{net}$ oppose a small change in the gap. Therefore, if $\delta g$ is negative, $\delta F_{net}$ must be positive to restore the system to the equilibrium point at $g$. If, on the other hand, $\delta F_{net}$ is negative the equilibrium point at $g$ is unstable since a small decrease in the gap results in a force tending to decrease it further. Hence, a stable equilibrium point will only occur when

$$k < \frac{\epsilon_0 A V^2}{g^3}. \tag{2.18}$$

As the applied voltage is increased, the gap diminishes according to equation (2.14) and the equilibrium will pass from stable to unstable at the point where the left and right sides of the above equation are equal:

$$k = \frac{\epsilon_0 A V_{PI}^2}{g_{PI}^3}. \tag{2.19}$$

This point represents the pull-in instability and the voltage at which this occurs is the pull-in voltage, denoted $V_{PI}$. Substituting this value for $k$ into (2.14), the separation distance at which pull-in occurs is simply determined by

$$g_{PI} = \frac{2}{3} g_0. \tag{2.20}$$

This is an interesting result which more plainly stated means that no stable solution exists for values of the gap which are less than $\frac{2}{3}$ that of the initial separation distance at rest. Using this result in equation (2.19), a value for the pull-in voltage can also be derived;

$$V_{PI} = \sqrt{\frac{8 k g_0^3}{27 \epsilon_0 A}}. \tag{2.21}$$

Figures 2.2 and 2.3 represent the above results graphically. The curved lines (**A**, **B** and **C**) in figure 2.2 depict the electrostatic force for applied voltages increasing from **A** to **C**. The intersections between these curves and the linear mechanical restoring force present the solutions to equation (2.13). The applied voltage responsible for **A** is below the pull-in voltage of the system. Therefore, the curve intersects the

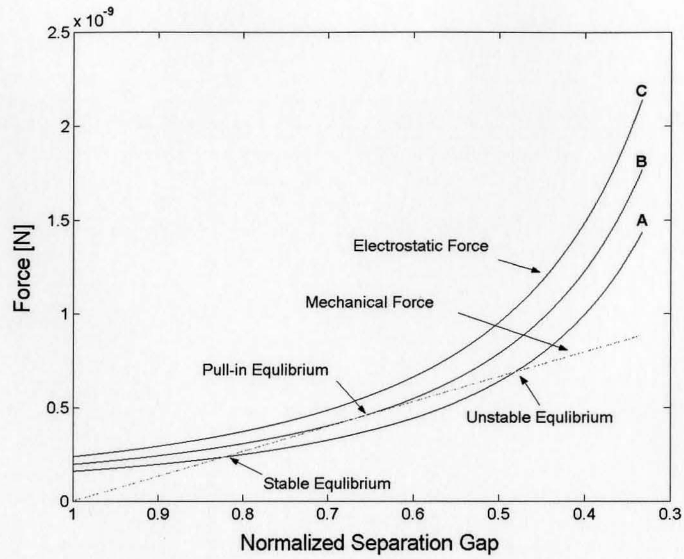


Figure 2.2: Comparison of mechanical and electrostatic torque.

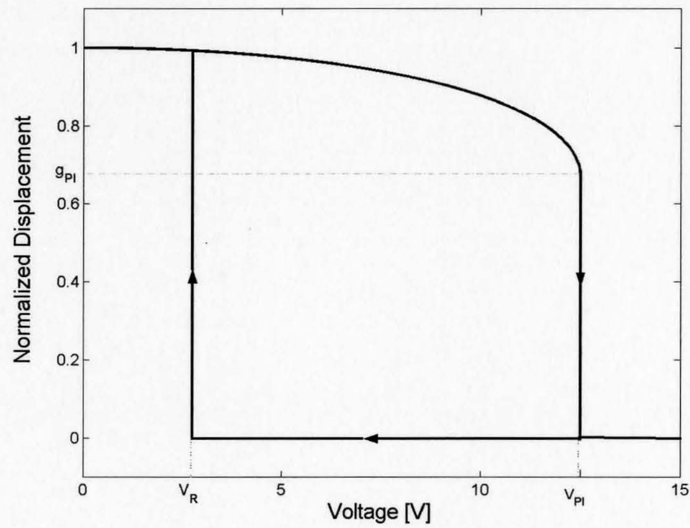


Figure 2.3: Snap down and hysteresis phenomena of electrostatic actuators.

mechanical restoring force at two separate displacements. According to equation (2.18), however, only the solution affiliated with the larger separation gap will be stable. For displacements between the equilibrium positions, the plate will return to the stable equilibrium point. Although, once the plate reaches the displacement of the second equilibrium point, stability is lost and the plates will collapse. As the voltage across the plates is increased, the equilibrium points visible on **A** will slowly move inwards until they coincide at a single point. This occurs for an applied voltage $V_{PI}$ as illustrated by **B**. The single equilibrium point which occurs at $g_{PI}$ will be unstable however, since (2.18) is not satisfied. The final curve (**C**) is the result of an applied voltage which is above $V_{PI}$ and therefore no equilibrium solutions exist.

If one was to continue drawing curves to represent all other possible voltages, the eventual result would be a complete set of stable solutions. These are combined and presented in figure 2.3 in a curve of normalized separation gap versus applied voltage. It can be seen that at exactly $V_{PI}$, and a separation distance of $\frac{2}{3}g_0$, the gap collapses to zero and no stable solutions exist past this point.

The hysteresis phenomenon experienced by electrostatic actuators is also presented in this diagram. Assuming the plates, when collapsed, are not in direct contact but instead held apart by a thin dielectric, a much lower voltage is required to send the upper plate back to its stable position. As mentioned previously, this occurs because the electrostatic attraction depends on the separation distance of the plates. With the plates nearly in contact, the capacitance increases dramatically creating a very strong electrostatic field. As the applied voltage is lowered past the release voltage $V_R$ the electrostatic force drops below the mechanical restoring force which lifts the upper plate back to a stable position.

## 2.4 Digital Operation

While the pull-in phenomenon is detrimental to the operation of some electrostatic devices, many designs, including that of the DMD$^{TM}$, make use of this phenomenon to provide maximum angular deflection and increase accuracy and reliability during operation. In the case of the DMD$^{TM}$, forcing the mirror into the snap-down regime

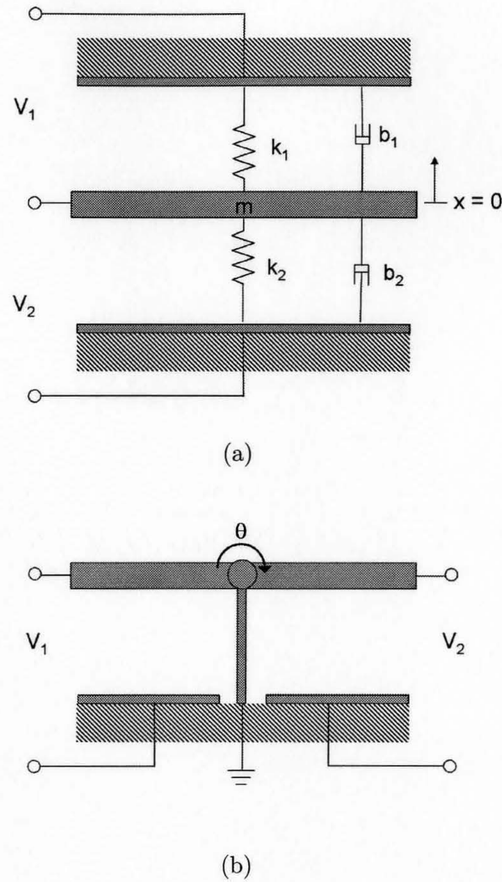


Figure 2.4: Comparison of a) parallel and b) torsional plate models.

by applying voltages in excess of $V_{PI}$ allows a mechanical stop to dictate the 'ON' and 'OFF' positions rather than a delicate balance of attractive and restoring forces.

Since the DMD$^{\text{TM}}$ has the ability to deflect in both the positive or negative directions, the equivalent parallel plate model would require an additional fixed plate above the other two as shown in figure 2.4(a). The middle plate is now free to move up and down depending on the applied potentials. A more realistic torsional representation of the DMD$^{\text{TM}}$ is also presented in figure 2.4(b). In order to achieve digital operation of the DMD$^{\text{TM}}$, it is possible to apply heightened voltages to the address electrodes on either side of the micromirror. However, it is advantageous to use digital

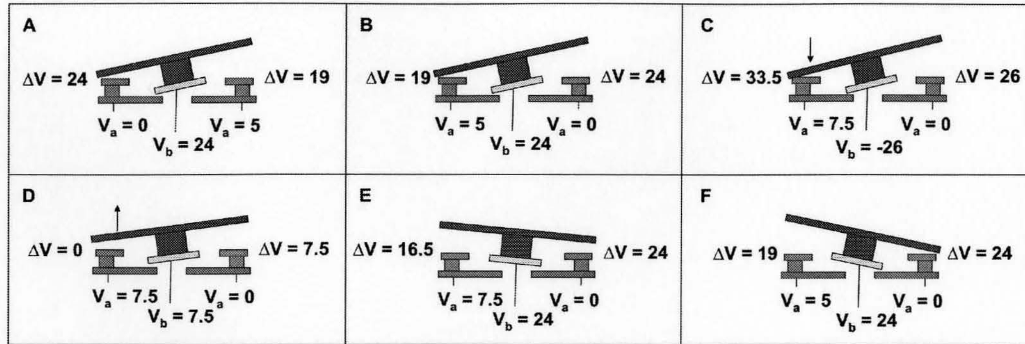


Figure 2.5: Schematic depicting the applied voltages and potential differences leading to the 'crossover' transition of the micromirror.

$0 - 5V$ operation in order to remain compatible with high density, standard CMOS addressing circuitry [6]. As a result, a differential bias voltage $V_b$ is applied to the mirror structure (and landing electrodes) to achieve the required elevated potentials. While the mirror is in its resting position, an applied voltage $V_b$ will result in zero net torque on the mirror unless a difference in voltage is present between the underlying address electrodes. As an example, the DMD$^{TM}$ 0.7XGA in conjunction with the DAD1000RST reset controller uses a constant (unless under reset condition) differential bias of $26V$ to achieve complete deflection of the mirror ($\pm 12°$). With the address electrodes set to 0 and $5V$, the mirror sees a greater attraction to the $0V$ electrode (potential difference of $26V$ as opposed to $21V$) and snaps down. The landing electrodes, which are held at the same potential as the mirror, protect the circuit from shorting out. Due to the hysteresis in the mirror displacement versus applied voltage, the underlying address electrodes are free to switch back and forth between 0 and $5V$ without effecting the mirror's position. Once the state of the address electrodes is appropriately set, a carefully designed reset waveform is applied through the differential bias to modify the state of the mirror. Figure 2.5 presents a schematic of a single mirror making the transition from one state to the other as a result of the reset bias. Initially, the differential bias drops, increasing the potential difference on the landed side of the mirror. Although this action seems counter intuitive, it results in mechanical energy being stored in both the torsional hinge as well as the spring

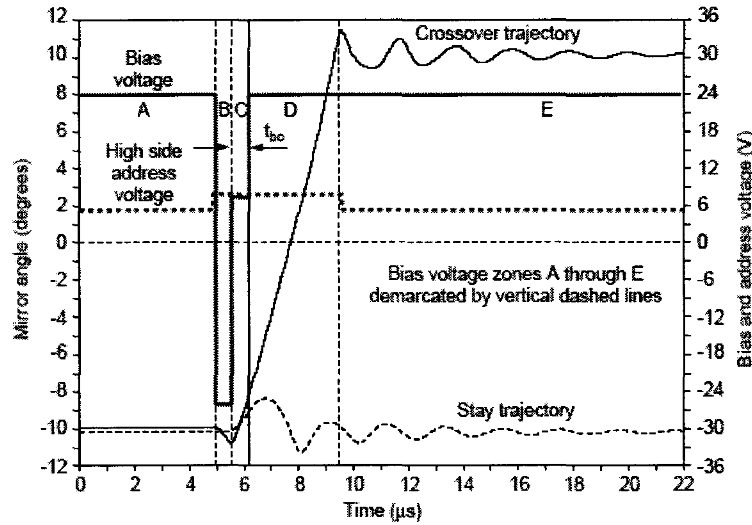


Figure 2.6: Simulated 'crossover' and 'stay' trajectories as well as the voltage reset waveform which drives the motion of the micromirror [33].

tips on the edge of the landed yoke. In the following step, the potential difference is removed from the landed side by shifting both the differential bias and the high address electrode to a stepped up voltage, $V_{DD} = 7.5V$. The stored mechanical energy is released pushing the mirror back towards the equilibrium position. As it approaches equilibrium however, the differential bias returns to $26V$, causing the mirror to pass through the equilibrium point and snap down on the opposite landing site.

A simulated graphical representation of the 'crossover' and 'stay' trajectories for a micromirror in the DMD$^{TM}$ array is presented in figure 2.6 [15]. Both the 'stay' and 'crossover' trajectories utilize the same reset waveform; although, due to the arrangement of the address voltages, different torques are produced in either case and hence the resulting trajectories are visibly different.

## 2.5 Free Oscillations

Several system parameters can be determined by observing of the unforced behavior of a device. For example, if the voltage securing a mirror in the latched position

is suddenly removed, the electrostatic attractive force drops to zero and the mirror is free to travel back towards its mechanical resting position. The mirror will follow a path given by the solution to the following equation:

$$\frac{d^2x}{dt^2} + \gamma\frac{dx}{dt} + \omega_0^2 x = 0. \tag{2.22}$$

This is simply equation (2.12) in which the electrostatic force has been set to zero. As well, two new constants have been defined for convenience: $\omega_0 = \sqrt{\frac{k}{m}}$ is the natural frequency of the system and $\gamma = \frac{b}{m}$ is the damping coefficient. Since 2.22 is a second-order, ordinary differential equation, it can be solved analytically by applying the trial solution $x = Ae^{i\alpha t}$. This leads to the following quadratic equation

$$-\alpha^2 + i\alpha\gamma + \omega_0^2 = 0 \tag{2.23}$$

which can be easily solved for $\alpha$;

$$\alpha = i\frac{\gamma}{2} \pm \sqrt{\omega_0^2 - \frac{\gamma^2}{4}}. \tag{2.24}$$

Therefore, by superposition, the general solution will be a combination of the two solutions,

$$x = e^{-\frac{\gamma t}{2}}(Ae^{i\omega_\gamma t} + A^* e^{-i\omega_\gamma t}) \tag{2.25}$$

where $\omega_\gamma = \sqrt{\omega_0^2 - \frac{\gamma^2}{4}}$. Since $x$ must be real valued the coefficients in equation (2.25) must be complex conjugates. As long as the system is not overly damped the mirror will sinusoidally decay towards the rest position. A particular solution to this problem can be determined by substituting the initial conditions $x = x_0$ and $\frac{dx}{dt} = v_0$ at $t = 0$ into both equation (2.25) as well as its time derivative. Therefore, the complete solution for the trajectory of the mirror is given by

$$x = e^{-\frac{\gamma t}{2}}\left[x_0 \cos\omega_\gamma t + \frac{2v_0 + \gamma x_0}{2\omega_\gamma}\sin\omega_\gamma t\right]. \tag{2.26}$$

Since the micromirror is originally at rest in the latched position (either 'ON' or 'OFF'), its initial velocity is zero ($v_0 = 0$). This leads to a slight simplification of equation (2.26), which can be written as

$$x = x_0 e^{-\frac{\gamma t}{2}}\left[\cos\omega_\gamma t + \frac{\gamma}{2\omega_\gamma}\sin\omega_\gamma t\right]. \tag{2.27}$$

A convenient way of describing the damping of an oscillating system is provided by the quality factor $Q$. The quality factor represents the energy loss of the system per cycle compared to the stored energy in the system. Using the values obtained above the quality factor is given by

$$Q = \frac{\omega_\gamma^2 + \omega_0^2}{2\gamma\omega_\gamma}. \tag{2.28}$$

# Chapter 3

# Optical Setup

Characterization techniques which make use of non-contact methods are essential for determining the experimental behavior of MEMS devices due to the small size and fragility of microstructures. Integrated sensors have been used to achieve contact free characterization of MEMS devices; however, this method greatly increases the complexity of fabrication[34]. Therefore, in post-fabrication, optical techniques are most commonly used.

Many commercially available systems use a variety of interferometric techniques to provide three dimensional optical characterization of MEMS devices, although these systems are generally bulky and expensive. While characterization methods based on spot optical measurements can not provide the three dimensional information of interferometric designs, it is possible that these detection systems are sufficient to provide a complete investigation of the fundamental rotational mode of a torsional micromirror [35].

Several examples of spot optical detection systems used to characterize torsional micromirrors exist in the literature [8, 35, 36]. In the first example, Fischer *et al.* couple light reflecting off of a deflected micromirror into a moveable fiber which outputs the light onto a photodiode. In this way, only the static behavior of the micromirror can be measured since the reflected light is manually coupled into the fiber [8]. In the second method, the reflected light falls incident on two carefully spaced photodiodes. Based on the intensity measurements recorded, the deflected

angle can be indirectly determined [36]. This method is capable of capturing dynamic response, although extensive post measurement calculations are required to retrieve this information. A third method, able to monitor the dynamic behavior without the need for extensive post measurement calculations, is presented by Annovazzi-Lodi *et al.* [35]. Here a position sensitive detector (PSD) replaces the photodiodes in the previous method. Unlike the photodiodes, the PSD is able to directly measure the angular deflection of the micromirror by tracking the movement of the reflected spot as it travels across the surface of the detector. The PSD outputs a voltage which is directly proportional to the position of the spot and can be continuously monitored by means of an oscilloscope or multimeter. Since a complete characterization of the DMD$^{TM}$ depends on both the static and dynamic behavior of the device, this final method presents the most appropriate solution.

## 3.1 Design

The optical setup designed to actively measure the angular deflection of a single mirror in the DMD$^{TM}$ array is presented in figure 3.1. The light from a Helium-Neon (HeNe) laser (632.8nm), with the help of two alignment mirrors, is directed through a 20X objective in order to reduce the lasers spot size. The beam is focused onto an individual micromirror by translating the DMD$^{TM}$ array in two dimensions using a motorized motion controller. As the mirror being examined rotates, the reflected light is collected by two aspheric lenses and relayed onto a bidirectional PSD. An oscilloscope as well as a collection of multimeters record the output of the PSD.

### 3.1.1 Beam Propagation

An ideal laser produces a pure $TEM_{00}$ Gaussian mode beam. The Gaussian beam, which represents a solution to the wave equation, has the smallest angular divergence of the wavefront normals permitted for a given beam width [37]. The term 'Gaussian' is used not for the shape of the wavefront as it is for 'spherical' and 'plane' waves but for the intensity distribution which is a circularly symmetric Gaussian function

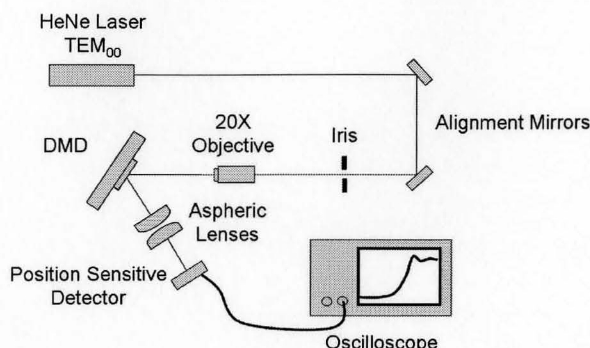


Figure 3.1: Schematic of the optical setup.

centered about the optical axis in any transverse plane. The laser specifications distributed by JDS indicate that the HeNe laser used in this optical setup (JDS 1107P) emits a beam constrained to greater than 95% in the $TEM_{00}$ mode. Thus, it is assumed that the beam produced is purely Gaussian and will propagate according to the theory of Gaussian beam optics.

The time independent complex amplitude of the Gaussian beam is given by

$$U(r) = A_0 \frac{W_0}{W(z)} \exp\left[-\frac{\rho^2}{W^2(z)}\right] \exp\left[-jkz - jk\frac{\rho^2}{2R(z)} + j\zeta(z)\right] \tag{3.1}$$

where $A_0$ is a constant, $\rho^2 = x^2 + y^2$, $k = \frac{2\pi}{\lambda}$ is the wavenumber, and $\zeta(z)$ is the phase retardation. $W(z)$, $W_0$, and $R(z)$ are the beam width, the beam waist, and the radius of curvature of the wavefronts, respectively, and are given by the following equations:

$$W(z) = W_0 \left[1 + \left(\frac{z}{z_R}^2\right)\right]^{\frac{1}{2}} \tag{3.2}$$

$$W_0 = \left(\frac{\lambda z_R}{\pi}\right)^{\frac{1}{2}} \tag{3.3}$$

$$R(z) = z \left[1 + \left(\frac{z_R}{z}^2\right)\right]. \tag{3.4}$$

With the parameter $z_R$, known as the Rayleigh range, and the wavelength $\lambda$, all other parameters can be determined.

The optical intensity, $I(r) = |U(r)|^2$, is a function of the axial and radial distances $z$ and $\rho$;

$$I(\rho, z) = \frac{2P_0}{\pi W^2(z)} \exp\left[-\frac{2\rho^2}{W^2(z)}\right] \tag{3.5}$$

where $P = \frac{1}{2}|A_0^2|(\pi W_0^2)$ is the total power carried by the beam. This is a Gaussian distribution which widens as it propagates away from the beam waist ($z = 0$) in both the positive and negative directions along the optical axis. At any position along the optical axis $z$, a circular aperture extending a distance $W(z)$ radially outwards from the axis will collect 86% of the total power. Approximately 99% of the total power is contained within a circular aperture of radius $\frac{\pi}{2}W(z)$. A single micromirror in the DMD$^{\text{TM}}$ array has dimensions of $12.68\mu\text{m} \times 12.68\mu\text{m}$; therefore, to collect all the light on a single mirror the width of the incident beam must be focused to approximately $4\mu$m giving a spot size ($2W_0$) of less than $8\mu$m.

The rate at which a Gaussian beam diverges is dependent on the spot size of the beam. As shown in equation (3.2), for $z \gg z_0$ the beam radius increases linearly with $z$:

$$W(z) = \frac{W_0}{z_0} z = \theta_0 z. \tag{3.6}$$

With the help of equation (3.3) it can be seen that the angular divergence is proportional to the ratio of wavelength to spot size:

$$\theta_0 = \frac{2}{\pi} \frac{\lambda}{2W_0}. \tag{3.7}$$

A consequence of this result is that beams which are squeezed down to smaller spot sizes diverge much more quickly. Thus, a beam incident on a single mirror will diverge (in the far field) at a rate of 0.05rad/m. The beam diameter will grow to 5mm after traveling a distance of 5cm. As the beam size increases, collection of the reflected light while recording its motion becomes extremely difficult. Hence, a relay system of lenses is necessary to properly capture the reflected light.

### Beam Focusing

As a Gaussian beam passes through a thin lens of focal length $f$ its complex amplitude given by equation (3.1) is multiplied by the complex amplitude transmittance

of the lens: $\exp(jk\rho^2/2f)$. This additional phase factor modifies the wavefront while leaving the beam width unaffected. The phase of the transmitted beam is

$$kz + k\frac{\rho^2}{2R} - \eta - k\frac{\rho^2}{2f} = kz + k\frac{\rho^2}{2R'} - \eta \tag{3.8}$$

where $R'$ satisfies the imaging equation

$$\frac{1}{R'} = \frac{1}{R} - \frac{1}{f}. \tag{3.9}$$

Using the transmitted radius of curvature $R'$ and the known beam width, equations (3.2) and (3.4) can be combined to calculate the new waist radius of the beam

$$W_0' = \frac{W}{[1 + (\frac{\pi W^2}{\lambda R'})^2]^{\frac{1}{2}}}, \tag{3.10}$$

and the distance to the beam waist

$$z' = \frac{R'}{1 + (\frac{\lambda R'}{\pi W^2})^2}. \tag{3.11}$$

Substituting equations (3.3), (3.4), and (3.9) back into equation (3.10) allows the new beam waist to be represented in terms of focal length $f$, the distance from the initial beam waist to the lens $z$, and the initial beam waist $W_0$:

$$W_0' = \frac{\left|\frac{f}{z-f}\right|}{\left(1 + \frac{W_0^2 \pi}{\lambda (z-f)^2}\right)^{\frac{1}{2}}}. \tag{3.12}$$

Solving this equation for the focal length,

$$f = z\frac{\left[W_0'^2 - \frac{W_0^2 W_0' \pi}{\lambda z}\left[W_0^2 - W_0'^2 \frac{\lambda^2 z^2}{W_0^2}\right]^{\frac{1}{2}}\right]}{W_0'^2 - W_0^2}, \tag{3.13}$$

allows a lens to be selected based on the existing and desired beam waists. Since the beam exits the laser with a waist of $W_0 = 0.24$mm and the required beam radius incident on the micromirror is $W_0' = 4\mu$m the needed focal length varies between approximately 9mm to 13mm depending on the distance $z$ between the laser and the lens. As is evident from equation (3.13), as $z$ decreases, the required focal length is shortened. Shorter focal lengths require shorter distances between the lens and

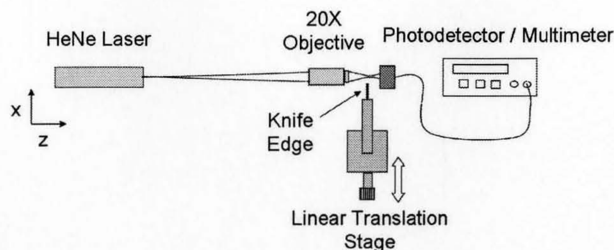


Figure 3.2: Schematic of the setup used in a knife edge test.

the DMD$^{TM}$ array. Therefore, longer focal lengths are desired to keep the optical elements from piling up. From the range of focal lengths determined, a 20X objective (Mitutoyo 20X) was chosen to provide the appropriate amount of beam focusing. This objective also has the advantage of having a long working distance of 20mm which enables it to be placed further away from the DMD$^{TM}$; thus, easing some of the spatial constraints.

**Knife Edge Test**

A knife edge technique was used to determine the width of the beam at various positions in the optical setup[38]. In this method, as demonstrated in figure 3.2, a knife edge positioned perpendicular to the optical axis was slowly shifted laterally through the beam in small increments to block or allow light (depending on the direction of the knife) to pass into the detector. Using equation (3.5), the power transmitted by the knife edge at some position $z$ is given by

$$P(x) = \int_{-\infty}^{\infty}\int_{x}^{\infty} \frac{2P_0}{\pi W(z)^2} \exp\left(-\frac{2(x^2+y^2)}{W^2(z)}\right) dxdy \tag{3.14}$$

$$= \frac{P_0}{2}\left[1 - erf\left(\frac{\sqrt{2}x}{W(z)}\right)\right]. \tag{3.15}$$

A plot of the normalized power $P(x)/P_0$ in figure 3.3 shows how the amount of transmitted light varies as the knife moves in the $x$ direction across a Gaussian beam of width $W$.

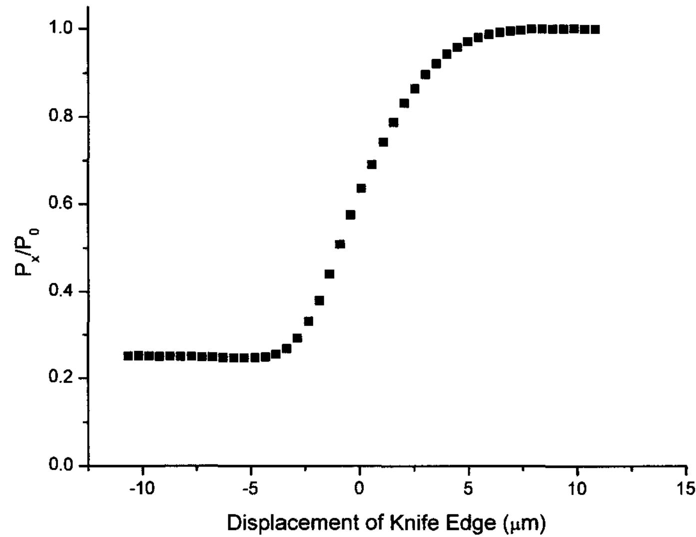


Figure 3.3: Plot of the data collected representing the integral of a Gaussian function.

Sets of knife edge measurements were performed both directly in front and after the objective. The first set was used to ensure the divergence of the beam exiting the laser was as predicted by the specifications supplied by JDS. The second set was used to verify that a spot size of $8\mu$m was achieved. In both cases, a Newport ESP300 motion controller was used to accurately place and record the position of the knife in the $x$ and $z$ axes. The knife was moved across the beam in submicron increments while the light intensity incident on the detector was recorded through a multimeter. The data collected was fit with equation (3.15) to determine the width of the beam. The waist was found by shifting the knife along the optical axis while recording width measurements at small intervals. The results of several measurements performed after the objective are presented in figure 3.4. This diagram clearly shows the beam focusing down to a spot size of less than $8\mu$m ($2W_0$).

One disadvantage of the knife edge test is that only two dimensional data is available ($x$ and $z$). A third axis, and a great deal of time, is required to perform three

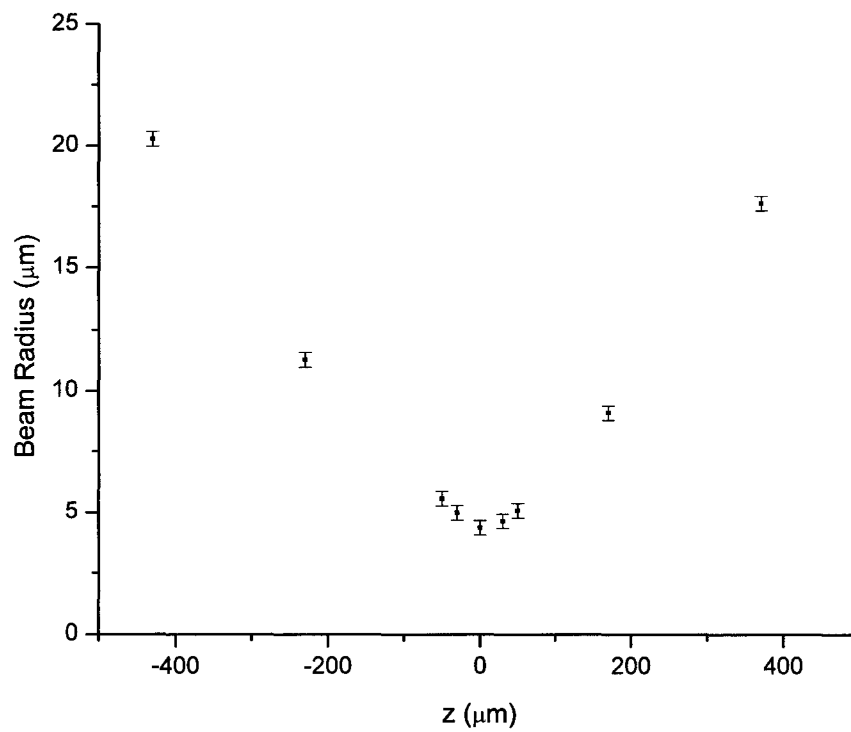


Figure 3.4: Beam width measurements.

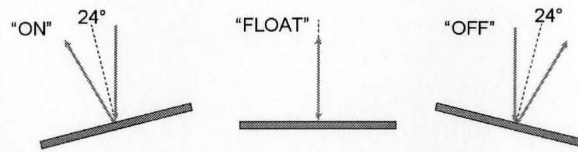


Figure 3.5: Schematic representing the increase in optical angle as a result of reflection.

dimensional measurements. In this respect, a beam profiler is extremely advantageous.

### 3.1.2 Collection Lenses

Each mirror in the DMD$^{TM}$ array has the ability to rotate ±12° about its torsional hinge. As depicted in figure 3.5, this physical angle of 24° translates into an optical angle of 48°. Thus, to capture the reflected light from both the 'ON' and 'OFF' positions a detector of width $d$ would need to be placed at most a distance $d$ away from the DMD$^{TM}$. This ignores the size of the beam. As such, to limit the expense of the system, smaller detectors are desired and thus must be placed in very close proximity to the DMD$^{TM}$. Alternatively, a set of relay lenses, positioned further away, can be used to collect the beam and direct it towards the detector placed at a distance. This is shown in figure 3.6. The detector can be positioned before or after the point $2f$ (twice the focal distance of the lens system); however, for positions after $2f$ the image will be inverted. At exactly $2f$, no beam movement will occur as the mirror is deflected, thus resulting in a loss of information. Therefore, to record the largest lateral translation it is advantageous to move the detector as far away from $2f$ as possible, in either direction, while still collecting light on the detector from the extreme micromirror deflections.

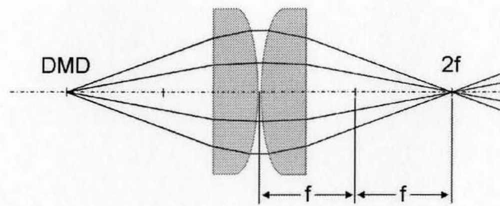


Figure 3.6: Two lenses acting as an optical relay to increase the separation distance between the detector and the DMD$^{\text{TM}}$.

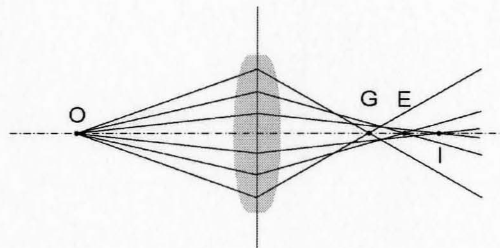


Figure 3.7: Spherical aberration.

### Spherical Aberration

In geometrical optics it is generally assumed that all rays are paraxial; that is, rays which are close to and make small angles with the optical axis. This allows approximations such as $\sin\theta \approx \theta$ and $\tan\theta \approx \theta$ to be used with little repercussion [39]. However, as the rays begin to deviate from the paraxial limit, these approximations are no longer valid, thus obscuring the validity of the 'perfect' imaging predicted by these equations. Instead, distortions, known as aberrations, begin to appear.

For non-paraxial rays, the use of spherical surfaces in common lenses leads to spherical aberration, as illustrated in figure 3.7. Rays passing through the lens close to the optical axis meet at the predicted paraxial image point **I**, while rays entering the lens further off axis meet at an axial image point, such as **E** or **G**, completely distinct from that of **I**. A difficulty which arises from this is selecting the most appropriate

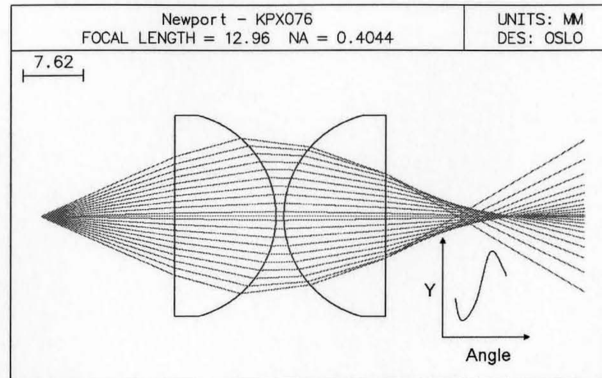


Figure 3.8: OLSO ray tracing diagram of a poor lens in terms of spherical abberation.

position along the optical axis to place the detector. Since we are determined to measure the trajectory of the mirror versus time, it is important that the angular positions of the mirror, from negative to positive, create monotonically increasing (or decreasing) voltages at the detector. If this were not so, two angular positions of the mirror would generate an identical measurement on the detector making it impossible to differentiate between the two.

Optical modeling software, OSLO 6.0, was used to test the spherical aberration in several off-the-shelf spherical lenses. An image plane, formed of the same dimensions as the detector, was placed in various positions along the optical axis to find positions of monotonically increasing values. Several lenses were modeled; however, the severity of the spherical aberration in each case made this task impossible. The ray tracing diagram produced using OSLO 6.0 for one of the modeled lenses (Newport KPX076) is presented in figure 3.8.

### Aspheric Lenses

Aspheric lenses provide a solution to spherical aberration. By modifying the surface of the lens away from the standard spherical shape, it is possible to align the image points of all rays, paraxial or otherwise. Without designing the perfect surface for each specific application however, it is difficult to completely eliminate all

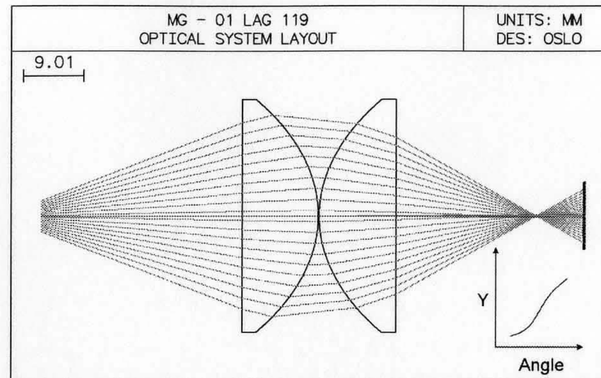


Figure 3.9: OLSO ray tracing diagram of the selected aspheric lens in which spherical aberration has been minimized.

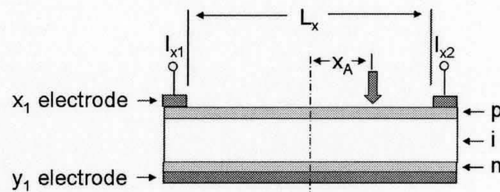


Figure 3.10: Functional diagram of a position sensitive detector.

spherical aberration. Since a small amount of spherical aberration is tolerable and custom designs are both complicated and expensive, off-the-shelf molded aspheric lenses were chosen. Figure 3.9, in comparison with figure 3.8, presents the benefit of using aspheric lenses. The spherical aberration, although not completely eliminated, is negligible. Based on the results obtained with OSLO and satisfaction of the spatial constraints, a set of plano-aspheric lenses from Melles Griot was chosen for the optical setup: 2 $\times$ 01 LAG 011.

### 3.1.3 Position Sensitive Detector

A lateral-effect position sensitive detector (PSD) offers a convenient way of measuring or tracking the position of an optical beam. The basic design of a PSD is similar to that of a large-area p-i-n photodetector with uniform resistive layers formed on the front and back surfaces of a high-resistivity semiconductor substrate. Positional information is extracted via current division through electrodes placed on either end of the resistive layers. When a light spot strikes the PSD, an electric charge proportional to the intensity of the light is generated at the point of incidence. By current division, the amount of charge which moves towards either electrode is inversely proportional to the distance which separates it from the point of incidence. Since the layers have a uniform resistance, the currents through the electrodes $I_{x1}$ and $I_{x2}$ can be determined by the following equations:

$$I_{x1} = \frac{\frac{L_x}{2} - x_A}{L_x} I_0, \tag{3.16}$$

$$I_{x2} = \frac{\frac{L_x}{2} + x_A}{L_x} I_0. \tag{3.17}$$

$I_0$, in the above equations, is the total photocurrent produced. $L_x$ is the length between the $x$ electrodes and $x_A$ is the distance between the incident spot and the center of the detector as shown in figure 3.10. Hence, the position of the beam can be accurately determined by calculating the difference between the measured currents at opposite ends of the device,

$$I_{x2} - I_{x1} = 2x_A I_0. \tag{3.18}$$

From this result, it is clear that the measured position of the beam is dependant on the intensity of the incident light. It is therefore common practice to divide the current difference by the current summation giving a result which is independent of intensity,

$$\frac{I_{x2} - I_{x1}}{I_{x2} + I_{x1}} = 2x_A \tag{3.19}$$

The PSD selected (Pacific Silicon Sensors DL100-7PCBA) was premounted on a printed circuit board with a built-in transimpedance amplifier so that voltages, instead of currents, were output. On extracted measurements, the difference voltage

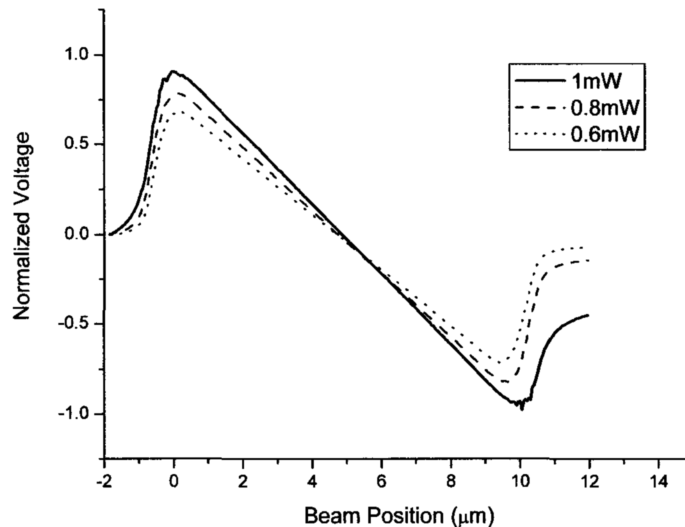


Figure 3.11: Normalized PSD output voltages for moving beams of varying intensity.

was divided by the summation voltage; however, this did not completely eliminate intensity variations as is evident from figure 3.11. For this reason, it was important to control the intensity fluctuations on the detector mainly due to background lighting. Rather large offset voltages ($\sim$ 100mV) were also present on the sum and difference voltages at the output of the detector and needed to be removed before normalization.

Although the linearity of this PSD was claimed to be 1%, data collected showed that this value dropped off considerably near the edges. Figure 3.12 presents the normalized voltages obtained for a grid of 121 evenly spaced light spot positions on the detector. The spot size of the beam used was 0.5mm and the spacing between adjacent points was 0.95mm. The linearity on the $x$-axis was better than 4% while the linearity on the $y$-axis fell to $\sim$ 45% near the top and bottom edges of the detector. The repeatability of the detector was also tested by randomly selecting 20 points from the grid and reacquiring data for those points. Repeatability was found to be better than 2%. Due to the reasonable repeatability but poor linearity of the PSD,

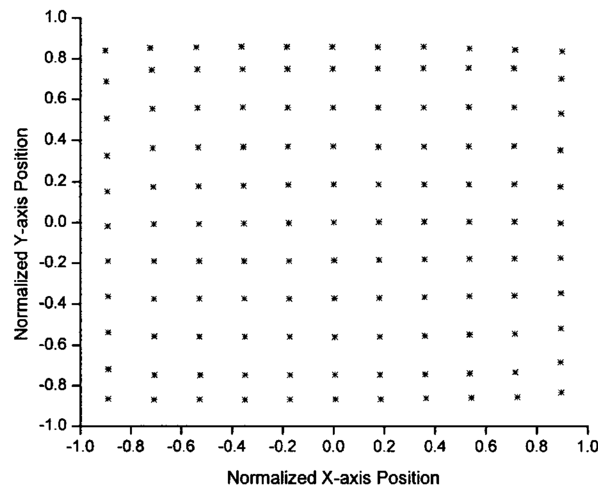


Figure 3.12: Measured linearity of the PSD.

an extensive positional calibration was necessary.

### PSD Bandwidth

The experimental bandwidth of the PSD was determined by positioning a LED, powered by the square wave output of a function generator, directly in front of the detector. The frequency produced by the function generator was varied from 100Hz to 1MHz while monitoring the peak to peak value of the voltage waveform output from the detector. As the frequency increased this value slowly trailed off providing the transfer function presented in figure 3.13. From the data collected, the -3dB bandwidth of the PSD used in this optical setup was determined to be $\sim$ 295kHz which compared closely to the expected value of 257kHz found on data sheets provided by Pacific Silicon Sensor.

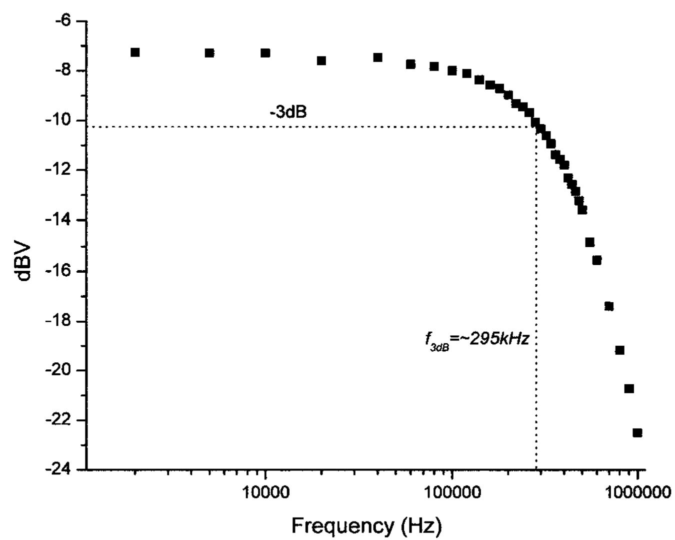


Figure 3.13: PSD transfer function.

### 3.1.4 Motion Controllers

The DMD™ was fixed to a dual axis translational stage positioned by motorized linear actuators (CMA-12CCCL) and a Newport ESP300 motion controller. Due to the minute size of the individual micromirrors in the DMD™ array, the submicron motion of the motorized actuators was necessary to align the incident beam onto a single micromirror. An electrostrictive actuator (Newport AD-30) and controller (Newport ESA-C) were also used to manipulate the focus of the objective.

The Newport ESP300 was computer controlled via the standard serial communication protocol (RS232) and automation was programmed using LabView 7.0. By automating the system, hundreds of micromirrors could be consecutively aligned and tested without user intervention.

### 3.1.5 Spatial Modeling

In conjunction with selecting the proper optical components for the measurement system a virtual three dimensional (3D) model was created using AutoCAD 4.0 to extinguish any spatial concerns. The benefit of 3D modeling is that it ensures that all components selected fit together in the allotted space before components are ordered, tested, and discovered to be too large for the rest of the setup. In this way, optical angles were also determined to provide the best fit of the optical components. The 3D model developed in AutoCAD 4.0 is visible in figure 3.14.

### 3.1.6 DMD Discovery™ 1100

For development purposes, Texas Instruments distributes the Discovery 1100 Starter Kit which includes a DMD™ chip (0.7 XGA) premounted on a printed circuit board equipped with the driving circuitry for the device. The Controller Board also provides an external connection for PC interfacing via USB 2.0 as well as a 5V power connection. A software package able to relay user initiated commands to the device through the USB connection is also provided in the kit.

The benefit of obtaining the DMD™ chip in this fashion is that it allows for

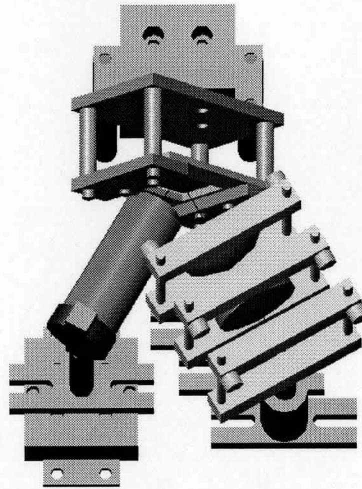

Figure 3.14: AutoCAD model of optical setup in close proximity to the DMD$^{TM}$ clearly representing the spatial constraints of the system.

instant access to the capabilities of the device. The included software provides three main commands: *LOAD*, *RESET*, and *FLOAT*. The *LOAD* command allows black and white image files to be loaded into the memory of the device. The *RESET* command triggers the bias reset voltage waveform while *FLOAT* clears the voltages and allows the mirrors to return to their mechanical resting positions.

In order to apply arbitrary voltages to the DMD$^{TM}$, the chip must be removed from the controller board. However, the connection of voltage signals to the 164 pins on the back of the device is made much simpler by the Discovery 1100 kit since the pinouts are also included in the documentation.

## 3.2 Alignment

Using dimensions determined with the 3D spatial model, an aluminum plate was machined to fix the DMD, the collection lenses and the PSD to the optical bench at the desired angles and positions. Each component of the system was individually introduced starting from the laser and alignment mirrors. Before introducing all other

components, a parallel beam was produced by reflecting the output from the HeNe laser off of the two alignment mirrors. The beam was directed through two variable apertures, at equal heights, separated by approximately 30cm. The second aperture was intentionally placed at (or very near) the focus of the objective. This was done to provide a minimal spot size at the aperture when the objective was later introduced.

Next, both the DMD and the PSD were secured to the aluminum plate. Voltage was removed from the device allowing the mirrors to rest in a flat position. The detector was then adjusted to position in incoming beam at the zero position (center of PSD). The aspheric lenses were then added one at a time and adjusted so that the measured beam on the detector remained at the zero position.

Alignment of the objective was complicated by the degrees of freedom allowed by the apparatus. The objective was held in an optical stand placed on a 2-axis linear translation stage. One axis was used to manipulate the focus while the other controlled the horizontal positioning of the objective. Both the vertical and the rotation adjustments of the objective were done manually. Proper alignment of the objective was thought to be achieved when light at its output was passed through the aperture placed directly in front of the objective, through the optical elements already in place and onto the zero position of the detector.

## 3.3 Calibration

Several factors lead to the requirement for a positional calibration of the PSD as a means of easily converting voltage readings to angular measurements. This include: the poor linearity of the detector, the difficulty of accurately measuring the distance between the DMD$^{TM}$ and the PSD, and the complicated optical effects of the collection lenses. A further problem, which arises due to the orientation of the rotational axes, is an arc-like trajectory traced out by the reflected beam. This is a result of the micromirror's rotational axis being aligned orthogonal to the angle of the incoming beam. The system was designed this way due to spatial constraints as well as to provide equal amounts of propagation through the protective glass covering the DMD$^{TM}$. The theory of the arc trajectory is presented in Appendix A.

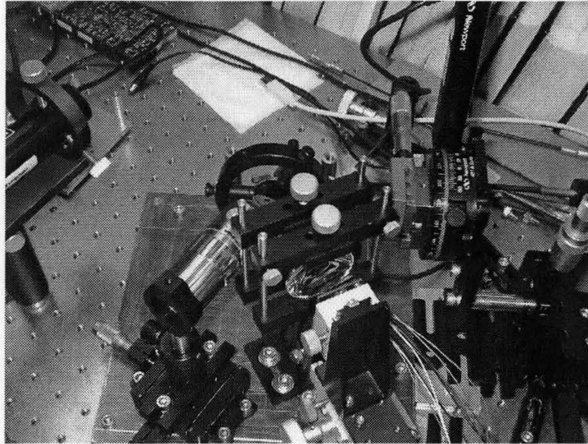

Figure 3.15: Setup providing angular calibration of the optical characterization system.

An accurate calibration was performed by replacing the DMD$^{TM}$ array with a single macromirror held by a rotational translation stage. The mirror was rotated through 28° with a motorized linear actuator (Newport CMA-12CCCL) while positional data was recorded from the PSD. A picture of the calibration setup is provided in figure 3.15.

Optical intensity was monitored very closely during calibration due to the intensity dependence of the PSD. A variable optical attenuator was placed at the output of the laser to reduce the intensity of the reflected light from the macromirror to equal the intensity reflected by the micromirror.

Accurate positioning of the macromirror was essential to the calibration. To achieve similar beam trajectories with both mirrors, the calibration mirror had to be placed in the exact same position as the micromirror. To confirm this, the DMD$^{TM}$ was set in place and the micromirrors were switched from the 'OFF' position to the 'ON' position while $x$ and $y$ voltages were recorded on the oscilloscope. The DMD$^{TM}$ was then replaced with the calibration mirror and its position was manipulated to conform to the same trajectory as seen by the micromirror. This was relatively difficult to achieve because the incident beam must strike the calibration mirror on

the rotational axis to mimic the results of the micromirror. As such, the macromirror was set on a three axis linear translation stage. The first axis controlled the height of both the mirror and rotational axis (rotational axis does not need to cross the center of the mirror) while the second manipulated the lateral position of the mirror relative to the rotational axis. The third was used to laterally shift both the mirror and the rotational axis to the position of the micromirror. The final calibration curve, shown in figure 3.16, was eventually found by trial and error.

Calibration of the detector eliminates the need for positional data along the $x$-axis since the angular deflection of the mirror can be entirely determined by the position of the beam along the $y$-axis as shown in figure 3.16(b).

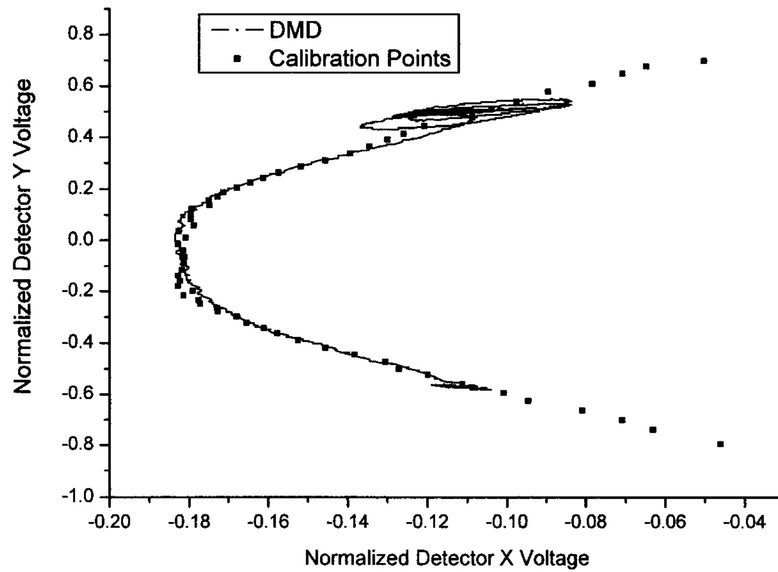


(a)

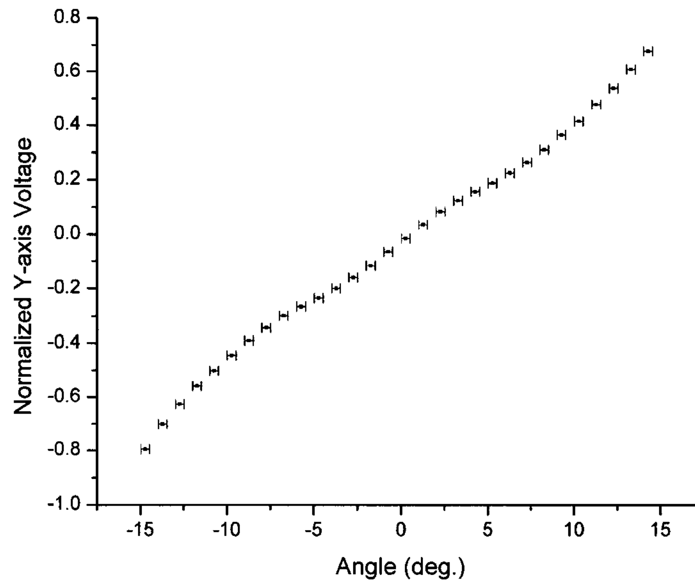


(b)

Figure 3.16: Calibration curves of the optical setup: a) $x$ and $y$ position of the reflected beam while sweeping through an angle of 28°, b) Height of the reflected beam versus sweep angle.

# Chapter 4

# Experimental Results

Direct measurements following the trajectory of an individual $DMD^{TM}$ micromirror versus time were performed with the optical setup described in Chapter 3. In using this setup, the dynamic response of the micromirror could be observed through three distinct transitions. For each tested mirror, the 'crossover', 'stay' and 'float' trajectories were recorded. Moreover, each of these measurements provided insight into the characteristics of the $DMD^{TM}$.

The natural frequency and quality factor of the system were easily realized through the 'float' transition or the transient decay of the micromirror. In this case, the micromirror begins in one of two deflected states ('ON' or 'OFF') before the bias voltage is removed. The lack of electrostatic force holding the mirror in place allows the mirror to freely oscillate back to its mechanical equilibrium position. This is an example of a damped oscillating system, which was discussed in §2.5. From the frequency of the oscillations and the decay of the exponential envelope, an experimental value for both the natural frequency and the quality factor of the system were determined.

In addition, the 'stay' and 'crossover' trajectories of the mirror describe the motion of the system during the application of the bias voltage reset waveform. Depending on the state of the address electrodes, the mirror is either sent quickly across to the opposite side ('crossover') or only allowed to move slightly away from the stable state before being immediately pulled back ('stay'). The information provided by these trajectories led to the evaluation of switching and stabilization times as well as

resting angles for the 'ON' and 'OFF' states.

## 4.1 Automated Experimental Design

Automated testing was necessary in order to perform measurements on a large number of micromirrors in the DMD$^{TM}$ array. As discussed in Chapter 3, computer automation of the motion controller, oscilloscope and multimeters was achieved using the standard communication interfaces: GPIB, and RS232. As well, the state of the micromirrors were programmed using a USB 2.0 connection supplied by the Discovery 1100 controller board.

A program written in National Instruments' LabView was designed to position the DMD$^{TM}$ such that the incoming beam was aligned to a specific mirror in the array. The mirror under test was then cycled through a series of transitions while recording the angular trajectory as a function of time. Due to the speed of the transitions, the oscilloscope was set to trigger on the appropriate slope and hold the trace for each transition while the data was transferred to the computer. After completing a set of desired tests, the automated system was programmed to move to the subsequent mirror and repeat the preceding process.

The state of a mirror in the DMD$^{TM}$ array is assigned by black and white images loaded into the memory of the device, with each pixel in the $1024 \times 768$ image defining the state of an individual micromirror. As such, black and white images were created with a preselected set of mirrors to be tested. This poses a problem for randomly selecting mirrors throughout the array since generating an image file requires manually selecting individual pixels. Thus, a set of 384 mirrors were periodically selected by generating a $64 \times 32$ pixel section to be used 384 times on a $1024 \times 768$ pixel image.

In order to begin testing, the DMD$^{TM}$ was manually aligned to the first preselected mirror to be tested in the top left corner of the array. As testing of the initial mirror was completed, the DMD$^{TM}$ was automatically shifted to the subsequent mirror along the path shown in figure 4.1 and automatically aligned. However, due to the mechanical constraints of the linear actuators manipulating the motion of the DMD$^{TM}$, only 160 of the 384 selected mirrors could be tested.

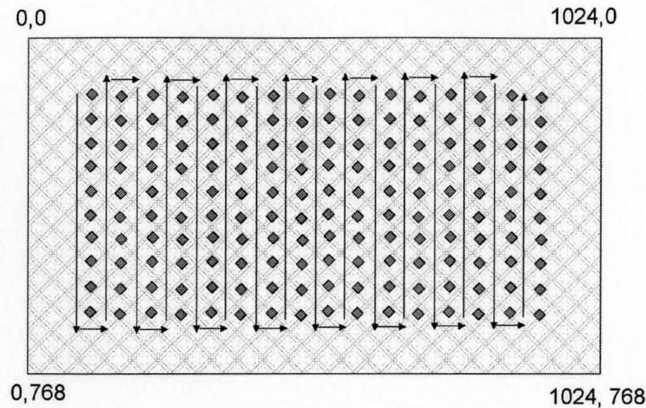


Figure 4.1: Automated test path of the DMD$^{TM}$.

### 4.1.1 Alignment Procedure

The alignment process for the initial mirror was performed manually. This was achieved by setting the target mirror and several of the mirrors directly surrounding it to their 'ON' state while placing all other mirrors in the array to the 'OFF' state. As the DMD$^{TM}$ was scanned across, the PSD monitored the position of the reflected light. An increase in voltage - meaning an increase in the average height of the reflected beam - was an indication of greater alignment. Rings of surrounding mirrors were slowly deflected to their 'OFF' position as the alignment was focused in on the desired mirror.

Motion of the DMD$^{TM}$ was accurately controlled with motorized linear actuators manipulated by a motion controller. Submicron increments, $0.2\mu$m, were used as means of ensuring maximum positional control during the final stages of the alignment. When the best transverse alignment was found, the focus of the objective was manipulated with an electrostrictive actuator. It became evident, however, that the best possible alignment only captured $\sim 60\%$ of the maximum intensity. This was likely the result of an astigmatism in the incoming beam caused by the misalignment of the objective; a problem which had been undetected in earlier beam width

measurements due to the one dimensional limitation of the knife edge test. Despite further attempts to better align the objective, the astigmatism in the beam persisted. Figure 4.2 presents three dimensional plots of the incoming beam measured at three positions along the optical axis. Specifically, figure 4.2(a) and 4.2(c) clearly show the approximate vertical and horizontal beam waists occurring at different points, whereas figure 4.2(b) presents a larger symmetric minimum positioned between the individual waists. These measurements were captured by shifting a single deflected mirror across the beam in a two dimensional rectangular area and recording the intensity of the reflected light on a photodetector. As a result, the measurements provided in figure 4.2 are in fact slightly larger than the actual beam dimensions due to a convolution between the shape of the individual micromirror and the cross section of the beam.

Once the initial alignment was accomplished, only a slight automatic adjustment for all other mirrors was required. To maintain the alignment of the previous mirror, the DMD$^{TM}$ was shifted by a calculated amount relative to its previous aligned position. The amount of the needed shift was evaluated using the path described by 4.1 and the known mirror center-to-center pitch of $13.68\mu m$. This distance, however, had to be translated to accommodate for the 45° rotation of the DMD$^{TM}$ about the optical axis. Once the DMD$^{TM}$ was positioned on the new mirror, a quick realignment routine was performed. The DMD$^{TM}$ was passed through $\pm 10\mu m$ in the $x$ direction and returned to the position providing the highest voltage at the PSD. The same procedure was then performed in $y$. Because automated manipulation of the focus was not possible with this setup, any misalignment in the focus could not be corrected. This did not appear to pose a problem however, as alignment values recorded for all 160 tested mirrors showed $\sim 60\%$ of the incident light was collected in each case.

## 4.2 Results

When automated testing of the DMD$^{TM}$ was completed, a Visual Basic for Applications (VBA) program was designed to cycle through the collected data in order to convert voltage readings taken from the oscilloscope into angular positions of the

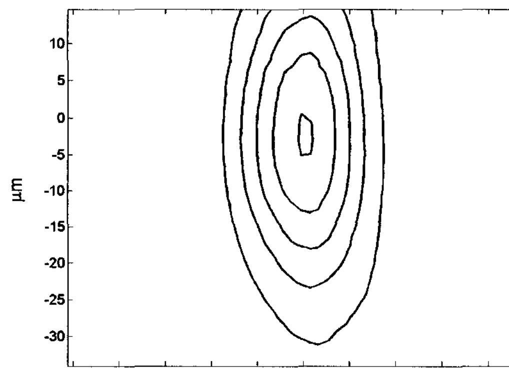


(a)

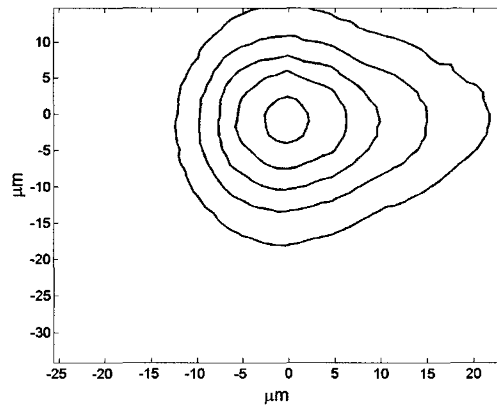


(b)

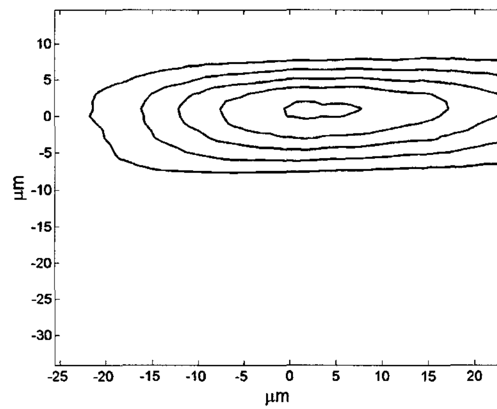


(c)

Figure 4.2: Profile of the astigmatic beam in the approximate focal positions along the a) $x$-axis b) $x$ and $y$-axis and c) $y$-axis.

micromirror. This process was based on the calibration described in Chapter 3. Some examples of the resulting trajectories for each transition are shown in figures 4.3(a) and 4.3(b). Figure 4.3(a) clearly depicts the mirror freely oscillating from the deflected 'ON' state to a mechanically stable position, while figure 4.3(b) represents the measured trajectories for both the 'stay' and 'crossover' transitions. As well, the recorded voltage reset waveform which triggers the motion of the mirrors is also depicted in this figure. Comparing figure 4.3(b) to previously published simulations of the micromirror trajectory shown in figure 2.6, there are some obvious discrepancies, most predominantly, between the initial peaks of the micromirror's transient motion at the landing site. Several possible explanations were proposed for these differences, including bending of the micromirror surface upon contact with the substrate. However, it is now understood that this discrepancy is a consequence of the detector's inadequate frequency response. The measured -3dB bandwidth of $\sim$ 295kHz for the PSD used in this optical setup was presented in Chapter 3. This was originally believed to be sufficient for switching times of $\sim 2\mu$s ($f = 250kHz$), although higher order components were ignored in this assumption. This hypothesis was verified through simulations performed with the model introduced in a subsequent chapter combined with the measured frequency response of the detector. Further, it was determined that filtering the higher order frequencies only slightly affects the measured switching time of the micromirror, thus suggesting that the results obtained using this setup should be considered equally valid.

### 4.2.1 Natural Frequency and Quality Factor

Data sets describing the trajectory of the micromirrors for the 'float' transition were fitted to the free oscillation model developed in Chapter 2. A Levenberg-Marquardt nonlinear fitting routine was programmed to iteratively determine the best fit values for $\omega_\gamma$ and $\gamma$ to match the model defined by equation (2.27) to the micromirror trajectory based on the minimization of $\chi^2$. Once $\omega_\gamma$ and $\gamma$ were known, values for the natural frequency $\omega_0$ and the quality factor $Q$ were simply determined

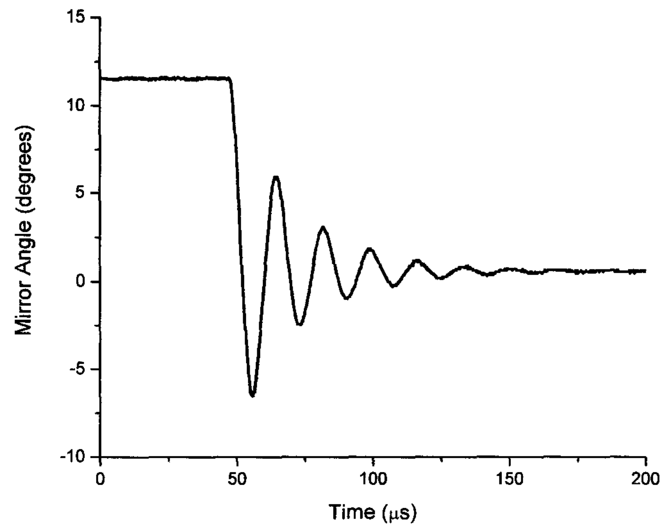


(a)

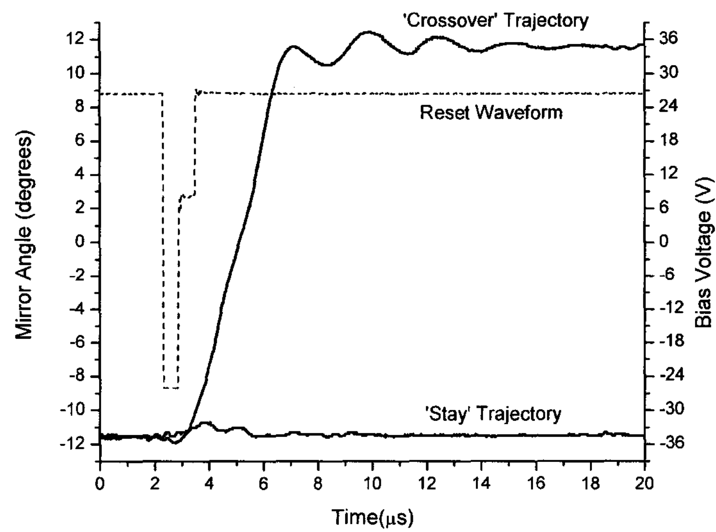


(b)

Figure 4.3: Experimentally recorded a)'float' trajectory and b)'stay' and 'crossover' trajectories.

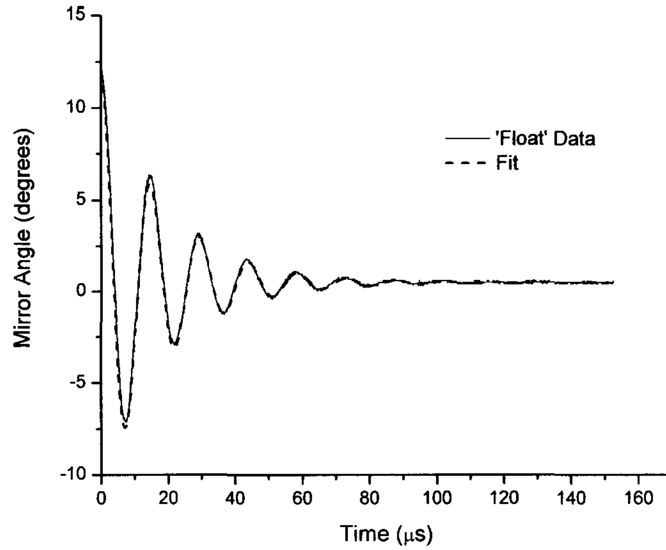


Figure 4.4: Measured 'float' transition along with the respective fit.

using the following equations:

$$\omega_0 = \sqrt{\omega_\gamma^2 + \frac{\gamma^2}{4}} \tag{4.1}$$

$$Q = \frac{\omega_\gamma^2 + \omega_0^2}{2\gamma\omega_\gamma}. \tag{4.2}$$

Figure 4.4 provides an example of one mirror's 'float' trajectory accompanied by its respective fitting curve. In observing this figure, it is important to note that the mirror does not come to rest in the 'flat' position (0°) as is expected for a symmetrical system; rather, an equilibrium position is found at $\sim 0.5°$. The same phenomenon is visible when the mirror is issued the 'float' command while fixed in the 'OFF' state; only the rest position occurs at $\sim -0.5°$. This indicates that the voltage is not completely removed from the device. In fact, it is believed that while the bias voltage is set to zero, one of two complementary address voltages remains in the high state ($5V$). As the 'float' command is issued the bias voltage is immediately removed while the state of the address electrodes are switched. This prevents the mirror from

| | $f_0$ (kHz) | $\sigma$ | $Q$ | $\sigma$ |
|---|---|---|---|---|
| 'ON'-'Float' | 68.4 | 0.2 | 4.05 | 0.04 |
| 'OFF'-'Float' | 68.3 | 0.2 | 3.75 | 0.03 |

Table 4.1: Mean values for $f_0$ and $Q$ for 160 tested mirrors.

snapping down on the opposite landing site as it oscillates. The small voltage which remains on the device slightly affects the path taken by the micromirror as it oscillates. However, drawing from the results of simulated trajectories, values obtained for $\omega_0$ and $Q$ from perturbed oscillations (as opposed to a completely unforced decay) differ by less than 4%.

Statistical data collected over the 160 tested mirrors is presented in table 4.1. The 'float' transition was initiated while the mirrors were positioned in both the 'ON' and 'OFF' states; hence, two sets of data are displayed in the table. The most notable observation from table 4.1 is that the variation from mirror to mirror is impressively small. For both sets of transitions, $\omega_0$ varies by less than 0.5% across the device while the variation in the $Q$ is limited to about 1%. A comparison of the two data sets, however, reveals a large discrepancy between the quality factor of a mirror leaving from the 'ON' state with that of a mirror departing from the 'OFF' state. The reason for this was hypothesized to be attributed to the mirror's rotational axis being positioned horizontally. Thus, depending on the starting position of the mirror, its initial motion is either helped or hindered by gravity as it rotates. However, a calculation of the gravitational torque inflicted on each micromirror reveals a torque on the order of $10^-18$N·m. This is $10^6$N·m less than the torque produced by the torsional hinges and therefore must have little affect on the motion of the micromirrors. Since the quality factor is predominantly affected by the amplitude of the beam, it is reasonable to assume the discrepancy seen here is an issue of calibration and not an asymmetry built into the device itself. To verify this, the DMD™ was rotated by 90° and retested. The results showed a similar pattern albeit in the opposite direction. Mirrors issued the 'float' command from the 'OFF' position had a mean quality factor of $3.98 \pm 0.07$ while mirrors issued the 'float' command

from the 'ON' position had a mean quality factor of $3.74 \pm 0.05$. Fits performed on the raw voltage data produced larger gaps between the two sets of quality factors. Thus, the calibration was found to reduce many of the nonlinearities in the system but failed to completely remove all such problems.

While there exists only a small variation in the natural frequency across the device, the spatial plot provided in figure 4.5(a) clearly depicts the positional dependence of $\omega_0$ over the array. A plane which was fit to the data (fig. 4.6) shows a 0.5° incline toward the lower right corner of the device (1024,768). Some initial doubt was cast on these results, however, due to the fact that the visible increase in the measured natural frequency of the micromirrors roughly follows the test path presented in figure 4.1. Thus, to eliminate thermal effects caused by radiation absorption and device heating as the cause for the discovered trend, the previously selected 160 mirrors across the device were retested albeit in the reverse order. As expected, the same positional dependance was visible for tests performed in either direction - removing thermal effects as the root cause. Thus, the observed variation across the device is most likely caused by errors inherent in the fabrication process of the array. The deviation in $\omega_0$ across this particular device equates to a 3% variation in the spring constant of the micromirror structure assuming an approximately constant moment of inertia. This leads to a 1% (or $\sim$ 1nm) variation in the thickness of the hinges which can be easily accounted for through the cosine distribution of the sputtering process. The thickness distribution of a thin-film deposited by a single point source is given by [40]

$$\frac{d}{d_0} = \frac{1}{[1 + (l/h)^2]^{\frac{3}{2}}}, \tag{4.3}$$

where $d_0$ is the thickest deposit and $l$ and $h$ are the radius of the sample and distance from the source to the sample respectively. This formula predicts the film thickness will drop quickly for reasonable dimensions, however, several optimizations can be performed in which multiple sources placed in specific locations increase the uniformity of film thickness. Because the specifics of TI's deposition system are unknown, it is difficult to predict the uniformity of the hinge thickness over the entire 200mm diameter wafer.

The effects of hinge thickness variations of the digital operation of the device

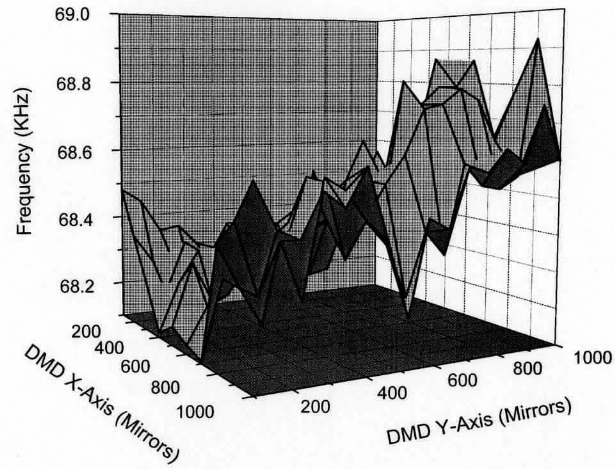


(a)

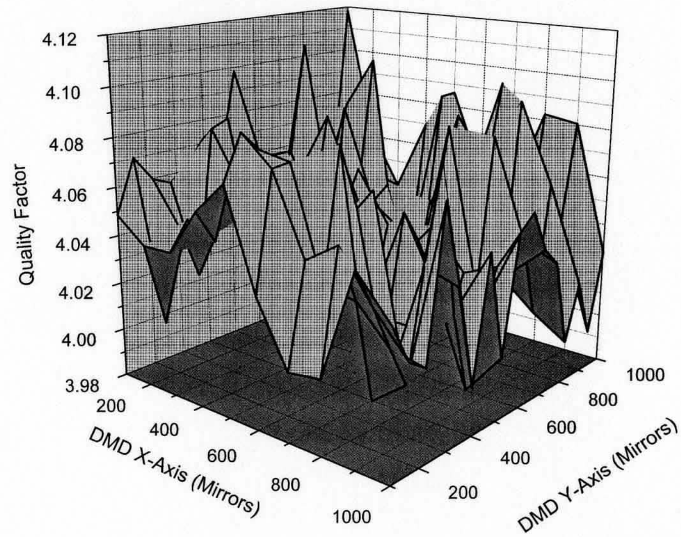


(b)

Figure 4.5: Uniformity of the DMD$^{\text{TM}}$: a) Positional dependence of $\omega_0$. b) Variation of Q over the device.

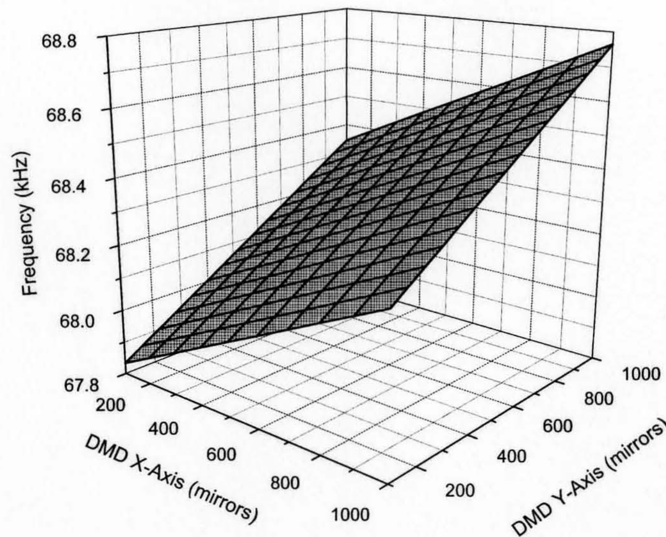


Figure 4.6: Planar fit produced of the natural frequency data showing a 0.5° incline towards the lower right corner of the device (1024,768).

are small compared to the effects caused to analog operation. At the dimensions of the DMD$^{TM}$, a small change of a few percent in the torsional spring constant of the hinges leads to a fluctuation of the pull-in voltage on the order of 10%. Since projection applications operate the device in the snapdown regime where applied voltages are far greater than the pull-in voltage, this has little effect on its digital operation. However, precisely controlling the analog positioning of the micromirrors will greatly depend on voltage levels very near the pull-in voltage.

As demonstrated in figure 4.5(b), trends in the Q value are not nearly as obvious. In fact, planar fits applied to several sets of quality factor measurements show very small yet opposing trends in the data. These are the result of uncertainties in the measurements as opposed to a positional dependence across the device. Correlation calculations performed on the same sets of quality factor measurements to predict a relationship between the quality factor and natural frequency values also presented conflicting results. Thus, any apparent correlation discovered was expected to be a result of the distribution of random errors in the measured Q values.

Uncertainty in the natural frequency measurements as a result of random errors can be determined by removing the systematic variation across the device. This was achieved by subtracting the planes fit to each set of data revealing a normal distribution in the measured values of $\omega_0$. With the systematic variation removed, the standard deviation of the natural frequency measurements, as a result of random errors, decreased to 0.1kHz. Histograms describing the distribution of the measured values for both $\omega_0$ and Q are given in figure 4.7.

### 4.2.2 Switching Time

The literature detailing previous generations of the DMD™ chip identifies two representations of switching times [15]. The optical switching time has been previously defined as the rise time of the light pulse as the light from the rotating mirror enters the projection lens pupil. This definition is slightly misleading, however, as it provides a measurement of the time necessary for the mirror to move from $0°$ to $12°$ but ignores the time required for the mirror to travel from $-12°$ to $0°$. Therefore, the optical switching times presented in this section refer to the measured time for a mirror traveling the full distance from $\mp 12°$ to $\pm 12°$. The mechanical switching time is simply an extension of the optical switching time, which also includes the settling of the mirror prior to being latched in its new position.

The optical switching speed of the mirrors was determined by measuring the time required for a mirror to travel from 10% to 90% of the total angular deflection. Typical switching times of $\sim 3\mu s$ were recorded across the device which compare well with previously reported switching times of $\sim 2\mu s$ albeit using an alternate definition. Statistical results presented in table 4.2 show little variation between the mirrors, with both 'ON'-'OFF' and 'OFF'-'ON' switching times remaining reasonably close.

The mechanical switching time was more difficult to measure, thus facilitating a further discrepancy between the mirrors. Times were calculated from the point the reset voltage waveform was triggered to the time when the mirror had settled to 10% of its peak transient motion. Due to the difficulties caused by the bandwidth of the detector, these measurements were somewhat inaccurate given that the initial peak of

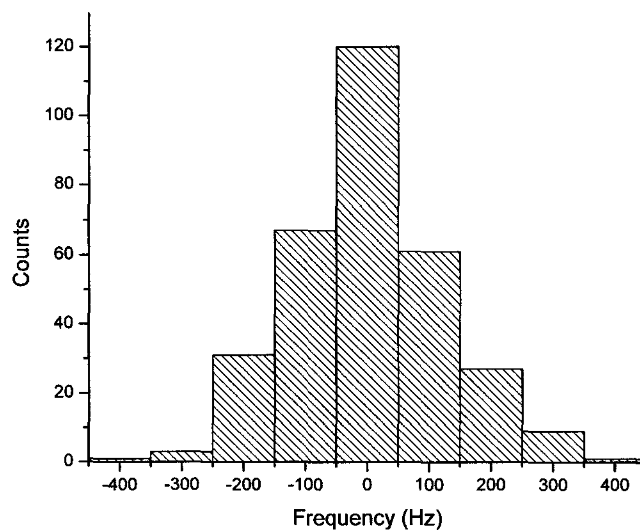


(a)

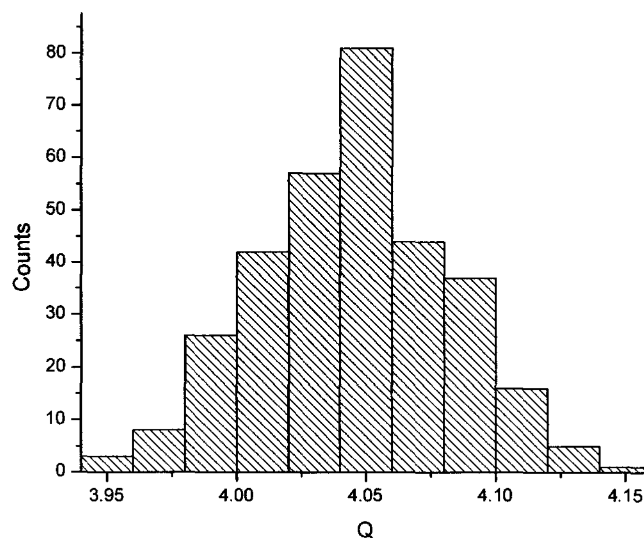


(b)

Figure 4.7: Distribution of the measured a)$\omega_0$ and b) Q values with systematic variations removed.

| | Mean ($\mu$s) | $\sigma$ |
|---|---|---|
| 'ON'-'OFF' | 3.10 | 0.03 |
| 'OFF'-'ON' | 3.09 | 0.03 |

Table 4.2: Mean optical switching times of 160 tested mirrors.

the transient motion was filtered out. The mean mechanical switching time of the 320 measured 'crossover' trajectories was found to be 15.8$\mu$s with a standard deviation of 0.4$\mu$s comparing quite closely with the value of $\sim$ 16$\mu$s reported by Van Kessel *et. al.* [15].

### 4.2.3 Deflection Angles

Deflection angles of the micromirrors in their 'ON' and 'OFF' state reflect the condition of the underlying address electrodes. Depending on the prospective action of the mirror, the address voltage directly beneath the landed mirror will be set to either 0 or $5V$. For example, a mirror originally in the 'OFF' position that is preparing to 'stay' as the reset waveform is triggered will have the address electrode underlying the landed site fixed at $0V$. In contrast, if the mirror were ready to 'crossover', the same electrode would be held at $5V$. The specifics of this methodology were previously discussed in Chapter 2. To measure the effects of these voltages, angular measurements were performed directly before and after each transition. Table 4.3 presents the mean and standard deviation of the results collected over 160 mirrors. The starting angles for both the 'stay' and 'float' transitions as well as the landing angles for the 'crossover' transition match up very closely. This is expected since the potential between the mirror and the landed site is $24V$ in each case. Small differences in the landing angles of the 'crossover' transition are most likely caused by the small oscillations of the mirror settling in the new position. The starting angles of the 'crossover' transition are also visibly lower than the others, which can be understood as a clear consequence of the lower potential difference ($19V$) between the mirror and the electrode in this case.

| | Start Angle (°) | $\sigma$ | End Angle (°) | $\sigma$ |
|---|---|---|---|---|
| **'Crossover'** | | | | |
| 'ON'-'OFF' | 11.39 | 0.06 | -11.82 | 0.06 |
| 'OFF'-'ON' | -11.61 | 0.06 | 11.58 | 0.07 |
| **'Stay'** | | | | |
| 'ON'-'Stay' | 11.60 | 0.07 | 11.59 | 0.06 |
| 'OFF'-'Stay' | -11.79 | 0.06 | -11.77 | 0.06 |
| **'Float'** | | | | |
| 'ON'-'Float' | 11.58 | 0.07 | 0.54 | 0.05 |
| 'OFF'-'Float' | -11.77 | 0.06 | -0.53 | 0.04 |

Table 4.3: Mean resting angles of 160 mirrors in various transitional states.

Data sheets for the DMD™ declare the landing angles of the micromirrors to be $12 \pm 1°$. Therefore, while the measured angles seem low, they are all within the range predicted by TI. By examining the data presented in table 4.3, however, it would appear that the calibration has been linearly translated by $-0.1°$. Though making this translation would ruin the symmetry present in the floating angles (landing angles of 'float' transition). It is expected however, that due to the symmetry of the device, the landing angles on either corner should be symmetrical about the neutral (flat) position. Thus, the offset in the recorded resting angles is most likely do to a slight nonlinearity that was not completely removed by the calibration. The same error was shown to affect the determined quality factors of the mirrors.

# Chapter 5

# Simulation

Dynamic modeling of the DMD$^{TM}$ micromirrors was chosen to demonstrate the feasibility of analog operation. This type of device simulation is a commonly used tool in the field of MEMS to optimize designs and predict device behaviour. As well, it eliminates the risk of potential damage to the device due to the direct application of improper voltages. However, due to the complexity of the micromirrors which suffer (as do all electrostatic MEMS devices) from the nonlinear effects of electrostatic attraction (as well as other nonlinearities), an analytical solution such as the one presented in §2.5 (damped motion of a free harmonic oscillator) is not possible. Instead, a numerical solution is required. Several accurate models based on direct two and three-dimensional numerical simulation using fully meshed structures have been developed; although this solution is computationally expensive. Thus, one dimensional simulations based on the Runge-Kutta numerical method are typically chosen as a alternative. This method provides a solution that reduces computation cost without compromising the accuracy of the dynamic model. A detailed description of the 4th order Runge-Kutta numerical method is provided in Appendix B.

## 5.1 Modeling Equation

For many electrostatic actuators, the parallel plate model described in Chapter 2 is sufficiently accurate to describe the actuation of the device under consideration.

However, as the design of the actuator strays from that of the parallel plate capacitor it is important to understand how this model differs from the actual device and the consequences of this variance. The rotational motion of the micromirrors in the DMD™ array, for example, uses torsional actuation as opposed to the linear actuation experienced by a parallel plate capacitor. Thus, equation (2.12), which represents the motion of the parallel plate system, must be modified to incorporate torques and angular deflections ($\theta$) in substitution for the linear forces and displacements used previously. The governing equation for a torsional micromirror system can be derived using Newton's law for rotational motion and is thus given by

$$I\ddot{\theta} = M_e + M_m + M_d, \tag{5.1}$$

where the mass has been replaced by $I$, the polar mass moment of inertia, and a summation of torques, as opposed to linear forces, appears on the right hand side. $M_e$, $M_m$, and $M_d$ represent the driving electrostatic torque, the opposing mechanical torque and the damping torque respectively. This resulting equation for a torsional system appears similar to the parallel plate model thus making it possible, in many cases, to use effective constants as compensation for slight differences between the models. However, depending on the degree of angular deflection, the electrostatic torque can differ greatly from the electrostatic force experienced by a set of parallel plates. For example, analysis performed by Osterberg has demonstrated that pull-in predictions of torsional micromirrors based on the parallel plate model can exhibit errors of up to 20% compared to finite-element simulations [41]. As such, for large angular deflections, it is crucial to develop a valid representation of the electrostatic torque.

### 5.1.1 Electrostatic Torque

Degani *et al.* have invested a considerable amount of time studying the pull-in phenomenon of electrostatic actuators. In doing so, they have determined the electrostatic forces produced for a myriad of actuators of various geometries including the torsional microactuator [9]. A schematic diagram of the torsional actuator is

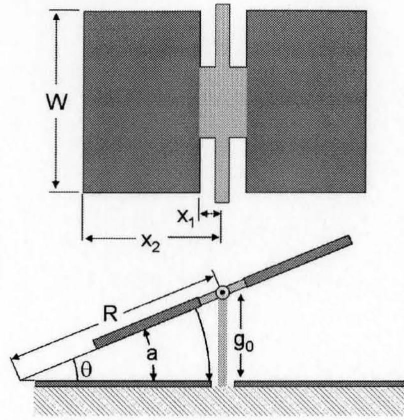


Figure 5.1: Schematic of a torsional actuator including required dimensions for the formulation of the electrostatic torque.

presented in figure 5.1 along with the required dimensions for analysis. Here, the top plate is free to rotate about the axis marked by $\odot$ while the bottom plate remains fixed. The angle of rotation is denoted by $\theta$ as previously referred to in equation (5.1). At rest, the separation distance between the plates is $g_0$. The cross sectional dimensions of the electrode on the upper plate are given by the distances $x_1$, and $x_2$ extending from the axis of rotation.

The electrostatic torque present in this system is determined by solving the Laplace equation for the electrostatic potential difference applied between the plates and integrating the electrostatic pressure over the mechanically free plate. Using cylindrical coordinates and assuming a voltage $V$ is placed on the upper plate while the bottom electrode remains connected to ground, the Laplace equation is given by [9]:

$$\frac{\partial^2 \Phi(\phi)}{\partial \phi^2} = 0, \text{ where } \Phi(\phi = 0) = 0 \text{ and } \Phi(\phi = \theta) = V. \tag{5.2}$$

The solution to the above equation yields

$$\Phi(\phi) = \frac{V}{\theta}\phi. \tag{5.3}$$

The electrostatic field can be determined by taking the gradient of the above potential.

Therefore,

$$\vec{E} = -\nabla\Phi = \begin{cases} 0 & \text{outside the plates} \\ -\frac{V}{\theta r}\hat{\phi} & \text{between the plates} \end{cases}, \tag{5.4}$$

where $\hat{\phi}$ is the unit vector in the direction of $\phi$. The charge density accumulated on the plates as a result of the applied potential is given by [9]

$$\rho_s = \epsilon_0(E_{\perp in} - E_{\perp out})|_{\phi=0 or \theta} = \mp\frac{\epsilon_0 V}{\theta r}, \tag{5.5}$$

where the + sign is for the upper plate and the − sign is for the lower plate. As discussed in Chapter 2, the charge is arranged such that any applied potential, regardless of polarity, will result in an attractive force between the electrodes. The electrostatic pressure on the upper plate is given by

$$\vec{P}(\theta) = \rho_s\vec{E}_{lower-plate} = -\frac{\epsilon_0 V^2}{2\theta^2 r^2}\hat{\phi}. \tag{5.6}$$

The resulting electrostatic torque can be found by integrating the contribution of the electrostatic pressure over the all elements of the upper electrode. Since the torque produced is about the hinges, let $r = R - x$ for convenience. Therefore,

$$M_e(\theta) = \frac{-\epsilon_0 V^2}{2}\int_{z=-W/2}^{W/2}\int_{x=x_1}^{x_2}\frac{x}{(R-x)^2\theta^2}dxdz \tag{5.7}$$

where $W$ is the width of the electrodes as shown in figure 5.1, and $R = \frac{g_0}{\sin(\theta)}$. Solving (5.7) produces a straight forward expression for the electrostatic torque of a torsional micromirror:

$$M_e(\theta) = \frac{-\epsilon_0 W V^2}{2\theta^2}\left[\ln\left(\frac{g_0 - x_2\sin(\theta)}{g_0 - x_1\sin(\theta)}\right) + \frac{g_0}{g_0 - x_2\sin(\theta)} - \frac{g_0}{g_0 - x_1\sin(\theta)}\right]. \tag{5.8}$$

### Fringing Fields

Throughout the formulations for the electrostatic force produced between a set of parallel plates (Chapter 2) and a set of torsional plates presented above, fringing fields have been ignored. Although this assumption is only completely accurate for a set of infinite parallel plates, the accuracy of this assumption is still very reasonable

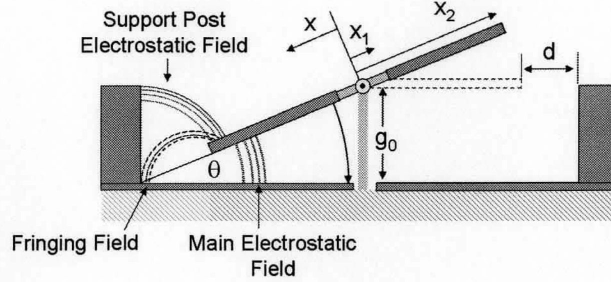


Figure 5.2: Counter electrostatic fields in the DMD™ design.

for parallel plates with a large ratio of plate size to separation distance. Tilting the plates, however, increases the fringing fields present in the design. The schematic presented in figure 5.2 displays the additional fields present in a DMD™ micromirror. A counter electrostatic field is produced by a combination of a fringing field supplied by the address electrode as well as an additional field produced by the support post a distance $d$ from the yoke. Torques provided by these fields rotate the mirror in the opposite direction to that of the main electrostatic field. The torque attributed to the fringing field is given by [42]

$$M_{eFF}(\theta) = \frac{-\epsilon_0 W V^2}{2(\pi - \theta)^2}\left[\ln\left(\frac{g_0 - x_2\sin(\theta)}{g_0 - x_1\sin(\theta)}\right) + \frac{g_0}{g_0 - x_2\sin(\theta)} - \frac{g_0}{g_0 - x_1\sin(\theta)}\right], \quad (5.9)$$

while the torque produced by the support post is defined as [42]

$$M_{eSP}(\theta) = \frac{-\epsilon_0 W V^2}{2(\frac{\pi}{2} - \theta)^2}\left[\ln\left(\frac{x_{SP} - x_2\sin(\theta)}{x_{SP} - x_{SP}\tan(\theta)\sin(\theta)}\right) + \frac{x_{SP}}{x_{SP} - x_2\sin(\theta)} - \frac{1}{1 - \tan(\theta)\sin(\theta)}\right], \quad (5.10)$$

where $x_{SP} = x_2 + d$.

Plotting these torques as a function of the angular deflection of the micromirror reveals that the resulting torque created by the fringing field is on the order of $10^2$ times smaller than the main electrostatic torque. In addition, the torque generated by the support post is $10^4$ times less than the main electrostatic field. Due to the low magnitude of these fields, they can be easily ignored without consequence to the accuracy of the model.

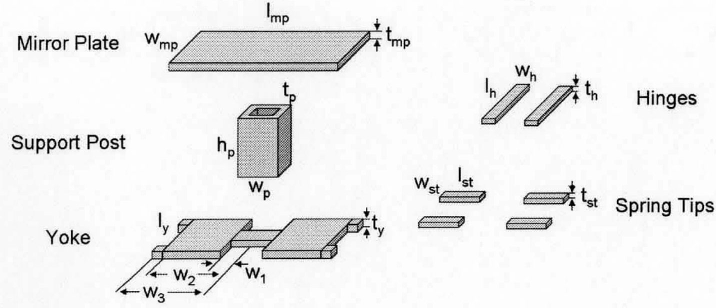


Figure 5.3: Components of the DMD$^{\text{TM}}$ micromirror including the important dimensions of each component.

### 5.1.2 Moment of Inertia

Just as the mass of an object opposes linear acceleration, the mass moment of inertia provides a measure of the body's resistance to angular acceleration. For a homogeneous object, the moment of inertia $I$ is given by

$$I = \rho \int r^2 dV, \tag{5.11}$$

where $\rho$ is the density of the object and $r$ is the normal distance from the axis of rotation to the elemental volume $dV$. The moment of inertia for a DMD$^{\text{TM}}$ micromirror was derived by combining the moments of the individual components depicted in figure 5.3. For each component, the moment was calculated about an imaginary axis passing through its center of mass. For the case of the mirror plate and the support post, the axes of rotation were then translated to the axis of rotation of the system (about the hinges) using the parallel axis theorem. This is given by

$$I = I_G + md^2, \tag{5.12}$$

where $I_G$ is the moment of the object about its center of mass and $d$ is the distance which separates the two axes. A detailed look at the calculations leading to these moments can be found in Appendix C.

### 5.1.3 Mechanical Torque

The micromirror structure of the DMD$^{\text{TM}}$ is held in place by two beams positioned on either side of the yoke. These beams function as the hinges of the structure allowing the mirror to rotate back and forth. As one edge of the mirror is attracted towards the substrate, a torque inflicted on the hinges causes the beams to twist. The strain induced by this deformation results in a restoring torque proportional to the rotation of the beams as they attempt to regain their equilibrium form. Timoshenko *et al.* have developed a formula to predict this constant of proportionality based on the dimensions of the beam [43]. The torsional spring constant for a clamped-clamped beam is given by

$$K_\theta = \frac{2Gwt^3}{l}\left[1 - \frac{192w}{\pi^5 t}\sum_{n=1}^{\infty}\frac{1}{(2n-1)^5}\tanh\frac{(2n-1)\pi t}{2w}\right] \tag{5.13}$$

where $G = 26\text{GPa}$ is the modulus of elasticity for Aluminum, $l$, $w$, and $t$ are the length, width, and thickness of the beam [44].

Real springs under large displacements can exhibit nonlinear behaviour due to strain-hardening or strain-softening. This phenomenon can be modeled by applying the nonlinear term $K_{NL}\theta^3$ to the mechanical torque. If $K_{NL} > 0$ then the spring is considered to be a weak spring and the restoring force will be smaller than that of the linear case. If $K_{NL} < 0$ the resulting force will be greater than that of the linear case and the spring is said to be strong.

As a micromirror in the DMD$^{\text{TM}}$ array approaches its maximum deflection, a second linear spring term is added to total mechanical torque as the spring tips hanging off the edge of the yoke touch down on the landing sites. Similar to the torsional hinges, the spring tips oppose bending with a force proportional to the deflection of the tips. The bending spring constant of a singly clamped beam is given by

$$K_b = \frac{Ewt^3}{4l^3} \tag{5.14}$$

where $E = 71\text{GPa}$ is Young's modulus for Aluminum. The total mechanical torque

of the micromirror system is the sum these components. Thus,

$$M_m = \begin{cases} K_\theta \theta + K_{NL}\theta^3 & \theta < |\theta_C| \\ K_\theta \theta + K_{NL}\theta^3 + K_b L_s^2 |\theta - \theta_C| & \theta > |\theta_C| \end{cases}, \tag{5.15}$$

where $\theta_C$ is the angle at which the spring tips contact with landing site, and $L_s$ is the length of the spring tip.

### 5.1.4 Damping

On the DMD™, only a narrow gap separates the moveable micromirrors from the fixed substrate. Therefore, as the mirror is rotated, air trapped between the mirror and the substrate is compressed resulting in a phenomenon known as squeeze film damping. The total damping force in this case is a combination of two effects: the air spring effect and the dissipative damping effect. The latter is a common form of air damping which is proportional to the velocity of the mirror and simply slows the rotation due to air friction. In contrast, the air spring effect is created by the spring-like behaviour of the compressed air which stores up energy as the mirror rotates and pushes the mirror back in the opposite direction. In a recent paper by Pan *et al.* an analytical expression for the squeeze film damping effect on a torsional micromirror was developed and compared with experimental results [45]. From this comparison, they concluded that the air spring effect was negligible in the case of a torsional actuator due to a much larger spring force exhibited by the torsional hinge. The following analytical formula was also presented by Pan *et al.* and is designed to predict the approximate damping torque in a torsional micromirror system :

$$M_d = \eta\dot{\theta}, \text{ where } \eta = -\frac{48}{\pi^6(b^2+4)}\frac{\mu l w^5}{g_0^3} \tag{5.16}$$

Here, $l$ and $w$ are the length and width of the mirror, $g_0$ is the separation distance at when the mirror is at rest, $b = l/w$, and $\mu = 1.79 \times 10^{-5}$Pa s is the viscosity of air at 1 atmosphere and room temperature.

Evaluating the damping in the case of the DMD™ micromirror structure is complicated by the stacked design. Both the mirror plate and the yoke layers of the

micromirror will contribute to air damping; thus, equation (5.16) must be evaluated for both layers and combined to determine the total damping of the system.

As well as supplying an elastic spring force to equation (5.15), the interaction of the spring tips with the landing electrode also produces a frictional damping term. The friction produced as the tips move across the landing pads is proportional to the force exerted by the spring tip itself. Therefore, the total damping torque of the system is given by

$$M_d = \begin{cases} \eta_{mirror}\dot{\theta} + \eta_{yoke}\dot{\theta} & \theta < \theta_C \\ \eta_{mirror}\dot{\theta} + \eta_{yoke}\dot{\theta} + \mu K_b L_s^2 |\theta - \theta_C| & \theta > |\theta_C| \end{cases}, \tag{5.17}$$

where $\eta_{mirror}$ and $\eta_{yoke}$ are the air damping coefficients for the mirror and yoke structures, $L_s$ is the length of the spring tip and $K_b$ is its bending spring constant.

### 5.1.5 DMD$^{TM}$ Dimensions

Approximate values for the constants revealed in the previous sections were required in order to begin modeling of the micromirror. Each of these parameters, including the moment of inertia $I$, the spring constants, the damping coefficients and even the electrostatic torque $M_e$ (as illustrated in equation (5.7) are dependant upon the dimensions of the micromirror. Measuring the DMD$^{TM}$ dimensions posses a problem however, since this costly approach would require completely dismantling the device. Thus, the DMD$^{TM}$ dimensions were accumulated from a series of published papers [46, 47, 48] and patents [49, 50, 33].

The moveable structure on each of the DMD$^{TM}$ micromirrors is comprised of several elements. Each of these components were presented in figure 5.3 along with an indication of the dimensions as they are reported in table 5.1.

The DMD$^{TM}$ has evolved considerably since its initial unveiling in the late eighties and it continues to be improved. Over the past five years, many slightly different designs have been manufactured. Given the multitude of designs, many of the DMD$^{TM}$ dimensions presented in table 5.1 have grave uncertainties and it is expected that, in many cases, the actual DMD$^{TM}$ dimensions are on the same order as the values given

| | Length($\mu$m) | $\delta l$ | Width($\mu$m) | $\delta w$ | Thickness($\mu$m) | $\delta t$ |
|---|---|---|---|---|---|---|
| Mirror Plate | 12.68 | - | 12.68 | - | 0.4 | 0.1 |
| Support Post | 2.0($h_p$) | 0.25 | 2.0 | 0.5 | 0.4 | 0.1 |
| Yoke | 8.3 | 0.5 | 1.5,4.39,5.0 | 0.5,0.5,1 | 0.3 | 0.1 |
| Hinges | 3.7 | 0.1 | 0.78 | 0.1 | 0.1 | 0.02 |
| Spring Tips | 1.0 | 0.2 | 0.55 | 0.2 | 0.1 | 0.02 |

Table 5.1: DMD™ micromirror dimensions.

here. Based on these dimensions, approximate values for the moment of inertia, the spring constants, and the damping coefficients were determined.

## 5.2 DMD™ Model

Relationships between the moment of inertia, the torsional spring constants and the damping coefficient can be determined using the known natural frequency and quality factor of the mirrors, which were determined through experimental measurements of the micromirror trajectories as presented in Chapter 4. These relationships for a damped mass-spring system are given by

$$\omega_0 = \sqrt{\frac{K}{I}}, \text{ and} \tag{5.18}$$

$$Q = \frac{I\omega_0}{\eta}. \tag{5.19}$$

Unfortunately, three unknowns and only two equations are presented here. Therefore, dynamic simulations were performed in MATLAB using a fourth-order Runge-Kutta numerical approximation to solve equation (5.1) for the motion of the micromirror given the application of predefined voltage waveform inputs discussed in Chapter 2. The approximate values for the moment of inertia, spring constants and damping coefficients determined in the previous section were used as starting values, but were modified to allow for the best fit of the model in reference to experimental data. Published simulations which were performed on a thoroughly verified TI-developed DMD™ pixel mechanics simulator for an earlier generation DMD™ micromirror [15]

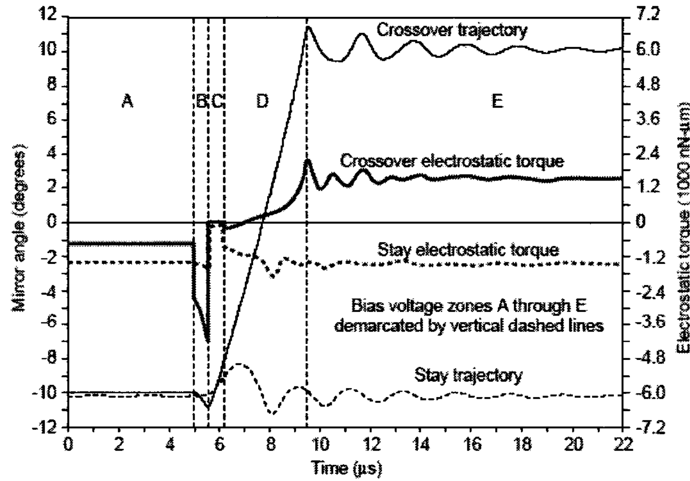


Figure 5.4: Simulations performed by TI providing an insight to the electrostatic torque present in the DMD$^{TM}$ micromirror as a function of angular deflection.

were also used to compare the electrostatic torque as a function of the mirror's angular position $\theta$. These simulations are presented in figure 5.4. Use of these functions provides increased information about the timing of the micromirror transitions. As well, the magnitude of the total electrostatic torque lends knowledge of the DMD$^{TM}$ dimensions which can greatly influence the surrounding electrostatic fields.

### 5.2.1 PSD Transfer Function

Unfortunately, a direct comparison between the simulated waveforms and the experimentally measured trajectories of the micromirrors was not possible due to the frequency response limitations of the PSD. The switching speed of the micromirror, or equivalently, the rise time of the beam traveling across the PSD was measured to be $\sim 3\mu s$. If the mirror was to oscillate back and forth at this speed, the frequency of the beam would be $166\mu s$ - much smaller than the measured cutoff frequency of the detector ($f_{3dB} =\sim 295$kHz). However, as is the case with any step function in time, a Fourier transform of the signal reveals many higher order frequency components. As an example, the Fourier transform of a measured 'crossover' transition is presented in

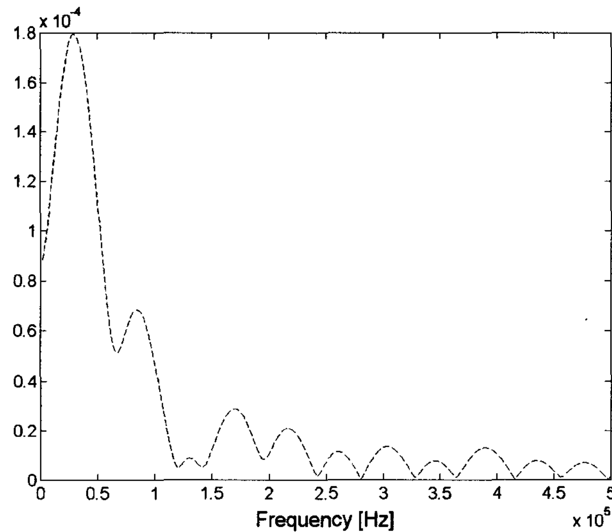


Figure 5.5: Fourier transform of the measured 'crossover' trajectory of a micromirror showing small yet present high frequency components.

figure 5.5. In this example, the higher frequency components have been reduced (or removed) by the PSD, thus, making visible a rounding of the measured 'crossover' trajectory. This was seen in data presented in Chapter 4 (fig. 4.3(b)). Thus, in order to accurately simulate the motion of the micromirror based on a comparison with collected data from the PSD, the simulations were passed through the transfer function of the PSD presented in Chapter 3 (fig. 3.13). This was accomplished by taking the Fourier transform of the simulated trajectory, multiplying the Fourier components by the transfer function and returning the simulation to the time domain through an inverse Fourier transform. To reduce the effects of 'windowing' caused by the application of the Fourier transform, simulations were produced over many points extending out much before and after the actual mirror transition.

### 5.2.2 Results

A tedious trial and error procedure involving the modification of the micromirror parameters followed by a comparison of the simulated trajectories with experimental

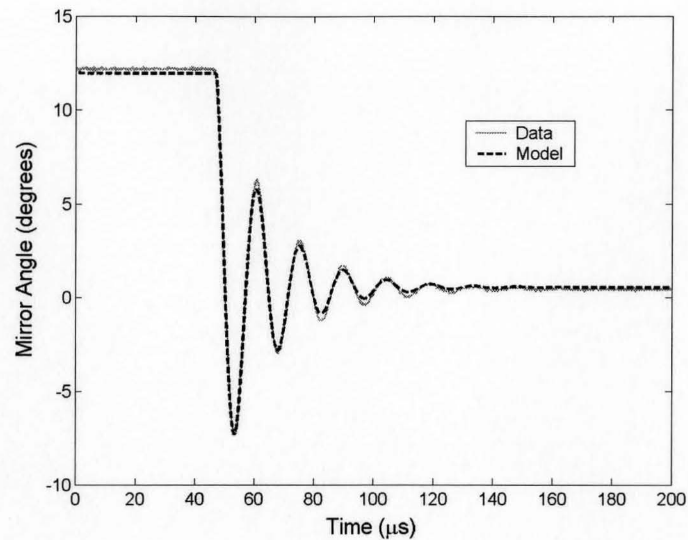


(a)

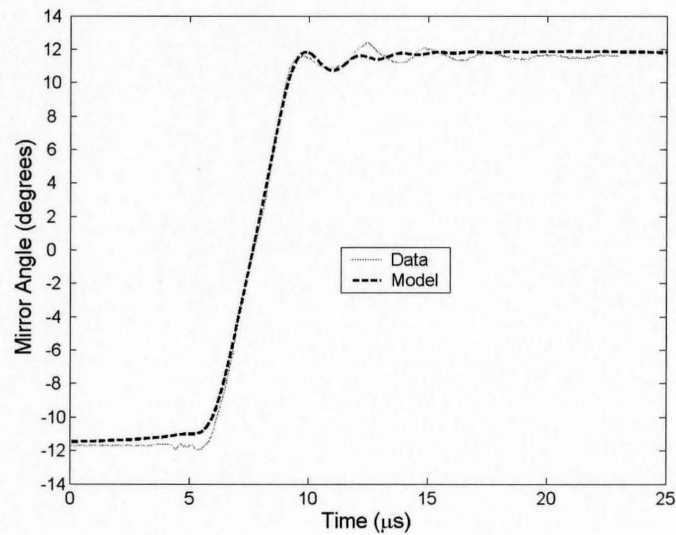


(b)

Figure 5.6: Comparison of simulated trajectories with experimental data for a) the 'float' transition and b) the 'crossover' transition.

data resulted in the best fit model presented in figure 5.6. Figure 5.6(a) displays the results of the 'float' transition in which all but the $5V$ address voltage have been removed. Despite some slight discrepancies in the peaks of the oscillating function, the two curves match very closely. The model comes to rest at $\sim 0.55°$ compared to the mean 'floating angle' of $\sim 0.54 \pm 0.05°$ presented in Chapter 4.

As discussed in the previous section, the 'crossover' simulations were passed through the transfer function of the PSD in order to accurately compare the model with the measured trajectories of the micromirrors. This comparison is provided in figure 5.6(b). The difference in the initial section of the curves is caused by the application of the Fourier transform followed by the inverse Fourier transform of the signal. The transition as well as the first transient peak of the model closely follows the trajectory of the micromirror but fails to model the rest of the transient motion. Several reasons exist for this discrepancy. First, damping due to friction between the spring tips and the landing site is largely exaggerated by the model. For this reason, the model's transient motion abruptly dies out. However, lowering the frictional force allows the amplitude of the transient oscillations to far exceed those seen in reality. The solution most likely involves an alternative form of dissipation which has not yet been considered. Inconsistencies also exist for the frequencies of the transient motion. The explanation for this may be due to a complex electrostatic torque for large angular displacements of the micromirror. This is demonstrated in section **E** of figure 5.4. A typical electrostatic torque increases for increasing angular deflection of the mirror, however, in the simulation presented in figure 5.4, the electrostatic torque is found to increase at points of decreasing angular deflection. Fringing fields were proposed to have created this phenomenon, however, as seen in §5.1.1 the counter electrostatic fields are too small at the present angles to cause such an effect. Nevertheless, discrepancies in this section of the transition are less crucial to the model since analog operation of the device does not depend on the interaction between the mirror and the landing site.

Improved simulations, which much more closely resemble the recorded 'crossover' trajectories, were achieved by means of a two stage model. In this attempt, the initial stage was used to simulate switching of the micromirror from one state to the other

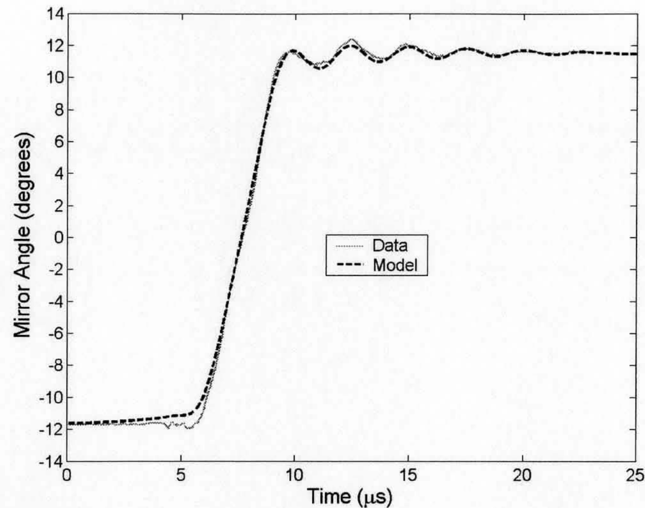


Figure 5.7: Simulated 'crossover' transition using two stage model.

while parameters in the second stage of the model were adjusted to fit the transient motion of the micromirror upon landing. It was also assumed that the spring tips remained in contact with the substrate in the second stage of the model creating a constant two spring system. This differs from the previous model in which the mirror was able to bounce back as a result of the restoring force of the spring tips. As demonstrated in figure 5.7, a much closer fit between the modeled simulations and the recorded trajectories was produced by this method; however, questions still remain concerning the discontinuities of the modeling parameters which exist at the interface between the two stages of the model.

Using the single and double stage models, two sets of determined values for the DMD$^{\text{TM}}$ micromirror including the moment of inertia, the spring constants and the damping coefficients are presented in table 5.2. These values are compared to the calculated geometrical results based on the dimensional dependant equations presented in the earlier sections of this chapter. The values obtained for the initial stage of the model are reasonably close to the geometrical values, however, these are still dependent on the dimensions of the device. Specifically, the torsional spring con-

| | Geometrical | Stage I | Stage II |
|---|---|---|---|
| **'Single Stage Model'** | | | |
| Moment of Inertia $(I)[kg \cdot m^2]$ | $3.8 \times 10^{-24}$ | $3.1 \times 10^{-24}$ | - |
| Torsional Spring Constant $(K_\theta)$ $[N \cdot m]$ | $4.4 \times 10^{-12}$ | $5.6 \times 10^{-13}$ | - |
| Bending Spring Constant $(K_b)[N/m]$ | 59 | 73 | - |
| Damping Coefficient $(\eta)$ $[N \cdot m \cdot s]$ | $1.4 \times 10^{-19}$ | $3.4 \times 10^{-19}$ | - |
| **'Double Stage Model'** | | | |
| Moment of Inertia $(I)[kg \cdot m^2]$ | $3.8 \times 10^{-24}$ | $3.1 \times 10^{-24}$ | $1.6 \times 10^{-23}$ |
| Torsional Spring Constant $(K_\theta)$ $[N \cdot m]$ | $4.4 \times 10^{-12}$ | $5.6 \times 10^{-13}$ | $2.9 \times 10^{-12}$ |
| Bending Spring Constant $(K_b)[N/m]$ | 59 | 73 | 199 |
| Damping Coefficient $(\eta)$ $[N \cdot m \cdot s]$ | $1.4 \times 10^{-19}$ | $3.4 \times 10^{-19}$ | $3.4 \times 10^{-19}$ |

Table 5.2: Comparison of DMD$^{\text{TM}}$ micromirror properties predicted by the single and double stage models to those predicted through geometrical formulas based on the micromirror dimensions.

stant is proportional to the cube of the hinge thickness. This results in large errors in the torsional spring constant for small discrepancies in hinge thickness. As well, the dimensions of the yoke greatly affect the magnitude of the electrostatic torque. An increase (or decrease) in the electrostatic torque requires a similar change in the mechanical torque supplied by the torsional hinges in order to maintain similar micromirror trajectories. Thus, due to the approximate nature of the yoke dimensions presented in table 5.1, the values presented here must also be considered approximate.

## 5.3 Analog Operation

Analog positioning of an electrostatically actuated spring-mass system can be achieved by varying the applied potential as described in Chapter 2. Therefore, using the model developed in this chapter to predict the motion of the DMD$^{\text{TM}}$ micromirror for an applied voltage, it is possible to simulate the feasibility of analog operation of the DMD$^{\text{TM}}$. As mentioned in Chapter 1, the difficulty in obtaining analog control of the DMD$^{\text{TM}}$ stems from the SRAM addressing electronics used to digitally control the state of the micromirrors. As a result of this circuitry, voltages applied to the

address electrodes beneath the opposing corners of the micromirror are limited to 0 or 5V. Even still, two possibilities exist for analog operation of the DMD$^{TM}$.

### 5.3.1 Bias Control

The bias voltage which is applied to the micromirror as well as its support structure is able to accept analog voltages from a set of pins located on the back of the DMD$^{TM}$. Unfortunately, only 16 bias/reset bus lines connect to the DMD$^{TM}$. This means that each applied bias voltage controls 48 rows of micromirrors in the array, totaling more than 49,000 individual mirrors. This, as a result, reduces the number of actuators in the array from greater than 768000 down to just 16. However, analog operation of these sections can be simply achieved by varying the magnitude of the applied bias voltage. A simulated example of analog positioning of a micromirror in the DMD$^{TM}$ array via bias voltage adjustments is presented in figure 5.8. Since the address electrodes are fixed at 0 and 5V, a bias voltage of 2.5V equalizes the torque in either direction allowing the mirror to maintain a flat position. Applying negative voltages to $V_b$, or alternatively, switching the state of the address electrodes will allow the mirror to rotate in the opposite direction.

### 5.3.2 Address Voltages

A slightly more complex solution - which maintains the individuality of the micromirrors - is achievable using of the address electrodes. By modulating the voltages between 0 and 5V for carefully allotted periods of time, an effective DC voltage is created. This phenomenon is easily explained using the modulated voltage waveform presented in figure 5.9. The Fourier series representation of this signal given by

$$V(t) = V_{DC} + \frac{4}{\pi} \sum_{n=1,3,5...}^{\infty} \frac{1}{n} \sin \frac{2\pi nt}{T}, \text{ where} V_{DC} = \frac{1}{T} \int_0^T V(t)dt, \tag{5.20}$$

decomposes the waveform into a series of harmonics. A DC component is also present provided the signal is varied non-symmetrically about 0V. Taking from figure 5.9, that

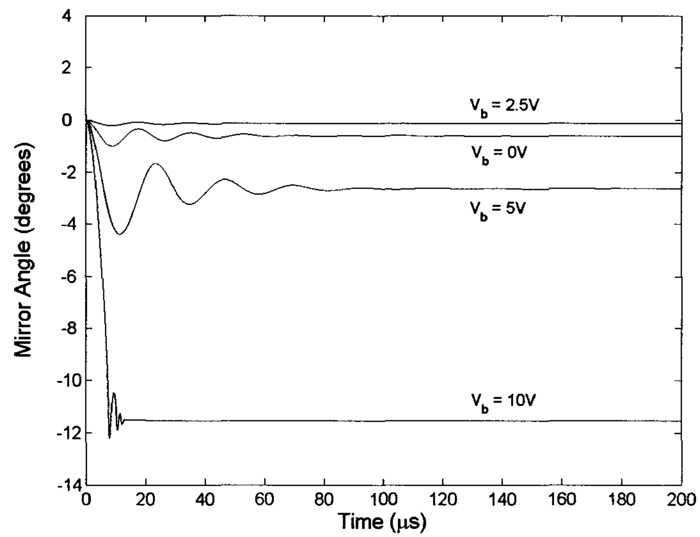


Figure 5.8: Simulation of analog operation by varying the amplitude of the bias voltage.

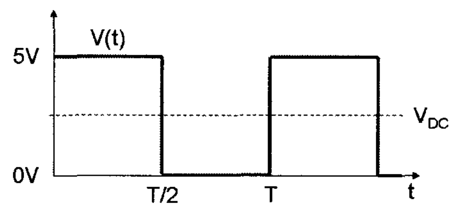


Figure 5.9: Square wave voltage.

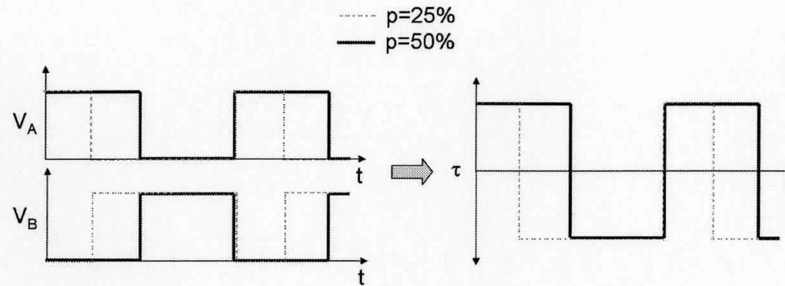


Figure 5.10: Schematic representing the voltages on the address electrodes equated to torques on the micromirror

$V(t) = 0$ from $t = \frac{T}{2}$ to $t = T$, evaluation of the DC component reduces to

$$V_{DC} = \frac{1}{T}\int_0^{pT} V(t)dt, \tag{5.21}$$

where $p = 50\%$ is the duty cycle of the square wave - meaning the voltage is set to 5V for 50% of the cycle and 0V for the rest. Therefore, it is evident that by adjusting the value of the duty cycle, the DC voltage component of the waveform is also modified. For example, $V_{DC} = 2.5$V for a duty cycle of 50%, but as this value is increased towards 100%, $V_{DC}$ rises to 5V. As well, for a duty cycle of 0%, the DC voltage drops to zero.

The DMD$^{\text{TM}}$ is complicated slightly by the addition of a second electrode; fortunately, this design is beneficial to the above described method of analog operation. The reason being, an applied bias voltage can be used to increase the maximum DC voltage of the system while maintaining the same zero minimum due to the symmetry of the device. Since the electrodes are complementary, one must be held at 0V while the other is set to 5V. Thus, the two applied waveforms will be 180° out of phase as demonstrated in figure 5.10. As opposed to the simple single electrode example, potentials acting between the electrodes and the mirror will pull the structure in opposite directions, thus, leading to the time dependant torque displayed in figure 5.10. Motion of the mirror depends on the duty cycle of the time dependant torque, or alternatively, the potential difference presented by the DC signals created by the

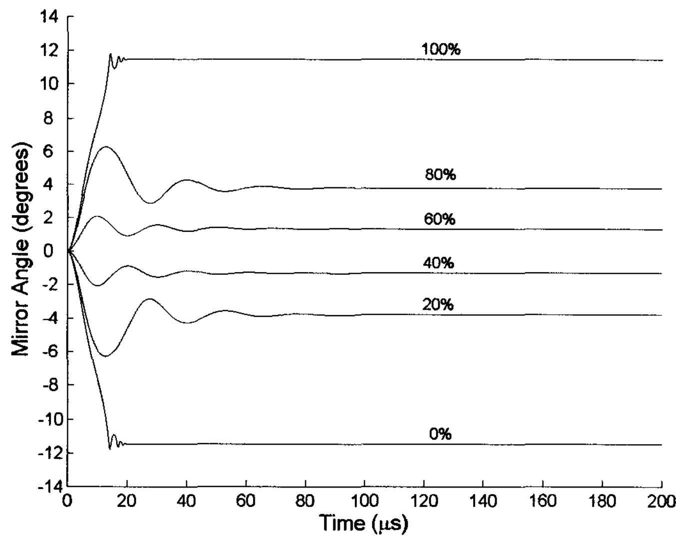


Figure 5.11: Simulation of analog operation based on the modulation of the address states.

modulation of $V_A$ and $V_B$. Thus, for a duty cycle of 50%, the mirror is pulled for an equal amount of time in either direction resulting in zero displacement; however, for a duty cycle of 25% (represented by the dotted line in fig. 5.10) the time dependant torque is not equally distributed amongst the electrodes causing the mirror to rotate towards electrode **B**.

Using the model of the DMD$^{\text{TM}}$ developed in this chapter, simulations were performed whereby modulated waveforms were applied to the address electrodes under each micromirror. A bias voltage of $V_b = 7.5V$ was also applied to increase the maximum deflection in either direction. Analog positioning of the micromirror is clearly visible in the simulations presented in figure 5.11 for varying duty cycles from $0 - 100\%$. The duty cycle values given in figure 5.11 refer to the modulation of $V_A$. At duty cycles of 0% and 100%, the potential difference in one direction or the other is too great and the mirror becomes unstable. This snap down phenomenon was discussed in Chapter 2.

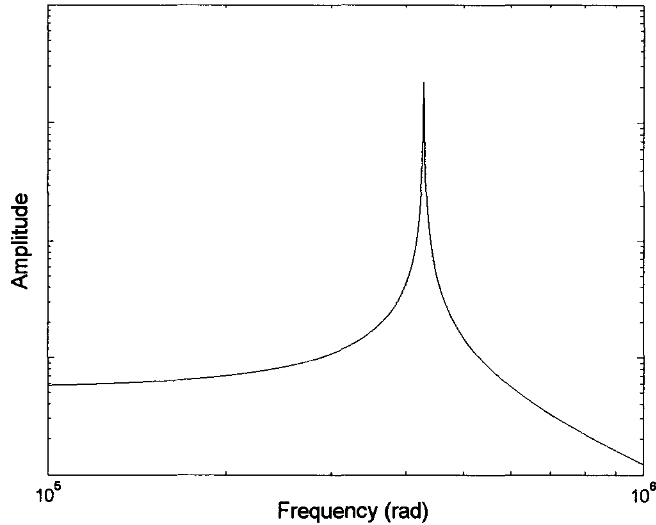


Figure 5.12: Theoretical frequency response of the DMD™ micromirror.

### 5.3.3 Angle Stabilization

In the previous section, analog positioning of the micromirror was achieved by modulating the underlying address circuitry; however, little was mentioned about the stability of the equilibrium angles. It is obvious that using a modulated input will most likely result in a modulated output though the systems response will depend on the frequency of the signal. The frequency response of a damped mass-spring system given an applied force $F = A\cos(\omega t)$ is given by

$$x(\omega) = \frac{A}{\sqrt{(\omega_0^2 - \omega^2)^2 + \omega^2\gamma^2}}. \tag{5.22}$$

A plot of this response shown in figure 5.12 illustrates that the amplitude of the oscillations is minimized for driving signals as far away from the natural frequency as possible. Thus, square wave signals of 5MHz were used in the previous section to produce the results shown in figure 5.11. As this frequency is minimized, the system gains more time to react to the changing voltage making oscillations more predominant for frequencies nearing the natural frequency of the system. Stabilization

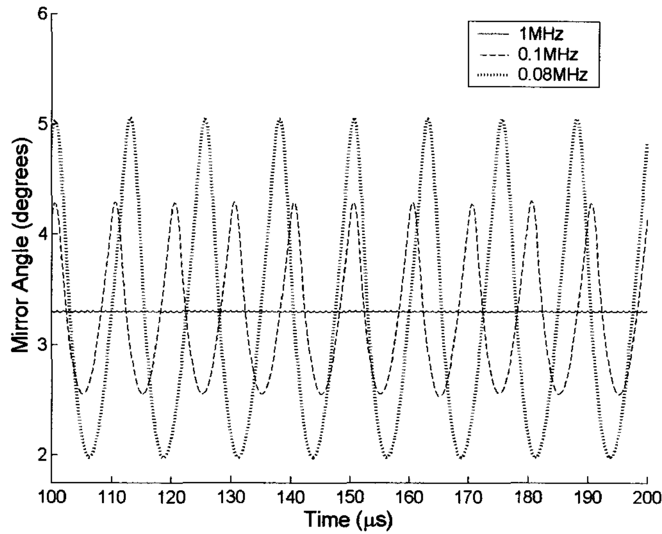


Figure 5.13: Stabilization of the angular deflection as a function of the input voltage frequency.

results for a duty cycle of 75% and range of input signal frequencies are displayed in figure 5.13. It is clear that higher input frequencies result in greater stabilization around the equilibrium angle.

### 5.3.4 Pull-In

Figures 5.8 and 5.11 presented earlier in this chapter, illustrate the problem inherent in electrostatically actuated devices. The device is only able to operate within approximately one third of the total separation gap on either side before becoming unstable. Degani *et al.* have performed numerous studies on a multitude of geometries to analytically predict the point where this instability occurs. For a torsional actuator, such as the rotating mirror in the DMD$^{\text{TM}}$ array, the pull-in voltage is given by [9]

$$V_{PI} = \sqrt{\frac{2Kg_0^3}{\epsilon_0 x^3 W} f(\beta, \gamma)} \tag{5.23}$$

where

$$f(\beta,\gamma)=\frac{\Theta_{PI}^{3}}{[\frac{1}{1-\beta\Theta_{PI}}-\frac{1}{1-\gamma\Theta_{PI}}+\ln\frac{1-\beta\Theta_{PI}}{1-\gamma\Theta_{PI}}]}. \tag{5.24}$$

Here, two dimensional ratios have been introduced: $\beta = x2/x3$ and $\gamma = x1/x3$. The pull-in angle, $\Theta_{PI}$, is determined independently of $V_{PI}$ by solving

$$\sum_{n=0}^{N}(1-n)\frac{n+1}{n+2}(\beta^{(n+2)}-\gamma^{n+2})\Theta_{PI}^{n}=0. \tag{5.25}$$

Using these equations, as well as the determined DMD$^{TM}$ dimensions and spring constant, the pull-in voltage of the DMD$^{TM}$ micromirrors was determined to be 11.4V. The instability of the system was shown to occur at an angle of $\Theta_{PI} = 5.8°$. This limits the wavefront stroke of the DMD$^{TM}$ to $\pm1.8\mu$m - slightly less than half the achievable range. Fortunately, methods exist to extend the range of an electrostatic actuator though this is not a simple procedure [51].

# Chapter 6

# Conclusions and Future Work

This thesis has demonstrated the feasibility of analog operation of a device which was previously overlooked by a multitude of applications due to its bistable nature. In the process, several device characteristics including the natural frequency and the quality factor of the Digital Micromirror Device$^{TM}$ were determined by way of an optical setup designed to actively monitor the dynamic motion of the individual mirrors in the micromirror array. Through automation, an investigation into the uniformity of the mirrors across the device was performed and properties such as the natural frequency were shown to vary according to radial dependencies introduced during the fabrication process. Though a slight error in the calibration of the optical setup resulted in the appearance of a geometrical device asymmetry, a strong consistency in the angular trajectories including switching times and the landing angles of the individual mirrors was reported.

Using the DMD$^{TM}$ characteristics discovered through experimentation, a computationally inexpensive, one-dimensional model based on the Runge-Kutta numerical approximation was constructed to simulate the response of the micromirrors to input voltage waveforms. Through this model, two methods which were proposed to provide analog operation of the DMD$^{TM}$ were verified. The first, which simply made use of the 16 bias voltage lines to directly influence the mirrors was limited in that it was only able to provide 16 controllable actuators. The second method, however, functioned using the underlying address circuitry typically used to provide digital op-

eration. By modulating the state of the address electrodes, a DC voltage of varying amplitude based on the duty cycle of the signal was achieved. Thus, by varying the duty cycle of the input waveform, the micromirror can be rotated to a desired angle in the same way a typical electrostatic device is controlled by adjusting the amplitude of the input voltage.

## 6.1 Limitations

The results in this thesis are hindered by two factors: namely, alignment and calibration issues. A third, and possibly fourth, degree of freedom are required to improve the positional alignment of the objective thereby eliminating the astigmatism in the propagated beam. The astigmatism present in the current optical setup separates the axial focal positions of the beam causing it to strike more than one micromirror at the position of 'best focus'. Although 60% of the incident light was shown to reflect off of the desired micromirror, measurements of mirror trajectories are constructed of a weighted average involving eight additional micromirrors directly adjacent to the mirror under consideration. By eliminating the astigmatism through improved alignment of the objective, this problem would be avoided.

Calibration of the PSD is necessary to compensate for the nonlinearities introduced by the orientation of the DMD$^{\text{TM}}$, the slight spherical aberration of the aspheric lenses and the characteristics of the PSD itself. Unfortunately, the method of calibration (replacing the DMD$^{\text{TM}}$ with a rotating macromirror) is also extremely sensitive to positional alignment. Placing the macromirror in the exact position of the DMD$^{\text{TM}}$ micromirror is a difficult requirement to fulfill in order to establish a perfect calibration. The difficulty arises due to the many degrees of freedom allowed by the macromirror apparatus on which the mirror as well as the entire apparatus can be translated separately. This degree of freedom was added in order to position the mirror on the axis of rotation of the rotational translation stage. Any separation between the mirror and the rotating axis leads to a possibly misleading change in the arc traced by the reflected beam. Thus, to ease the calibration, a perpendicular beam as well as theoretical measurements should be used to fix the mirror at the

exact position of the rotational axis thereby reducing the degrees of freedom during calibration.

## 6.2 Future work

The feasibility of the DMD$^{TM}$ working in an analog positioning scheme has been theoretically proven; however, before the device is ready for applications such as adaptive optics more still must be accomplished. First and foremost, the device must be removed from the current circuitry which limits the device to digital operation and placed in a system designed to allow high frequency inputs. This is not as easy as it appears. The DMD$^{TM}$ accepts inputs in a controlled manner which allows the device to be packaged in a small chip containing only 168 pins - not 768432 which would be required to access each mirror at any particular instance. Once the DMD$^{TM}$ has been connected to circuitry sophisticated enough to allow rapid switching of address states, experimental positioning of the micromirror can be monitored on the optical setup presented in this thesis.

With analog operation of the DMD$^{TM}$ experimentally proven, the device can be introduced into specific applications. As discussed in the onset of this thesis, adaptive optics, especially in the area of vision science, is one such application which could greatly benefit from this device. The DMD$^{TM}$, as well as all other current deformable micromirror arrays, still suffers from inadequate stroke to provide complete correction for vision science. This is also aggravated by the snapdown phenomenon which would need to be overcome to provide maximum stroke of the device. However, micromirror arrays with similar or less stroke have demonstrated reasonable correction of low order aberrations. Thus, by introducing the DMD$^{TM}$ into a setup such as the ones developed by Liang *et al.* [27] and Doble *et al.* [21] to test the correctional ability of the DMD$^{TM}$ for intentionally added aberrations, the ability of the DMD$^{TM}$ to excel as a wavefront corrector in the area of adaptive optics can be investigated.

# Appendix A

# Beam Trajectory

A beam of normal incidence which reflects off of a rotational plane will move vertically in a linear trajectory across the detection plane as the mirror surface is rotated. However, for a beam of non-normal incidence, the trajectory of the detected beam becomes an arc. A schematic representing an incident beam of angle $\theta$ is depicted in figure A.1. The trajectory of the reflected beam can be determined by finding the intersection of the reflected beam with the detection plane as a function of the mirrors rotation $\varphi$.

Assuming the detection plane is aligned perpendicular to the reflected beam, the normal $N$ is given by $P_2$. Therefore, the equation for the detection plane is given by

$$\begin{aligned} N \cdot (P_p - P_3) &= 0 \\ (d\sin\theta, 0, d\cos\theta) \cdot (x, y, z - \frac{d}{\cos\theta}) &= 0 \\ d\sin\theta \cdot x + d\cos\theta \cdot z - d^2 &= 0, \end{aligned} \tag{A.1}$$

where $P_p = (x, y, z)$ is any point on the detection plane. The equation for the reflected beam is given by

$$\begin{aligned} P_l &= P_1 + u(P_2 - P_1) \\ &= (0,0,0) + (d\sin\theta, 0, d\cos\theta) \\ &= u(d\sin\theta, 0, d\cos\theta), \end{aligned} \tag{A.2}$$

where the length of the line depends on the scalar $u$ and $P_l$ is any point along the

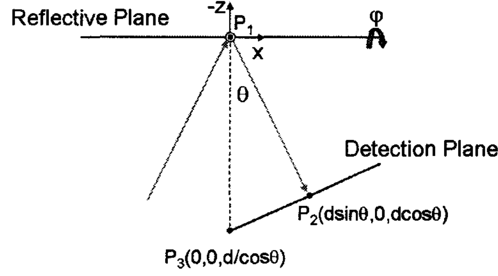


Figure A.1: Schematic of a non-normal incident beam reflecting of a rotating plane before striking the detection plane.

line. In order to introduce the effects of the mirror's rotation, the equation for the reflected beam must be multiplied by the following X-axis rotational matrix:

$$R_x = \begin{bmatrix} 1 & 0 & 0 \\ 0 & \cos\alpha & \sin\alpha \\ 0 & -\sin\alpha & \cos\alpha \end{bmatrix}. \tag{A.3}$$

Thus, the equation for the reflected beam after a rotation of the mirror becomes

$$P_l = u(d\sin\theta, -d\cos\theta\sin\varphi, d\cos\theta\cos\varphi). \tag{A.4}$$

Forcing $P_l = P_p$ and substituting equation (A.4) into (A.1) provides the point of intersection between the reflected beam and the detection plane. Thus,

$$u \cdot d^2\sin^2\theta + u \cdot d^2\cos^2\theta\cos\varphi - d^2 = 0. \tag{A.5}$$

Solving for $u$ gives

$$u = (\sin^2\theta + \cos^2\theta\cos\varphi)^{-1} \tag{A.6}$$

Therefore, the point at which the reflected beam strikes the detection plane for an angle of incidence $\theta$ and an angle of rotation $\varphi$ is given by

$$P = (\sin^2\theta + \cos^2\theta\cos\varphi)^{-1}(d\sin\theta, -d\cos\theta\sin\varphi, d\cos\theta\cos\varphi). \tag{A.7}$$

Plotting the solution to the reflected beam trajectory offered by equation (A.7) is difficult due to the three dimensional aspect of the solution. A rotation about the

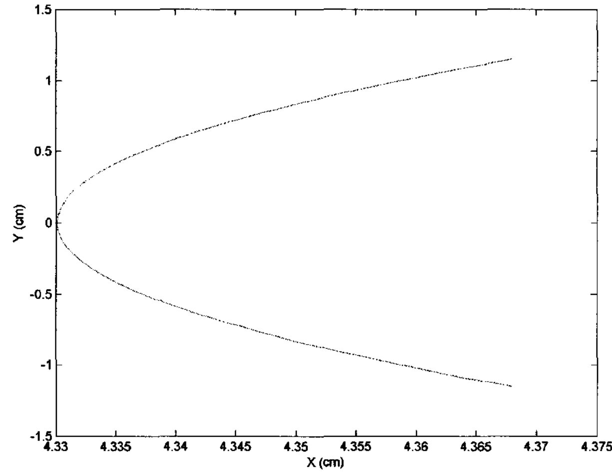


Figure A.2: Arc trajectory of a beam reflecting off of a rotational mirror at non-normal incidence

X-axis given by

$$R_y = \begin{bmatrix} \cos\varphi & 0 & -\sin\varphi \\ 0 & 1 & 0 \\ \sin\varphi & 0 & \cos\varphi \end{bmatrix}, \tag{A.8}$$

where $\alpha = -\theta$, simplifies the graphical representation of this problem. Hence, the rotation of the solution projects the trajectory of the reflected beam onto the $z = d$ plane and the solution becomes

$$P = (\frac{d\sin\theta\cos\theta - d\cos\theta\cos\varphi\sin\theta}{\sin^2\theta + \cos^2\theta\cos\varphi}, \frac{-d\cos\theta\sin\varphi}{\sin^2\theta + \cos^2\theta\cos\varphi}, d), \tag{A.9}$$

which can be easily plotted in two dimensions. An example of the arc trajectory traced by the reflected beam is given in figure A.2 for $\theta = 30°$ and $d = 5$cm.

# Appendix B

# Runge-Kutta Numerical Method

Using the Taylor series expansion it is possible to predict the value of a function at a given point based on a set of initial values. For example, the value of the one-dimensional function $f(x)$ for any $x$ is given by

$$f(x) = f(a)+f^{(1)}(a)(x-a)+\frac{f^{(2)}(a)}{2!}(x-a)^2+\frac{f^{(3)}(a)}{3!}(x-a)^3+...+\frac{f^{(n)}(a)}{n!}(x-a)^n+... \tag{B.1}$$

where $f^{(n)}(a)$ is the $n^{\text{th}}$ derivative of $f(x)$ evaluated at an arbitrary point $x = a$. The exact solution to this equation unfortunately requires the knowledge or determination of an infinite number of derivatives; therefore, an approximate solution can be found by truncating the right hand side of equation (B.1) down to an appropriate number of terms. The error in the resulting solution is on the order of the first truncated term.

Given a first order ordinary differential equation

$$\frac{dy}{dx} = f(x, y) \tag{B.2}$$

and a set of initial values $x_n$, $y_n$, and $f_n$, it is possible to advance the solution of equation (B.2) using a truncated form of the Taylor series expansion

$$y_{n+1} = y_n + hf(x_n, y_n) + O(h^2). \tag{B.3}$$

In this case, $h = x_{n+1} - x_n$ represents the interval separating the initial and evaluated points. This process can be continued using the new point to find the next and

so on until a solution for equation (B.2) is determined over the desired interval. Unfortunately, this method is not particularly accurate due to the number of ignored terms in equation (B.1). Including higher order terms, however, does not present a valid option since this would require the formulation of higher order derivatives. The fourth-order Runge-Kutta method defined by the following equations

$$\begin{aligned}
k_1 &= hf(x_n, y_n) \\
k_2 &= hf(x_n + \frac{h}{2}, y_n + \frac{k_1}{2}) \\
k_3 &= hf(x_n + \frac{h}{2}, y_n + \frac{k_2}{2}) \\
k_4 &= hf(x_n + h, y_n + k_3) \\
y_{n+1} &= y_n + \frac{h}{6}(k_1 + 2k_2 + 2k_3 + k_4) + O(h^5),
\end{aligned} \tag{B.4}$$

instead, evaluates the first order derivative four times within the interval at each progressive step. A weighted average of the determined slopes is then performed to predict a more accurate solution.

The system equation for a torsional micromirror was developed in Chapter 5. In its simplest form the governing equation can be written as

$$I\ddot{\theta} + \eta\dot{\theta} + K_\theta\theta = M_e. \tag{B.5}$$

This is of course a second-order differential equation, but it is possible to reduce this to a set of first-order differential equations:

$$\begin{aligned}
\frac{d\theta(t)}{dt} &= \omega(t) = f_1(t_n, \theta_n, \omega_n) \\
\frac{d\omega(t)}{dt} &= \frac{1}{I}(M_e - \eta\omega(t) - K_\theta\theta(t)) = f_2(t_n, \theta_n, \omega_n).
\end{aligned} \tag{B.6}$$

$\omega(t)$ in this equation is the angular velocity of the mirror. The Runge-Kutta approximation for this system is calculated as follows

$$\begin{aligned}
\alpha_1 &= hf_1(t_n, \theta_n, \omega_n) \\
\beta_1 &= hf_2(t_n, \theta_n, \omega_n) \\
\alpha_2 &= hf_1(t_n + \frac{h}{2}, \theta_n + \frac{\alpha_1}{2}, \omega_n + \frac{\beta_1}{2})
\end{aligned}$$

$$\beta_2 = hf_2(t_n + \frac{h}{2}, \theta_n + \frac{\alpha_1}{2}, \omega_n + \frac{\beta_1}{2})$$

$$\vdots \tag{B.7}$$

$$\theta_{n+1} = \theta_n + \frac{h}{6}(\alpha_1 + 2\alpha_2 + 2\alpha_3 + \alpha_4) + O(h^5) \tag{B.8}$$

$$\omega_{n+1} = \omega_n + \frac{h}{6}(\beta_1 + 2\beta_2 + 2\beta_3 + \beta_4) + O(h^5), \tag{B.9}$$

where $\alpha_3$, $\alpha_4$, $\beta_3$, and $\beta_4$ have been omitted due to the similarities with equation (B.4).

# Appendix C

# Moment of Inertia

Calculating the moment of inertia for a complex object can (in most cases) be simplified by reducing the object to its basic components, calculating the individual moments and combining the results by means of the parallel axis theorem. In the case of the DMD$^{\text{TM}}$, an individual micromirror can be reduced to four separate components: the mirror plate, support post, yoke and a set of torsional hinges. The moment of inertia for each of these components can be geometrically determined by means of equation (5.11) which is repeated here for convenience:

$$I = \rho \int r^2 dV. \tag{C.1}$$

Using the density of Aluminum, $\rho = 2700\text{g/m}^3$, the moment of inertia for each component of the DMD$^{\text{TM}}$ micromirror is determined in the following sections. In the final section, the moments of the individual components are combined to define the total moment of inertia for DMD$^{\text{TM}}$ micromirror structure.

### Mirror Plate

The dimensions of the mirror plate are depicted in figure C.1 along with the axis of rotation which passes diagonally through the plate. Using equation (C.1), the integral can be divided into two parts,

$$I_{mp} = \rho \int_{-\alpha}^{0} \int_{-(x+\alpha)}^{(x+\alpha)} \int_{-\frac{t}{2}}^{\frac{t}{2}} (x^2 + z^2) dxdydz + \rho \int_{0}^{\alpha} \int_{(x-\alpha)}^{-(x-\alpha)} \int_{-\frac{t}{2}}^{\frac{t}{2}} (x^2 + z^2) dxdydz], \tag{C.2}$$

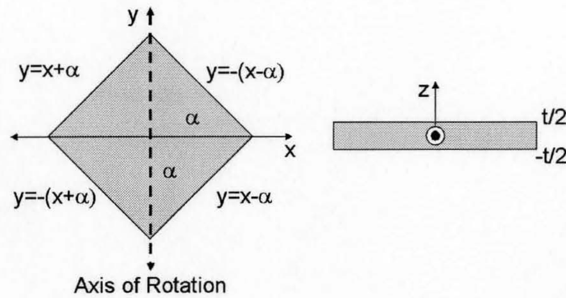


Figure C.1: Dimensions of mirror plate showing axis and rotation.

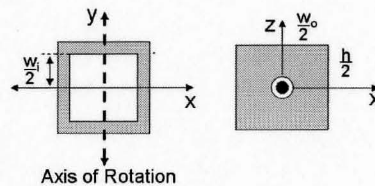


Figure C.2: Dimensions of support post showing axis and rotation.

where the first is an integration over the volume to the left of the $y$-axis while the second term is related to the volume on the right. Solving equation (C.2) and substituting $m_{mp} = 2\alpha^2 t\rho$, where $m_{mp}$ is the mass of the mirror plate, gives

$$I_{mp} = \frac{1}{6} m_{mp}\alpha^2 + \frac{1}{12} m_{mp} t^2. \tag{C.3}$$

### Support Post

The dimensions of the support post are illustrated in figure C.2 along with the axis of rotation. To moment of inertia of the support post can be determined by subtracting the imaginary moment of the hollow area from that of a solid rectangular

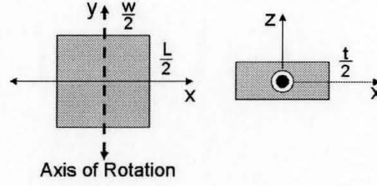


Figure C.3: Dimensions of yoke showing axis and rotation.

block with the same outer dimensions as the support post. Thus,

$$I_{sp} = \rho \int_{-\frac{w_o}{2}}^{\frac{w_o}{2}} \int_{-\frac{w_o}{2}}^{\frac{w_o}{2}} \int_{-\frac{h}{2}}^{\frac{h}{2}} (x^2 + z^2) dx dy dz - \rho \int_{-\frac{w_i}{2}}^{\frac{w_i}{2}} \int_{-\frac{w_i}{2}}^{\frac{w_i}{2}} \int_{-\frac{h}{2}}^{\frac{h}{2}} (x^2 + z^2) dx dy dz]. \quad (C.4)$$

Solving equation (C.4) gives

$$I_{sp} = \frac{\rho w_o^2 h}{12}(w_o^2 + h^2) - \frac{\rho w_i^2 h}{12}(w_i^2 + h^2). \quad (C.5)$$

### Yoke

The simplified dimensions for the yoke are depicted in figure C.3. The moment of inertia for this simple rectangular structure can be easily found to be

$$I_y = \frac{m_y}{12}(w^2 + t^2). \quad (C.6)$$

### Hinge

The moment of inertia of the hinges is similar to that of the yoke. Given the dimensions in figure C.4 the moment of inertia of the two hinges combined is

$$I_h = \frac{m_h}{6}(w^2 + t^2). \quad (C.7)$$

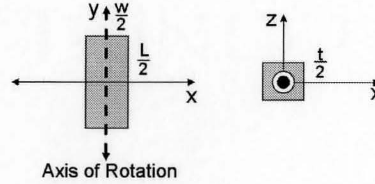


Figure C.4: Dimensions of torsional hinge showing axis and rotation.

## Total Moment of Inertia for the DMD™ Micromirror

In order to determine the moment of inertia of the complete DMD™ micromirror structure, each of the moments found in the previous sections must be added together. However, since the moments of both the mirror plate as well as the support post were calculated about axes parallel to, but translated away from, the axis of rotation of the complete structure, the parallel axis theorem is required. In this case a $md^2$ term is added to each of the translated terms, where $d$ is the distance which separates the parallel axes. The distances separating the axes of rotation of the mirror plate and the support post from the complete structures axis of rotation are given by

$$d_{sp} = \frac{t_y}{2} + \frac{h_{sp}}{2}, \text{ and} \tag{C.8}$$

$$d_{mp} = \frac{t_y}{2} + h_{sp} + \frac{t_{mp}}{2}, \tag{C.9}$$

where $t_y$ is the thickness of the yoke, $h_{sp}$ is the height of the support post, and $t_{mp}$ is the thickness of the mirror plate. Therefore, the moment of inertia of the complete DMD™ micromirror structure is given by

$$I = I_h + I_y + I_{sp} + m_{sp}d_{sp}^2 + I_{mp} + m_{mp}d_{mp}^2. \tag{C.10}$$

# Appendix D

# DMD Micromirror Modeling: MATLAB Simulation Code

```
0001 function MicromirrorSim(Mode)
0002 %=====================================================================
0003 %This function uses RK4 to simulate the dynamic motion of a DMD
0004 %micromirror for various applied voltage waveforms. The 'Mode'
0005 %input argument is used to specify a specific input waveform including:
0006 %Float, Crossover, Stay, and Modulate.
0007 %=====================================================================
0008
0009 tic
0010
0011 e0 = 8.85e-12; %[C^2/Nm^2] Permittivity of free space
0012
0013 wa = 1.5e-6;  %[m] Distance from hinge center to start of electrode
0014 wb = 4.39e-6; %[m] Distance from hinge center to end of electrode
0015 wc = 5.0e-6;  %[m] Distance from hinge center to end of spring tips
0016 L = 8.3e-6;   %[m] Length of electrode
0017
0018 g0 = 1.185e-6; %[m] Gap between electrodes at rest
```

```
0021
0022 k1 = (2*pi*68215)^2*I  %[N.m/rad] Torsional spring constant
0023 k2 = 73;              %[N/m.rad] Bending spring constant
0024 k3 = 0;               %[N.m/rad^3] Nonlinear element of hinge spring
0025 k4 = 0;               %[N/m.rad^3] Nonlinear element of spring tip
0026 b = sqrt(I*k1)/3.8    %[N.m.s/rad] Damping Coefficient
0027 b2 = 0;               %[N.m/rad] Air spring element
0028 mu = 0.25;            %Friction damping of spring tip contact
0029
0030 Ls = 1e-6;                          %[m] Spring tip length
0031 ContactAngle = asin(g0/(wc+Ls)); %[rad] Spring contact angle
0032 StopAngle = atan(g0/wb) - 1e-6;  %[rad] Mirror contact angle
0033
0034 if Mode == 0 -------------------%Crossover Transition
0035   load Va_Crossover.txt;
0036   load Vb_Crossover.txt;
0037   Va = Va_Crossover;
0038   Vb = Vb_Crossover;
0039   h = 1e-8;                       %[s]
0040   StartingAngle = -12*(pi/180); %[rad]
0041 elseif Mode == 1 ---------------%Stay Transition
0042   load Va_Stay.txt;
0043   load Vb_Stay.txt;
0044   Va = Va_Stay;
0045   Vb = Vb_Stay;
0046   h = 1e-8;                       %[s]
0047   StartingAngle = -12*(pi/180); %[rad]
0048 elseif Mode == 2 ---------------%Float Transition
0049   load Va_Float.txt;
0050   load Vb_Float.txt;
0051   Va = Va_Float;
0052   Vb = Vb_Float;
```

```
0053    h = 4e-8;                      %[s]
0054    StartingAngle = 12*(pi/180); %[rad]
0055 elseif Mode == 3 --------------%Modulation
0056    h = 1e-8;
0057    NumTimeSteps = 20000;
0058    Frequency = 0.08e6;
0059    Duty = 85;
0060
0061    NumCycles = NumTimeSteps*h * Frequency;
0062    CountsPerCycle = 1/Frequency/h;
0063    for j = 1:NumCycles
0064      for n = ((j-1)*CountsPerCycle + 1):(j*CountsPerCycle)
0065        if mod(n,CountsPerCycle) < CountsPerCycle*(100-Duty)/100
0066          n = int32(n);
0067          Va(n,1) = 12.5;
0068          Vb(n,1) = 7.5;
0069        else
0070          n = int32(n);
0071          Va(n,1) = 7.5;
0072          Vb(n,1) = 12.5;
0073        end
0074      end
0075    end
0076    StartingAngle = 3.305*(pi/180); %[rad]
0077 elseif Mode == 4 -----------------%Constant voltage
0078    h = 1e-8;
0079    NumTimeSteps = 20000;
0080
0081    Va(1:NumTimeSteps,1) = 15;
0082    Vb(1:NumTimeSteps,1) = 10;
0083
0084    StartingAngle = 1e-6*(pi/180);  %[rad]
```

```
0085 end
0086
0087 NumIter = size(Va); %Number of iterations
0088 t = zeros(1,1);     %Time
0089 theta = zeros(1,1); %Angular position
0090 v = zeros(1,1);     %Voltage
0091
0092 theta(1) = StartingAngle; %[rad]
0093
0094 for i = 2:NumIter   %Perform iterations
0095   t(i) = (i-1)*h;
0096   if abs(theta(i-1)) >= StopAngle;
0097     theta(i-1) = real((theta(i-1)/abs(theta(i-1)))*StopAngle);
0098     v(i-1) = 0;
0099   else
0100     if abs(theta(i-1)) < ContactAngle %Spring tip not in contact
0101       A1 = h*(v(i-1));
0102       B1 = h*(-(b/I)*v(i-1) - (b2/I)*theta(i-1) - (k1/I)*(theta(i-1))
0103         -(k3/I)*(theta(i-1))^3 - e0*L*Va(i-1)^2/(2*I*(theta(i-1)^2)) *
0104         (log((g0+wb*sin(theta(i-1))) / (g0+wa*sin(theta(i-1))) ) +
0105         (g0/(g0+wb*sin(theta(i-1)))) - (g0/(g0+wa*sin(theta(i-1))))) +
0106         e0*L*Vb(i-1)^2/(2*I*(theta(i-1))^2) * (log((g0-wb*sin(theta(i-
0107         1)))/(g0-wa*sin(theta(i-1)))) + (g0/(g0-wb*sin(theta(i-1)))) -
0108         (g0/(g0-wa*sin(theta(i-1))))));
0109
0110       A2 = h*(v(i-1) + 1/2*B1);
0111       B2 = h*(-(b/I)*(v(i-1) + 1/2*B1) - (b2/I)*(theta(i-1) + 1/2*A1)-
0112        (k1/I)*(theta(i-1) + 1/2*A1) - (k3/I)*(theta(i-1) + 1/2*A1)^3 -
0113        e0*L*Va(i-1)^2/(2*I*(theta(i-1) + 1/2*A1)^2) *
0114        (log((g0+wb*sin(theta(i-1) + 1/2*A1)) /
0115        (g0+wa*sin(theta(i-1) + 1/2*A1))) + (g0/(g0+wb*sin(theta(i-1) +
0116        1/2*A1))) - (g0/(g0+wa*sin(theta(i-1) + 1/2*A1)))) +
```

```
0117        e0*L*Vb(i-1)^2/(2*I*(theta(i-1) + 1/2*A1)^2) *
0118        (log((g0-wb*sin(theta(i-1) + 1/2*A1)) / (g0-wa*sin(theta(i-1)
0119        + 1/2*A1)) ) + (g0/(g0-wb*sin(theta(i-1) + 1/2*A1))) -
0120        (g0/(g0-wa*sin(theta(i-1) + 1/2*A1)))));
0121
0122      A3 = h*(v(i-1) + 1/2*B2);
0123      B3 = h*(-(b/I)*(v(i-1) + 1/2*B2) - (b2/I)*(theta(i-1) + 1/2*A2) -
0124        (k1/I)*(theta(i-1) + 1/2*A2) - (k3/I)*(theta(i-1) + 1/2*A2)^3 -
0125        e0*L*Va(i-1)^2/(2*I*(theta(i-1) + 1/2*A2)^2) *
0126        (log((g0+wb*sin(theta(i-1) + 1/2*A2)) / (g0+wa*sin(theta(i-1) +
0127        1/2*A2))) + (g0/(g0+wb*sin(theta(i-1) + 1/2*A2))) -
0128        (g0/(g0+wa*sin(theta(i-1) + 1/2*A2)))) +
0129        e0*L*Vb(i-1)^2/(2*I*(theta(i-1) + 1/2*A2)^2) *
0130        (log((g0-wb*sin(theta(i-1) + 1/2*A2)) / (g0-wa*sin(theta(i-1) +
0131        1/2*A2)) ) + (g0/(g0-wb*sin(theta(i-1) + 1/2*A2))) -
0132        (g0/(g0-wa*sin(theta(i-1) + 1/2*A2)))));
0133
0134      A4 = h*(v(i-1) + B3);
0135      B4 = h*(-(b/I)*(v(i-1) + B3) - (b2/I)*(theta(i-1) + A3) -
0136        (k1/I)*(theta(i-1) + A3) - (k3/I)*(theta(i-1) + A3)^3 -
0137        e0*L*Va(i-1)^2/(2*I*(theta(i-1) + A3)^2) *
0138        (log( (g0+wb*sin(theta(i-1) + A3)) / (g0+wa*sin(theta(i-1) +
0139        A3))) + (g0/(g0+wb*sin(theta(i-1) + A3))) - (g0/(g0+wa*
0140        sin(theta(i-1) + A3)))) + e0*L*Vb(i-1)^2/(2*I*(theta(i-1) +
0141        A3)^2) * (log((g0-wb*sin(theta(i-1) + A3)) / (g0-wa*
0142        sin(theta(i-1) + A3))) + (g0/(g0-wb*sin(theta(i-1) + A3))) -
0143        (g0/(g0-wa*sin(theta(i-1) + A3)))));
0144    else % ------------------------------Spring tip contacting substrate
0145      A1 = h*(v(i-1));
0146      B1 = h*(-(b/I)*v(i-1) - (b2/I)*abs(theta(i-1)) - (k1/I)*
0147        (theta(i-1))-(k2/I)*Ls^2*((theta(i-1)/abs(theta(i-1)))*
0148        ((abs(theta(i-1)) - ContactAngle))) - (k3/I)*(theta(i-1))^3 -
```

```
0149      (k4/I)*(Ls*((theta(i-1)/abs(theta(i-1)))*(sin(abs(theta(i-1)))-
0150      sin(ContactAngle))))^3 - e0*L*Va(i-1)^2/(2*I*(theta(i-1))^2) *
0151      ( log( (g0+wb*sin(theta(i-1)))/ (g0+wa*sin(theta(i-1))) ) +
0152      (g0/(g0+wb*sin(theta(i-1)))) - (g0/(g0+wa*sin(theta(i-1))))) +
0153      e0*L*Vb(i-1)^2/(2*I*(theta(i-1))^2)*( log( (g0-wb*
0154      sin(theta(i-1))) / (g0-wa*sin(theta(i-1))) ) + (g0/(g0-wb*
0155      sin(theta(i-1)))) - (g0/(g0-wa*sin(theta(i-1))))));
0156
0157
0158    A2 = h*(v(i-1) + 1/2*B1);
0159    B2 = h*(-(b/I)*(v(i-1) + 1/2*B1) - (b2/I)*abs((theta(i-1) +
0160      1/2*A1))-(k1/I)*(theta(i-1) + 1/2*A1) - (k2/I)*Ls^2*
0161      ((theta(i-1)/abs(theta(i-1)))*((abs(theta(i-1) + 1/2*A1) -
0162      ContactAngle)) -(k3/I)*(theta(i-1) + 1/2*A1)^3 - (k4/I)*(Ls*
0163      ((theta(i-1)/abs(theta(i-1)))*(sin(abs(theta(i-1) + 1/2*A1))-
0164      sin(ContactAngle))))^3 - e0*L*Va(i-1)^2/(2*I*(theta(i-1) +
0165      1/2*A1)^2) * ( log( (g0+wb*sin(theta(i-1) + 1/2*A1)) /
0166      (g0+wa*sin(theta(i-1) + 1/2*A1)) ) + (g0/(g0+wb*sin(theta(i-1)+
0167      1/2*A1))) - (g0/(g0+wa*sin(theta(i-1) + 1/2*A1)))) +
0168      e0*L*Vb(i-1)^2/(2*I*(theta(i-1) + 1/2*A1)^2) *
0169      (log((g0-wb*sin(theta(i-1) + 1/2*A1)) / (g0-wa*sin(theta(i-1)+
0170      1/2*A1)) ) + (g0/(g0-wb*sin(theta(i-1) + 1/2*A1)) -
0171      (g0/(g0-wa*sin(theta(i-1) + 1/2*A1)))));
0172
0173    A3 = h*(v(i-1) + 1/2*B2);
0174    B3 = h*(-(b/I)*(v(i-1) + 1/2*B2) - (b2/I)*abs((theta(i-1) +
0175      1/2*A2))-(k1/I)*(theta(i-1) + 1/2*A2) - (k2/I)*Ls^2*
0176      ((theta(i-1)/abs(theta(i-1)))*((abs(theta(i-1) + 1/2*A2) -
0177      ContactAngle))-(k3/I)*(theta(i-1) + 1/2*A2)^3 - (k4/I)*(Ls*
0178      ((theta(i-1)/abs(theta(i-1)))*(sin(abs(theta(i-1) + 1/2*A2))-
0179     sin(ContactAngle))))^3 - e0*L*Va(i-1)^2/(2*I*(theta(i-1) +
0180     1/2*A2)^2) * ( log( (g0+wb*sin(theta(i-1) + 1/2*A2)) /
```

```
0181        (g0+wa*sin(theta(i-1) + 1/2*A2)) ) + (g0/(g0+wb*sin(theta(i-1)+
0182        1/2*A2))) - (g0/(g0+wa*sin(theta(i-1) + 1/2*A2)))) +
0183        e0*L*Vb(i-1)^2/(2*I*(theta(i-1) + 1/2*A2)^2) * (log((g0-wb*
0184        sin(theta(i-1) + 1/2*A2)) / (g0-wa*sin(theta(i-1) + 1/2*A2)))+
0185        (g0/(g0-wb*sin(theta(i-1) + 1/2*A2)))-(g0/(g0-wa*sin(theta(i-1)+
0186        1/2*A2)))));
0187
0188
0189       A4 = h*(v(i-1) + B3);
0190       B4 = h*(-(b/I)*(v(i-1) + B3) - (b2/I)*abs((theta(i-1) + A3)) -
0191        (k1/I)*(theta(i-1) + A3) - (k2/I)*Ls^2*((theta(i-1)/
0192        abs(theta(i-1)))*((abs(theta(i-1) + A3) - ContactAngle))) -
0193        (k3/I)*(theta(i-1) + A3)^3 - (k4/I)*(Ls*((theta(i-1)/
0194        abs(theta(i-1)))*(sin(abs(theta(i-1) + A3))-
0195        sin(ContactAngle))))^3 - e0*L*Va(i-1)^2/(2*I*(theta(i-1) +
0196        A3)^2) * ( log( (g0+wb*sin(theta(i-1) + A3)) / (g0+wa*
0197        sin(theta(i-1) + A3)) ) + (g0/(g0+wb*sin(theta(i-1) + A3)))
0198        - (g0/(g0+wa*sin(theta(i-1) + A3)))) + e0*L*Vb(i-1)^2/
0199        (2*I*(theta(i-1) + A3)^2) * ( log( (g0-wb*sin(theta(i-1) +
0200        A3)) / (g0-wa*sin(theta(i-1) + A3)) ) + (g0/(g0-wb*
0201        sin(theta(i-1) + A3))) - (g0/(g0-wa*sin(theta(i-1) + A3))));
0202     end
0203   end
0204
0205   theta(i) = theta(i-1) + 1/6*(A1 + 2*A2 + 2*A3 + A4);
0206   v(i) = v(i-1) + 1/6*(B1 + 2*B2 + 2*B3 + B4);
0207 end
0208
0209 theta = theta.*180/pi; %[degrees]
0210
0211 %Plotting results (and experimental data)
0212 if Mode == 0
```

```
0213     t = (t.*1e6) - 20; %[us]
0214     Data(:,1) = t';
0215     Data(:,2) = theta';
0216     dlmwrite('CrossModel.txt', theta', '\t')
0217
0218     load CrossData.txt;
0219     ModelTime(1:2301) = t(1976:4276);
0220     figure;
0221     plot(t,theta,'k--',ModelTime,CrossData,'r')
0222     axis([-20 22  -14 14]);
0223 elseif Mode == 1
0224     t = (t.*1e6) - 20; %[us]
0225
0226     figure;
0227     plot(t,theta,'k--')
0228     axis([0 22  -14 14]);
0229 elseif Mode == 2
0230     t = (t.*1e6);
0231
0232     Data(:,1) = t';
0233     Data(:,2) = theta';
0234     dlmwrite('FloatModel.txt', theta', '\t')
0235
0236     load FloatDatab.txt;
0237     figure;
0238     plot(t,FloatDatab,'r',t,theta,'k--')
0239 else
0240     t = t.*1e6;
0241
0242     hold on;
0243     plot(t,theta,'k')
0244     axis([0 200 -14 14])
```

```
0245 end
0246
0247 toc
```

# Bibliography

[1] D. W. Monk. Digital Light Processing$^{\text{TM}}$: A New Image Technology for the Television of the Future. *International Broadcasting Convention.*

[2] M. R. Dokmeci, A. Pareek, S. Bakshi, M. Waelti, C. D. Fung, K. H. Heng, and C. H. Mastrangelo. Two-Axis Single-Crystal Silicon Micromirror Arrays. *J. Microelectromech. Syst.*, 13:1006–1021, 2004.

[3] D.A. Winick, B.E. Duewer, S. Palchaudhury, and P.D. Franzon. Performance Evaluation of Micromechanical Binary Phase-only Holographic Optical Elements. In *47th Electronic Components and Technology Conference.* Components, Hybrids, and Manufacturing Technology Society, IEEE.

[4] V. Milanovic, G. A. Matus, and D. T. McCormick. Gimbal-Less Monolithic Silicon Actuators for Tip-Tilt-Piston Micromirror Applications. *IEEE J. Select. Topics Quantum Electron.*, 10:462–471, 2004.

[5] M. K. Lee, W. D. Cowan, B. M. Welsh, V. M. Bright, and M. C. Roggemann. Aberration-correction results from a segmented microelectromechanical deformable mirror and a refractive lenslet array. *Opt. Lett.*, 23:645–647, 1998.

[6] L. J. Hornbeck. Deformable-mirror spatial light modulators. *Proc. Spatial Light Modulators and Applications III, SPIE*, 1150:86–102, 1990.

[7] J. Comtois, V. Bright, S. Gustafson, and M. Michalicek. Implementation of hexagonal micromirror arrays as phase-mostly spatial light modulators. *Proc.*

*SPIE Microelectronic Structures and Microelectromechanical Devices for Optical Processing and Multimedia Applications*, 2641:76–87, 1995.

[8] M. Fischer, H. Graef, and W. von Münch. Electrostatically deflectable polysilicon torsional mirrors. *Sensors and Actuators A*, 44:83–89, 1994.

[9] O. Degani, E. Socher, A. Lipson, T. Leitner, D. J. Setter, S. Kaldor, and Y. Nemirovsky. Pull-In Study of an Electrostatic Torsion Microactuator. *J. Microelectromech. Syst.*, 7:373–379, 1998.

[10] J. Young. Design, Modeling, and Experiment on Two-Degree-of-Freedom MEMS Micromirrors. Master's thesis, UC, Irvine, CA, 2001.

[11] A. Tuantranont and V. M. Bright. Segmented Silicon-Micromachined Microelectromechanical Deformable Mirrors for Adaptive Optics. *IEEE J. Select. Topics Quantum Electron.*, 8:33–45, 2002.

[12] D. Dudley, W. Duncan, and J. Slaughter. Emerging Digital Micromirror Device (DMD™) Applications. *SPIE Proc.*, 4985:14–25, 2003.

[13] M. A. Mignardi. From ICs to DMDs. *TI Technical Journal.*

[14] M. R. Douglas. Lifetime Estimates and Unique Failure Mechanisms of the Digital Micromirror Device (DMD™). *Proc. International Reliability Physics Symp., 36th Annual.*

[15] P. F. Van Kessel, L. J. Hornbeck, R. E. Meier, and M. R. Douglas. A MEMS-Based Projection Display. *IEEE Proc.*, 86:1687–1704, 1998.

[16] L. J. Hornbeck. Current Status of the Digital Micromirror Device (DMD) for Projection Television Applications (Invited Paper). *International Electron Devices Technical Digest.*

[17] L. Yoder, W. Duncan, E.M. Koontz, J. So, T. Bartlett, B. Lee, B. Sawyers, D.A. Powell, and P. Rancuret. DLP™ Technology: Applications in Optical Networking. *Proc. SPIE*, 4457:54–61, 2001.

[18] A. L. P. Dlugan, C. E. MacAulay, and P. M. Lane. Improvements to quantitative microscopy through the use of digital micromirror devices. *Proc. SPIE*, 3221:6–11, 2000.

[19] Q. S. Hanley, P. J. Verveer, M. J. Gemkow, D. Arndt-Jovin, and T. M. Jovin. An optical sectioning programmable array microscope implemented with a digital micromirror device. *J. Microscopy*, 196:317–331, 1999.

[20] E.P. Wagner II, B. W. Smith, S. Madden, J.D. Winefordner, and M. Mignardi. Construction and Evaluation of a Visible Spectrometer Using Digital Micromirror Spatial Light Modulation. *Appl. Spectroscopy*, 49:1715–1719, 1995.

[21] N. Doble, G. Yoon, L. Chen, P. Bierden, B. Singer, S. Oliver, and D. R. Williams. Use of a microelectromechanical mirror for adaptive optics in the human eye. *Opt. Lett.*, 27:1537–1539, 2002.

[22] R. Tyson. *Principles of Adaptive Optics.* Acedemic Press, San Diego, 2nd edition, 1998.

[23] C. Max. Astronomy 289C – Adaptive Optics – UCSC – Dept of Astronomy and Astrophysics. http://www.ucolick.org/7Emax/289C/Lecture1.2003.v1.bw.pdf, 2003.

[24] M. Born and E. Wolf. *Principles of Optics.* Pergamon Press, New York, 6th edition, 1993.

[25] J. Liang, D. Grimm, S. Goelz, and J. F. Bille. Objective measurement of wave aberrations of the human eye with the use of a hartmann-shack wavefront sensor. *J. Opt. Soc. Am. A*, 11:1949–1957, 1994.

[26] M. C. Roggemann, V. M. Bright, B. M. Welsh, S. R. Hick, P. C. Roberts, and W. D. Cowan. Use of micro-electro-mechanical deformable mirrors to control aberrations in optical systems: theoretical and experimental results. *Opt. Eng.*, 36:1326–1338, 1997.

[27] J. Liang, D. R. Williams, and D. T. Miller. Supernormal vision and high-resolution retinal imaging through adaptive optics. *J. Opt. Soc. Am. A*, 14:2884–2892, 1997.

[28] W. D. Cowan, M. K. Lee, B. M. Welsh, V. M. Bright, and M. C. Roggemann. Surface Micromachined Segmented Mirrors for Adaptive Optics. *IEEE J. Select. Topics Quantum Electron.*, 5:90–101, 1999.

[29] D. Gray. Astronomy 289C – Adaptive Optics – UCSC - Dept of Astronomy and Astrophysics. http://www.ucolick.org/7Emax/289C/Lecture14.2003.v1.bw.pdf, 2003.

[30] T. G. Bifano, R. K. Mali, J. K. Dorton, J. Perrault N. Vandelli, M. N. Horenstein, and D. A. Castanon. Continuous-membrane surface-micromachined silicon deformable mirror. *Opt. Eng.*, 36:1354–1360, 1997.

[31] N. Doble and D. R. Williams. The Application of MEMS Technology for Adaptive Optics in Vision Science. *IEEE J. Select. Topics Quantum Electron.*, 10:629–635, 2004.

[32] S. D. Senturia. *Microsystem Design.* Kluwer Acedemic Publishers, Boston, 2003.

[33] R. E. Meier and J. D. Huffman. U.S. Patent No. 6,522,454, 2003.

[34] M. G. Allen, M. Scheidl, R. L. Smith, and A. D. Nikolich. Movable Silicon Plates with Integrated Position Sensing. *Sensors and Actuators A*, 21–23:211–214, 1990.

[35] V. Annovazzi-Lodi, M. Benedetti, S. Merlo, and M. Norgia. Spot Optical Measurements on Micromachined Mirrors for Photonic Switching. *IEEE J. Select. Topics Quantum Electron.*, 10:536–544, 2004.

[36] K. A. Honer, N. I. Maluf, E. Martinez, and G. T. A. Kovacs. A high resolution laser based deflection measurement system for characterizing electrostatic actuators. *Transducer '95 Eurosensors IX*, 1:308–311, 1995.

[37] B. E. A. Saleh and M. C. Teich. *Fundamentals of Photonics.* John Wiley and Sons, New York, 1991.

[38] Y. Suzaki and A. Tachibana. Measurement of the $\mu$m sized radius of gaussian laser beam using the scanning knife-edge. *Appl. Opt.*, 14:2809–2810, 1975.

[39] F. L. Pedrotti and L. S. Pedrotti. *Introduction to Optics.* Prentice-Hall, New Jersey, 2nd edition, 1993.

[40] M. Ohring. *Materials Science of Thin Films.* Academic Press, San Diego, 2nd edition, 2002.

[41] P. M. Osterberg. *Electrostatically actuated microelectromechanical test structures for material property measurements.* PhD thesis, MIT, Cambridge, MA, 1995.

[42] R. B. Bhat A. K. Bhaskar, M. Packirisamy. Modeling switching response of torsional micromirrors for optical microsystems. *Mechanism and Machine Theory*, 39:1399–1410, 2004.

[43] S. P. Timoshenko and J. N. Goodier. *Theory of Elasticity.* McGraw-Hill, New York, 3rd edition, 1970.

[44] J.-M. Huang, A. Q. Liu, Z. L. Deng, Q. X. Zhang, J. Ahn, and A. Asundi. An approach to the coupling effect between torsion and bending for electrostatic torsional micromirrors. *Sensors and Actuators A*, 115:159–167, 2004.

[45] F. Pan, J. Kubby, E. Peeters, A. T. Tran, and S. Mukherjee. Squeeze film damping effect on the dynamic response of a mems torsion mirror. *J. Michromech. Microeng.*, 8:200–208, 1998.

[46] B. Bhushana and H. Liu. Characterization of nanomechanical and nanotribological properties of digital micromirror devices. *Nanotechnology*, 15:1785–1791, 2004.

[47] H. Liu and B. Bhushana. Investigation of nanotribological and nanomechanical properties of the digital micromirror device by atomic force microscopy. *J. Vac. Sci. Technol. A*, 2:1388–1396, 2004.

[48] J. D. Jackson. Visual Analysis of a Texas Instruments Digital Micromirror Device – The Institute of Optics at the University of Rochester. http://xray.optics.rochester.edu/workgroups/cml/opt307/spr05/john/, 2005.

[49] W. E. Bailey and J. C. Baker. U.S. Patent No. 5,526,951, 1996.

[50] J. D. Huffman, B. K. Dodge, and M. K. Fletcher. U.S. Patent No. 6,897,991, 2005.

[51] J. Chen, W. Weingartner, A. Azarov, and R. C. Giles. Tilt-Angle Stabilization of the Electrostatically Actuated Micromechanical Mirrors Beyond the Pull-In Point. *J. Microelectromechanical Systems*, 13:988–997, 2004.